Lithium conductivity characteristics of amorphous lithium silicate and lithium alumosilicate materials and their compaction

Von der Naturwissenschaftlichen Fakultät

der Gottfried Wilhelm Leibniz Universität Hannover

zur Erlangung des Grades

Doktor der Naturwissenschaften,

Dr. rer. nat.

genehmigte Dissertation

von

Dipl.-Chem. Sebastian Roß

geboren am 06. Juli 1985, in Stadthagen

2014

Kurzfassung

Lithiumhaltige amorphe Phasen sind vielversprechende Kandidaten für die Nutzung als Festelektrolyt in Lithium-Ionen-Batterien. Um die Eigenschaften dieser Phasen besser zu verstehen, wird der Einfluss verschiedener Faktoren auf die Lithiumleitfähigkeit in dieser Arbeit untersucht.

Dazu werden mit Hilfe von drei verschiedenen Herangehensweisen die Leitfähigkeitseigenschaften von amorphen Lithiumsilikaten und Lithiumalumosilikaten untersucht. In Kapitel 1 wird der Einfluss von Aluminium und nichtverbrückenden Sauerstoffatomen auf die strukturellen Eigenschaften und die Leitfähigkeitscharakteristika von Lithiumalumosilikatgläsern untersucht. Der Vergleich von vier vollständig polymerisierten und drei teilweise depolymerisierten Lithiumalumosilikatgläsern, synthetisiert über den Melt-Quench-Prozess, zeigt, dass AlO_4^- Tetraeder und nichtverbrückende Sauerstoffatome ähnliche Auswirkungen auf die Leitfähigkeit und Aktivierungsenergie von Li^+-Ionen im Material haben. Treten beide gleichzeitig auf, führt dies zu einem Absinken der Diffusivität des Lithiums und einer Erhöhung der Aktivierungsbarriere für die Lithiumbewegung im Vergleich zu Gläsern, die nur eines der Strukturmerkmale aufweisen. Die Aktivierungsenergien der polymerisierten Gläser liegt beispielsweise durchschnittlich 8 kJ/mol niedriger als in den teilweise depolymerisierten Gläsern, die Diffusivitäten unterscheiden sich um eine log-Einheit. Im Gegensatz dazu hat der Depolymerisierungsgrad keinen Einfluss auf den präexponentiellen Faktor der Arrheniusbeziehungen.

Neben der chemischen Zusammensetzung und der inneren, mikroskopischen Struktur, trägt auch die makroskopische Morphologie zur Leitfähigkeit bei. Kapitel 2 beschreibt die Entwicklung einer axialen Presszelle zur impedanzspektroskopischen *in situ* Untersuchung von Kompaktierungsprozessen. Anhand der Kompaktierung von pulverisiertem Lithiumtrisilikatglas bei 420 °C, 440 °C und 470 °C, in einem Druckbereich von Normaldruck bis zu 4 kbar, werden die Einsatzmöglichkeiten der Presszelle diskutiert und Schlüsse auf strukturelle Veränderungen während des Kompaktierungsprozesses gezogen.

Als alternativer Syntheseweg von amorphen Lithiumalumosilikatphasen wird in Kapitel 3 die chemische Gasphasensynthese genutzt um Precursor für Kompaktierungsexperimente in extern beheizten Gasdruckautoklaven herzustellen. Die Kompaktierung dieser Precursor führt zu ionenleitenden Festkörpern, die impedanzspektroskopisch auf ihre Lithiumleitfähigkeit untersucht werden. Hierbei zeigt sich, dass die Herstellung von festen Ionenleitern möglich ist, die ähnlich hohe Leitfähigkeiten erreichen wie die Lithiumalumosilikatgläser. Jedoch ist der genutzte CVS-Prozess sehr anfällig für Precursorverunreinigungen und die Bildung von Nebenprodukten, sodass der Prozess nur schwer zu reproduzieren ist.

Schlagwörter: Lithiumionenleitfähigkeit, Impedanzspektroskopie, amorphe Phasen

Abstract

Amorphous phases containing lithium are promising materials for lithium ion battery solid electrolytes. For a better understanding of the lithium conducting properties of those phases the influence of chemical composition, temperature and pressure are analyzed in this thesis.

For this, three different views are given on the lithium conducting characteristics of lithium silicate and lithium alumosilicate phases within three different stand-alone chapters. Chapter 1 deals with the analysis of four polymerized and three partly depolymerized lithium alumosilicate glasses, derived from the melt-quench process. With the help of impedance spectroscopy and Raman spectroscopy analyses the influence of aluminium content and degree of depolymerization on the lithium conducting characteristics are discussed and compared to aluminium-free lithium silicate phases from literature. It came out, that activation energy increase and diffusivity decrease with increasing content of aluminium and non-bridging oxygen atoms. The mean activation energy of fully polymerized lithium alumosilicate glasses is around 8 kJ/mol lower than in the partly depolymerized glasses, while the diffusion coefficient D_σ is differing around 1 log unit. The pre-exponential factor for the of Arrhenius relationships is not affected by the degree of depolymerization.

Beside the chemical composition and the inner, microscopic structure, the macroscopic morphology of the materials influence the conductivity behavior. In chapter 2 the development of a axial pressure cell is described, which allows the *in situ* impedance spectroscopic analysis of samples during compaction processes. The capabilities of the press cell are described by means of the compaction of powdery lithium tri-silicate at 420 °C, 440 °C and 470 °C in a pressure range from ambient up to 4 kbar. Conclusions on structural changes during the press process are drawn.

As an alternative synthesis route for amorphous lithium alumosilicate materials the chemical vapor synthesis (CVS) is used in chapter 3 to produce precursors for compaction experiments in externally heated cold seal pressure vessels (CSPV). The compaction of these CVS derived precursors enable the synthesis of solid ion conducting materials which are analyzed by impedance spectroscopy. It is shown that these solid ion conductors can have comparable high lithium conductivities like the bulk glasses described in chapter 1. But the CVS process used here is very prone to precursor contamination of the products and the formation of byproducts. That leads to limited reproducibility of the process.

Keywords: lithium ion conduction, impedance spectroscopy, amorphous phases

Content

List of abbreviations

A	Ampere
Å	Angstrom
a	long ellipsoidal dimension
A_0	pre-exponential factor
AC	alternating current
b	short ellipsoidal dimension
c. n.	coordination number
cf.	confer
CSPV	cold seal pressure vessel
CVD	chemical vapor deposition
CVS	chemical vapor synthesis
D	diffusion coefficient
DC	direct current
d_{sample}	sample thickness
DTA	differential thermal analysis
E_a	activation energy
EDX	energy dispersive X-Ray
EMPA	electron microprobe analysis
eV	electron volt
f_a	aspect ratio
fig.	figure
fwhm	full width at half maximum
I	current

I*	complex current
i. e.	id est - compare
ICP-OES	inductively coupled plasma - optical emission spectroscopy
IS	impedance spectroscopy
K	Kelvin
L	liter
LVDT	linear variable differential transformer
m	meter
min	minute
mol%	molar percent
N	charge carrier concentration
NBO	non bridging oxygen
NMR	nuclear magnetic resonance
p	pressure
PTFE	polytetrafluoroethylene
PVC	polyvinyl chloride
q	ion charge
R	Boltzmann constant
SEM	scanning electron microscopy
spec.	specific
T	tetrahedron
tab.	table
T_g	glass transition temperature
TG	thermogravimetry
U	voltage
U*	complex voltage

V	Volt
XRD	X-Ray diffraction
Z^*	complex impedance
$Z_{imaginary}$	imaginary part of complex impedance
Z_{real}	real part of complex impedance
ρ_I	phase angle of current
ρ_U	phase angle of voltage
σ_{DC}	direct current conductivity
ω	frequency
wt%	weight percent

List of figures

List of tables

Preface

Solid ion conductors are of high technical and scientific interest. Lithium is used today in a vast variety of lithium ion primary or secondary batteries and energy storage technologies become more and more important in times of changing energy concepts. The change from fossil fuels to more sustainable energy sources needs a reliable way of electrical energy storage. The replacement of currently used liquid and flammable lithium battery electrolytes with non-flammable non-toxic solid lithium electrolytes would be a step to a more secure and easy use of those energy storage technologies. For this, the better understanding of ionic conductivity mechanisms, i. e. the influence of composition, structure, temperature and pressure on ionic conducting characteristics of materials is very important.

The phenomenon of fast ionic diffusion in solid materials is of scientific and technical interest since decades. A big variety of material classes like oxides, halogenides, chalcogenides and its combinations were analyzed in terms of ionic conductivity and the responsible transport mechanisms [1], [2], [3], [4]. It turned out that all these materials share some general mechanistic aspects of ionic conductivity [5], [6] and common responses in impedance spectroscopic analysis [7].

Those common aspects are the power law behavior and Arrhenius like temperature dependence. The power law behavior corresponds to the dependence of ac conductivity from logarithmic ac frequency which shows a general trend for solid ion conductors, described by Jonscher as `universal` dielectric response or power law [8]. Both aspects are valid not only for a large amount of compositions but also for different structural classes of solid electrolytes, like single crystals, amorphous glasses or organic polymers [9], [10], [11].

Preface

The basic property of crystalline ionic conductors is the occurrence of structural defects. These defects like Frenkel or Schottky defects, dislocations or grain boundaries lead to a deviation from the ideal structure allowing ionic mobility [12]. These phenomena are valid for polycrystalline materials and single crystals. Amorphous solids show a more open structure without a pronounced long range order. Nevertheless, the modeling background and deduced mathematical relations can also be used to describe ion hopping and jump relaxation processes in amorphous solids [13], although physical interpretation of processes is less clear due to the larger variety of bond lengths, bond angles and build order of structural elements. This more flexible amorphous structure leads to comparable high conductivity values in comparison to single crystals with the same compositions [14]. Additionally lithium ion conductors benefit from the small ionic radius of lithium ions (0.76 Å for c. n. 6) [15] which allows a high mobility in the solid structure.

Amorphous solids can be prepared on several ways. The most common is the melt-quench technique where a mixture of molten oxides (applied directly or derived *in situ* from carbonates) is cooled down fast below the melting point. The melt components cannot relax to the ideal crystal structure and freeze in the amorphous state. Other methods are the chemical vapor deposition (CVD) of thin films [16], the chemical vapor synthesis (CVS) of particles or the sol-gel route to precipitate amorphous solids from solution [17]. Especially CVD, CVS or sol-gel products are not homogenous bulk materials but films or powders made of distinct particles. For those materials not only the chemical composition and crystallographic state determine the ionic diffusion characteristics. Structural properties like particle size distribution and morphology have also a large influence on ionic conductivity. The formation of ceramic materials by compaction and/or sintering of powdery starting materials leads to new ion conducting materials. The manipulation of these composite ionic conductors can highly influence the ionic diffusivity by introducing grain boundaries or particle/particle interfaces [12], [18].

Preface

Compaction and sintering methods to manipulate the structure of solid materials are known for a long time and became an important part of industrial production procedures with time. Different compaction techniques are used for different approaches. Diamond anvil presses are used for the application of very high pressures up to 300 GPa (or 3 Megabars) [19] mostly for scientific reasons. Piston cylinder presses are used for application of medium to high pressures but they allow a much larger sample volume in comparison to diamond press cells. Because of this, Piston cylinder presses are used, but not only, for scientific and industrial applications in powder metallurgy and ceramic synthesize. In general, compaction processes are used from very small scales for scientific reasons [20], [21] up to large industrial scales.

This thesis was prepared within the framework of the Research Group FOR 1277 `molife` supported by the German Science Foundation. It is about Li^+ conductivity in lithium silicates and lithium alumosilicates to contribute to the question which mechanisms of lithium mobility are valid in solid and amorphous lithium ion conductors.

Lithium conductivity characteristics are known for many solid amorphous ion conductors and also for lithium alumosilicates, but structural influences introduced by compositional changes are not fully understood; especially the influence of aluminium, non-bridging oxygen atoms and the macroscopic structure of amorphous lithium silicates and lithium alumosilicates. Remaining questions are how the composition of lithium alumosilicate glasses and the degree of depolymerization influences the lithium conductivity behavior and which structural information can be obtained from this. Additionally, how the macroscopic structure, the synthesize route and compaction processes does influence these properties.

To answer these questions the lithium conductivity characteristics of seven lithium alumosilicate glass compositions are determined by impedance spectroscopy to reveal the influence of chemical composition and non-bridging oxygen atoms within the amorphous

structure. Furthermore, the development of a new axial pressure cell for *in situ* impedance spectroscopy analysis is described on the basis of compaction experiments on lithium tri-silicate glass powder. Additionally, the CVS process is used to synthesize amorphous lithium alumosilicate powders which are compacted in cold seal pressure vessels to obtain solid lithium ion conductors. So this work gives three different views on the phenomenon of lithium ion conductivity in glassy lithium silicate and alumosilicate materials. It is separated into three stand-alone chapters, each dealing with one aspect:

Chapter 1 gives insights in the lithium conduction mechanism in bulk lithium alumosilicate glasses of different composition. A set of four polymerized and three partly depolymerized lithium alumosilicate glasses of different composition are studied by impedance spectroscopy (IS) and Raman spectroscopy to analyze the structural influence of aluminium and non-bridging oxygen atoms on the lithium diffusivity. The results are compared to aluminium-free, amorphous lithium silicate systems. The content of chapter 1 is partly published in *Phys. Chem. Chem. Phys.* **2015, 17 (1), 465 - 474** [Sebastian Ross, Anna-Maria Welsch, Harald Behrens, *Lithium conductivity in glasses of the Li_2O - Al_2O_3 - SiO_2 system*, Phys. Chem. Chem. Phys., **2015**, 17 (1), 465 - 474] (compare List of publications).

On the basis of amorphous lithium tri-silicate powder the development of a new axial pressure cell apparatus is presented in chapter 2. The pressure cell allows *in situ* impedance spectroscopy analysis during the compaction process of powdery materials in a pressure range from ambient up to 4.3 kbar to obtain information about the pressurization process itself. After description of the development process a proof of concept is given on the example of lithium tri-silicate glass powder, which is obtained also by melt quench technique and crushed afterwards.

Contrary to this, the direct synthesis of powdery amorphous lithium ion conductors and their compaction to bulk products is shown in chapter 3. The chemical vapor synthesis

route is used to obtain small particles of amorphous lithium alumosilicates. These small particles are compacted in externally heated cold seal pressure vessels (CSPV) with the help of high pressure argon gas to get macroscopic solid lithium ion conducting materials. These materials are analyzed for their lithium conducting characteristics with the help of impedance spectroscopy also used for the experiments in chapter 1.

Common aspects of all three chapters are the influence of composition and structure on the diffusivity characteristics of glassy lithium silicates and lithium alumosilicates and its analysis with impedance spectroscopy methods.

Chapter 1: Lithium conductivity in lithium alumosilicate glasses

1.1. Introduction

Lithium-alumosilicate glasses and glass-ceramics are of considerable importance in a variety of industrial applications. Li-Al-Si containing minerals like spodumene ($LiAlSi_2O_6$) and petalite ($LiAlSi_4O_{10}$) are well-known for their negative thermal expansion coefficient and as such are broadly used in high precision thermo- and electro-optics. Li-containing alumosilicate glasses and nanocrystalline materials are fast ion conductors [22], [13] and thus possible materials for solid lithium ion batteries. However, the mechanisms governing the transport of lithium ions in silicate-based networks are still insufficiently understood.

There are indications that Al plays an important role for Li-dynamics in lithium alumosilicate glasses and that the mechanisms of lithium transport are different from aluminum-free lithium silicate glasses [24], [25]. The exact nature of the interaction of AlO_4^- tetrahedra with the mobile Li-cations in comparison to non-bridging oxygen atoms (NBO) in the alumosilicate matrix is yet to be determined.

This work focuses on the relationship between the local interactions of $[AlO_4]^-$-tetrahedra and NBOs with lithium ions, which are the only mobile species in the studied materials. For this purpose two series of glasses were analyzed. Four fully polymerized glasses with a constant Li/Al ratio of one and a variable Al/Si ratio are compared with a series of three partly depolymerized glasses (Li/Al > 1) with nearly constant lithium content. In these glasses three types of lithium coordinating oxygen atoms occur: (i) Si-O-Si with a formal charge of 0, (ii) Si-O-Al with a formal charge of (-¼) and (iii) non-bridging oxygen atoms, Si-O$^-$ with a formal charge of -1. These oxygen atoms determine the coordination of lithium in the material both on regularly occupied sites and on interstitial sites which are

passed by lithium during transition between different regular, low potential sites. Impedance spectroscopy is used to investigate the electric conductivity of the glasses, and Raman spectroscopy provides insights in the network topology. The particular role of aluminum in the network structure will be elaborated by comparison to data for lithium silicate glasses [26], [24].

1.2. Li_2O - Al_2O_3 - SiO_2 glasses

In a lithium alumosilicate (LAS) glass, the glass structure comprises the network-forming SiO_4 and AlO_4^- tetrahedra units connected via bridging oxygen atoms, while Li^+ represents the network modifying cation and the only mobile species present. The glasses with a Li to Al ratio of 1:1 are fully polymerized, meaning the network contains only bridging oxygen atoms. The incorporation of network-modifiers, such as Li_2O, in excess to the quantity needed for charge compensation of Al^{3+} cations leads to the formation of non-bridging oxygen atoms and a reduction in the degree of glass network polymerization. As a consequence, melting temperatures and melt viscosity are lowered [27]. The degree of polymerization in a silicate glass can be characterized by the ratio of non-bridging oxygen per tetrahedral unit, NBO/T [28]:

$$NBO/T = \sum_{i=1}^{i}\left(nM_i^{n+}\right)/T \qquad (1)$$

where M_i represents network modifying cations with charge n. The sum is obtained after all metal cations are subtracted which are needed for charge compensation. T represents the sum of all tetrahedral coordinated cations.

Chapter 1: Lithium conductivity in lithium alumosilicate glasses

To investigate the transport properties of lithium in different Al-Si-O glass networks, we have analyzed a group of fully polymerized (group 1) and a group of depolymerized glasses (group 2). The fully polymerized glass samples were provided by Alan Whittington, University of Missouri [29]. Depolymerized glasses were synthesized in the Institute of Mineralogy, Leibniz University of Hanover. The compositions are represented in figure 1 and are listed in table 1. For three of the polymerized glasses compositional analogues exist in nature as minerals: eucryptite, $LiAlSiO_4$ (EUC); spodumene, $LiAlSi_2O_6$ (SPO); petalite, $LiAlSi_4O_{10}$ (PET). The join is completed with a composition $LiAlSi_3O_8$ (FSP) which can be considered as the lithium analogue of albite. The labels in parentheses are used further on in reference to the compositions.
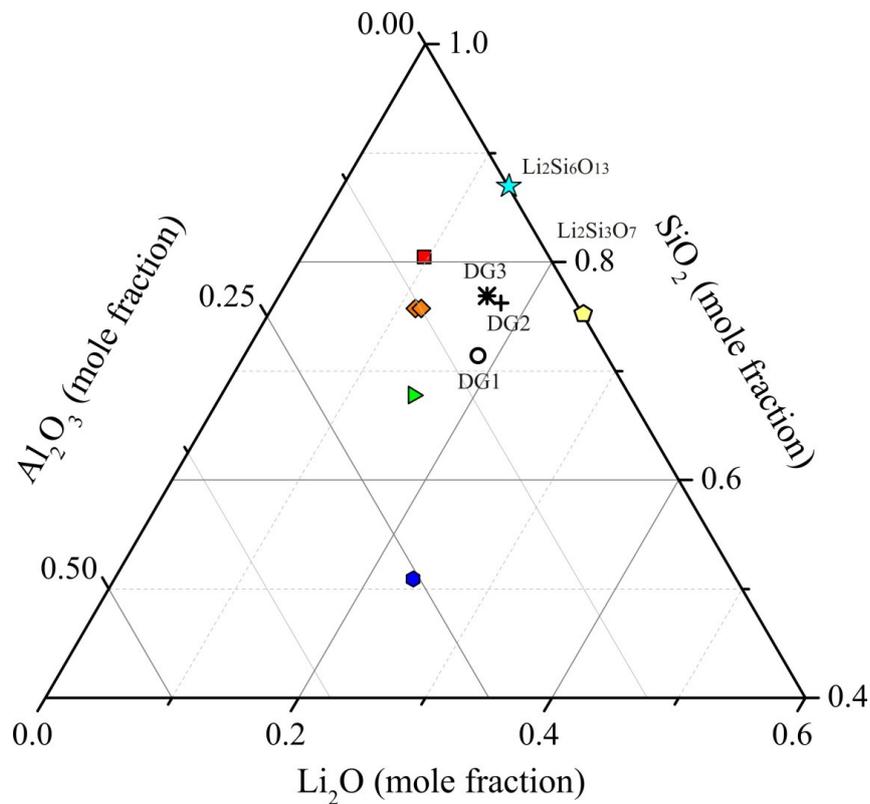
Figure 1: Ternary diagram of glass composition given in mole percent.

Theoretically, glasses of group 1 contain only bridging oxygen which are bond to two silicon atoms [≡Si-O-Si≡] or between a silicon and aluminum tetrahedra [≡Si-O-Al$^{(-)}$≡]. According to the Löwenstein rule [30] neighboring alumina tetrahedra [≡$^{(-)}$Al-O-Al$^{(-)}$≡] are unlikely in alumosilicates, but NMR spectroscopy gives evidence that such connections may occur in small quantities [31]. Glasses of group 2 contain non-bridging oxygen atoms [≡Si-O$^-$]) in addition to both types of bridging oxygens.

Regular and interstitial sites of lithium in the glass structures are formed by combinations of these types of oxygen. ^{6}Li MAS NMR spectroscopy indicates that silicate glasses have wide distribution of Li coordination numbers between four and six [32]. Hence, large differences in lithium mobility can be expected depending on the relative abundance of oxygen species.

Table 1: Composition of the glasses derived by ICP-OES for lithium and EMPA and ICP-OES measurements for silicon and aluminium in combination. Remarks: a) Contents of Al_2O_3 and SiO_2 were determined by ca. 5 EMPAs and Li_2O content by 2-3 OES analyses. Na_2O, K_2O and CaO content were below detection limit of the EMPA, i.e. present in less than 0.01 wt%. b) Sample $LiAlSi_2O_6$-1 and $LiAlSi_3O_8$-1 from Hofmeister et al. (2009) [29] are identical to samples used in this thesis. c) EMPA data for petalite are from Welsch et al. (2012) [33], but Li_2O content was newly determined by OES in this work. d) NBO/T is calculated by Eqn. (1), negative values have no physical meaning but indicate deficiency of Li with respect to Al, consistent with atomic Li/Al ratios.

Composition	Li_2O		Al_2O_3^{a}		SiO_2^{a}		NBO/T^d	Li/Al
	wt%	1σ	wt%	1σ	wt%	1σ		at. ratio
$LiAlSiO_4$	11.05		40.66	0.36	47.47	0.25	-0.04	0.93
$LiAlSi_2O_6$	7.07							
$LiAlSi_2O_6$-1^b	7.15		27.41		63.79			
$LiAlSi_3O_8$	5.62		20.68	0.09	73.27	0.04	-0.04	0.89
$LiAlSi_3O_8$-1^b	5.60		21.24		72.90		-0.02	0.93
$LiAlSi_4O_{10}$^{c}	4.80		16.37		79.09		-0.03	0.90
DG1	9.40	0.14	17.33	0.25	73.36	0.41	0.19	1.85
DG2	8.83	0.64	11.13	0.08	80.94	0.47	0.24	2.71
DG3	9.49	0.23	9.73	0.27	81.66	0.73	0.29	3.33

1.3. Analytical methods

In the following, a short theoretical background of impedance spectroscopy and Raman spectroscopy is given. Impedance spectroscopy is the basic analytical method for conductivity measurements in all three chapters. Raman spectroscopy is mainly focused on chapter one and the characterization of bulk glass samples and their structure.

1.3.1 Impedance spectroscopy

The analysis of the frequency-dependent interaction of matter with electromagnetic fields applied by an alternating current (AC) or a direct current (DC) is called impedance spectroscopy. The interaction of matter in condensed phases with electromagnetic fields allows to draw conclusions on mobile charge carriers in the material and their conductive and diffusivity behavior. The theoretical background has already been described by Macdonald (1987), Wedler (1987) and Orazem (2008) [34], [35], [36] and a short summary is given at the example of mobile charge carriers in a solid matrix (like Li^+ ions in a glass matrix).

The mobile charge carriers are forced to move with the induced electromagnetic field gradient when an AC voltage is applied to a solid material. The ion follows the gradient and either vibrates at its original place or jumps to another free place in the material. The jump of a charge carrier changes the chemical potential at both, the new and old position. Two possible scenarios might happen: (i) the ion jumps back to its original place and the jump is called unsuccessful, or (ii) the surrounding matrix relaxes and stabilizes the ion in its new position and the jump is called successful. The moving charge carriers induce a measureable current. After Ohms law the resistance of a material is given by the ratio of

applied voltage and the induced current. The complex resistance, as the ratio of complex voltage and complex current, is called impedance of the material Z^*

$$Z^* = \frac{U^*}{I^*} \tag{2}$$

with U^* as complex voltage and I^* as complex current. Both, complex current and complex voltage, are frequency dependent and may show a phase shift between voltage and current, which can be described with

$$I^* = I \cdot e^{i(\omega t + \rho_I)} = I \cdot e^{i(\omega t)} \cdot e^{i(\rho_I)} \tag{3}$$

and

$$U^* = U \cdot e^{i(\omega t + \rho_U)} = U \cdot e^{i(\omega t)} \cdot e^{i(\rho_U)} \tag{4}$$

with circular frequency ω, voltage phase ρ_U and current phase ρ_I. The circular frequency ω equals $2\pi f$ (with f as frequency of the applied AC voltage). This results in the frequency dependent complex impedance answer of the sample with an applied AC voltage and by this induced complex current

$$Z^* = \left(\frac{U}{I}\right) \cdot e^{i(\rho_u - \rho_i)} \tag{5}$$

with the phase shift (ρ_U - ρ_I) which equals ρ. From the vector presentation of imaginary values the real and imaginary part can be separated to $Z_{real} = |Z| \cdot \cos(\rho)$ and $Z_{imaginary} |Z| \cdot \sin(\rho)$. Further calculations and experimental specific data treatment is described with the obtained results.

1.3.2 Raman spectroscopy

Raman spectroscopy is a method to analyze the inelastic scattering of light during interaction with materials. From this interaction structural and compositional characteristics of the analyzed material can be concluded [37].

The interaction of light and matter leads to the excitation of electrons from their ground state to excited states by interactions of photons with phonons and molecular vibrations. The relaxation from the higher energy states results in emission of light. The emitted light can be of the same energy or discretely altered on quantum levels. If emitted photons and incident light have the same energy, no change in the wave vector or frequency occurs. This process is called Rayleigh-scattering and acts as the zero point in the spectrum. But incident light can react with matter causing a change in wave vector and frequency of the outgoing signal, producing an inelastic scattering of light. This change can release either photons of higher or lower energy than the incident light. When the energy state after interaction falls below the initial (ground) state, the matter emits energy, which is combined with the incident light and the signal is observed at frequencies higher than the incident light. Thus signal of higher energy is called anti-Stokes shifted. The more statistically probable interaction is whereby electrons fall back to states above their ground state, producing a signal lower in energy, i.e. the Stokes shift. The vibrational states on both sides of the Rayleigh scattering require the same differential amount of energy on the quantum level but the probability of a stoke shifted interaction is higher. Due to this, the signal of the Stokes shift is more intense than the anti-Stokes shift and as such is used for the material analysis. It is known as the Raman shift or the Raman spectrum. The peaks in the Raman spectrum arise from the changed bonding polarizability caused by molecular vibrations during excitation by incident light. Molecular vibrations can be of bending and stretching type, symmetric or asymmetric in their nature and depending on the site

symmetry. The produced signal will be Raman active, silent or forbidden [38]. Crystalline samples show sharp peaks in the Raman spectra due to the highly accurate long range order and narrow range distribution of vibrational energies. In amorphous materials bond lengths and angles distributions are much broader. Due to this the Raman peaks of the analyzed amorphous lithium alumosilicates are broad peaks with large overlapping areas. By deconvolution of the spectra and fitting of individual peaks the information about chemical phase, abundance of structural units, changes in the structure as a function of temperature, pressure or chemistry can be obtained.

To obtain spectra which can be compared, the raw data has to be corrected for the influence of temperature, baseline background and scale. At first the minimum intensity value of the raw spectrum is calculated to be 0 (the whole spectrum is shifted in intensity, so that the lowest point of the spectrum is zero). Afterwards, the Bose-Einstein statistics of the phonon population is used for temperature correction [39], [40], [41]. This is based on the Bose-Einstein anomaly that at temperatures above 0 K not only the energetic ground states of the atoms are populated but higher energy levels, too. The measured intensity is influenced by this depending on the wavelength of the emitted light and the temperature of the experiment. To correct this, the population distribution of the energy levels is calculated and the spectra are corrected by the phonon occupation as a function of frequency.

Afterwards the spectra are baseline corrected what is especially important at low and high energy parts of the spectra. At low energies the Rayleigh and boson peak influences the baseline and pretend higher intensities.

1.4. Experimental procedures

1.4.1 Glass synthesis and analytics

The depolymerized glasses were prepared by melting powder mixtures of high purity Li_2CO_3, Al_2O_3 and SiO_2 in a platinum crucible at temperatures of 1873 K and subsequent quenching by placing the crucible in water. To improve the quality of the synthesized glass, the melting procedure was repeated twice, with fine milling of the glass product in between. The glasses synthesized in this way were often strained, making them prone to breaking and difficult to handle. In order to improve the mechanical stability, the glasses were slowly heated to 450 °C, and after 15 to 20 minutes of dwelling time slowly cooled to ambient temperature at a rate of 5 K/min.

The composition of the synthesized glass samples was analyzed by inductively coupled plasma optical emission spectroscopy (ICP-OES) and electron-microprobe analysis (EMPA). For ICP-OES measurements a defined mass (50 mg to 150 mg) of glass were dissolved in a mixture of 1 mL hydrofluoric acid (40 %), 2 mL phosphorous acid (85 %) and 4 mL nitric acid (70 %) in a PTFE vessel heated by a microwave MLS START 1500. These measurements were done with a Varian ICP-OES 715 at $\lambda_{Al} = 308.215$ nm, $\lambda_{Li} = 670.783$ nm and $\lambda_{Si} = 250.690$ nm. The content of silicon, aluminum and lithium in the glass sample were recalculated from concentration data of the measured solution and the initial weight.

To control the composition determined by ICP-OES and to check the homogeneity of the glasses, EMPA measurements were carried out. Lithium as a light element is not measurable by EMPA, but Li_2O contents may be estimated as difference to 100 wt%, if all other oxides are quantified. The analyses were performed on a CAMECA SX-100 microprobe. Typically, three to five points were analyzed on each sample. A beam current

of 15 nA was used with an acceleration voltage of 15 kV and a beam size of 5 μm, while the counting times were 10 to 20 s depending on the sample. The programmed matrix correction "PAP" by Pouchou and Pichoir [42] was used to correct the measured values of Al and Si. Compositions reported in table 1 are based on ICP-OES data for Li_2O and EMPA data for Al_2O_3 and SiO_2.

The density of each glass was determined using the buoyancy method, i.e. by measuring the weight in ethanol and in air (table 2). The accuracy of the measurements was in the order of *per mill* for standards of quartz crystal (ρ = 2.684 g/cm^3) and silica glass (ρ = 2.203 g/cm^3).

1.4.2 Determination of the T_g

The glass transition temperature (T_g) of the samples was determined to ensure that high temperature impedance spectroscopy measurements are not affected by structural relaxation of the network and to get information about the thermal stability of the glasses. T_g was derived by differential thermal analysis using the TG/DTA Setsys Evolution 1750 setup. The material was heated up in an alumina crucible (heating rate: 5 K/min), kept for 10 min at the target temperature and cooled down afterwards (cooling rate: 20 K/min). A flow of 20 mL/min of synthetic air (80 % N_2, 20 % O_2) was used to purge possibly occurring gaseous products. An empty alumina crucible was taken as reference, which was periodically measured under the same conditions in order to accurately correct the sample data. T_g values were derived from the DTA curves recorded during heating to avoid falsification by possible crystallization or phase separation at high temperatures. To define T_g , the tangent intersection method was applied at the DTA curves (intersection of two tangents at the curve before minimum, cf. Fig. 2). The experimental technique was verified

to be correct within +/- 1.5 K by measurements on the DGG1 standard glass of the German Glass technical Society [43].
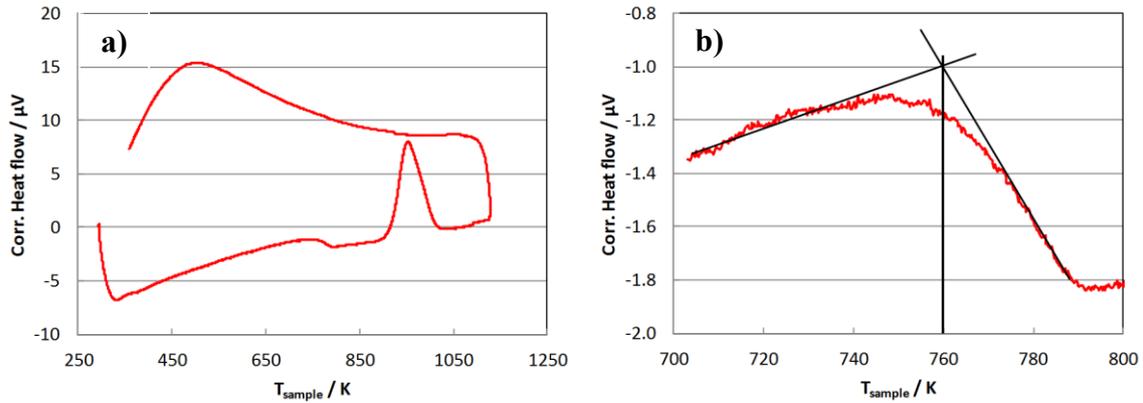
Figure 2: Example of T_g determination of sample DG3. a) DTA curve for increasing and decreasing temperature. b) Detailed view on DTA curve from 700 to 800 K for increasing temperature and inserted tangents for T_g determination.

T_g values for the alumosilicate glasses are listed in table 2. Derived values for glasses of group 1 agree with literature data within ± 5 K for EUC [44], [29], SPO, FSP and PET [29].

1.4.3 Impedance spectroscopy

For the conductivity experiments, circular Ag electrodes with 1 mm in diameter were applied. To produce the electrodes, Ag lacquer (Co. Dr. Ropertz-GmbH) was deposited and sintered on the sample surfaces at 573 K for 30 minutes. After slowly cooling to room temperature the samples with properly attached sintered electrodes were placed into the impedance sample holder between two Pt-cones. A spring-tension mechanism was applied to one Pt-cone via a ceramic rod to ensure good electrical contact. Afterwards the sample holder was inserted into an earth-grounded gold tube, serving as an insulating shield. Impedance measurements were performed in a tube furnace Nabertherm R50/500/13.

During the experiment the temperature was continuously recorded at a distance of 2 and 5 mm from the sample using two electrically shielded type-K thermocouples. Heating rate was varied between 0.8 and 0.9 K/min. Cooling rates, after switching off the furnace, decrease from 2.4 K/min in the high temperature region to 0.7 K/min around 400 K.

The electrical conductivity was measured periodically during heating and cooling using a Novocontrol Alpha AN impedance analyzer equipped with a Novocontrol ZG4 module to allow a four terminal configuration. Before the measurements, the spectrometer was calibrated, using a short circuit arrangement and a certified 100 Ω resistance. Additionally, internal high capacity references were used to calibrate the system. Impedance spectra were collected from 0.5 Hz to 2 MHz at each selected temperature. The duration of each conductivity measurement depends on the absolute conductivity because a certain confidence is needed by repeating the measurement. The heating/cooling program was not interrupted for recording impedance data, and the spectra correspond to a temperature interval of ~8 K at low temperature and 1 - 3 K at the highest temperature. However, the temperature corresponding to the center of the conductivity plateau was always determined with a precision better than ± 1 K. The accuracy of conductivity measurements was verified to be better than ± 0.10 log units by comparison of conductivity data of $LiAlSi_2O_6$ glasses with literature data [33].

1.4.4 Raman spectroscopy

The local structural characteristics of each glass were analyzed by Raman spectroscopy before and after experimental runs. The measurements were made on a confocal Bruker Senterra micro-Raman spectrometer equipped with an Olympus BX 51 microscope and an Andor DU420-OE CCD camera. Unpolarized spectra were collected at ambient conditions, using the 532 nm laser excitation line with 20 mW power, under the 50x magnification of an Olympus objective for 10 s with 2 times acquisition repetitions. Instrumental precision was within $\pm$ 3 cm^{-1}. The spectra were baseline and temperature corrected [40], [41]. The reproducibility of Raman structural signal was confirmed by repeated measurements as well as measurements at different areas of each sample.

1.5. Results

1.5.1 Chemical analyses of LAS glasses

All synthesized glasses are clear, colorless and free of bubbles, inclusions or cracks. The chemical composition of the samples, analyzed by ICP-OES and EMPA is shown in table 1. All samples contain lithium, aluminium, silicon and oxygen while other alkalis are below the detection limit of the EMPA. This is important because other alkalies may act as additional charge carriers and mask the effect of lithium mobility. Furthermore, a second alkali may produce a mixed alkali effect leading to a decrease in conductivity [45], [46], [47]. The NBO/T value of the depolymerized glass samples ranges from 0.19 to 0.29. The fraction of NBO compared to total oxygen is in the order of 10 - 15 % in the studied compositions of group 2. The depolymerized glasses show a significantly lower glass transition temperature T_g (760-773 K) than the polymerized glasses (922 - 1015 K, cf. table 2).

Table 2: Material and lithium conductivity characteristics of analyzed glass compositions

Composition	T_g	ρ	Z	Z	T-range	$\log_{10}A_0$	E_a	$\log_{10}D_\sigma$ at 500 K
	K	g/cm^3		without Li	K	A_0 in SKm^{-1}	kJ/mol	D_σ in m^{2}s^{-1}
LiAlSiO$_4$	922	2.437(1)	56.4	59.89	298-717	7.4(9)	67.5(09)	-12.89(01)
LiAlSi$_2$O$_6$	960	2.381(2)	57.63	60.34	333-800	7.2(7)	68.9(04)	-12.98(01)
LiAlSi$_3$O$_8$	1010	2.322(2)	59.4	61.09	304-532	7.4(8)	70.5(05)	-12.90(01)
LiAlSi$_4$O$_{10}$	1015	2.309(1)	59.66	61.16	350-500	7.0(2)	72.5(11)	-13.16(01)
DG1	769	2.362(3)	58.67	59.43	327-625	7.4(1)	76.5(13)	-13.89(01)
DG2	773	2.357(6)	58.57	59.69	327-626	7.4(8)	77.2(11)	-13.86(01)
DG3	760	2.323(8)	59.64	60.79	425-714	7.7(7)	78.0(08)	-13.82(01)

1.5.2 Specific conductivity

The results of impedance spectroscopy experiments were used to calculate the specific conductivity, σ, of each individual glass type by dividing the measured conductivity with the cell constant (electrode area/sample thickness), usually of ca. 0.015 m. The specific conductivity as a function of frequency for EUC and PET glass, the end members of the polymerized Li-alumosilicate glass series, are plotted in figure 3 in comparison to the depolymerized glasses DG1 and DG2.
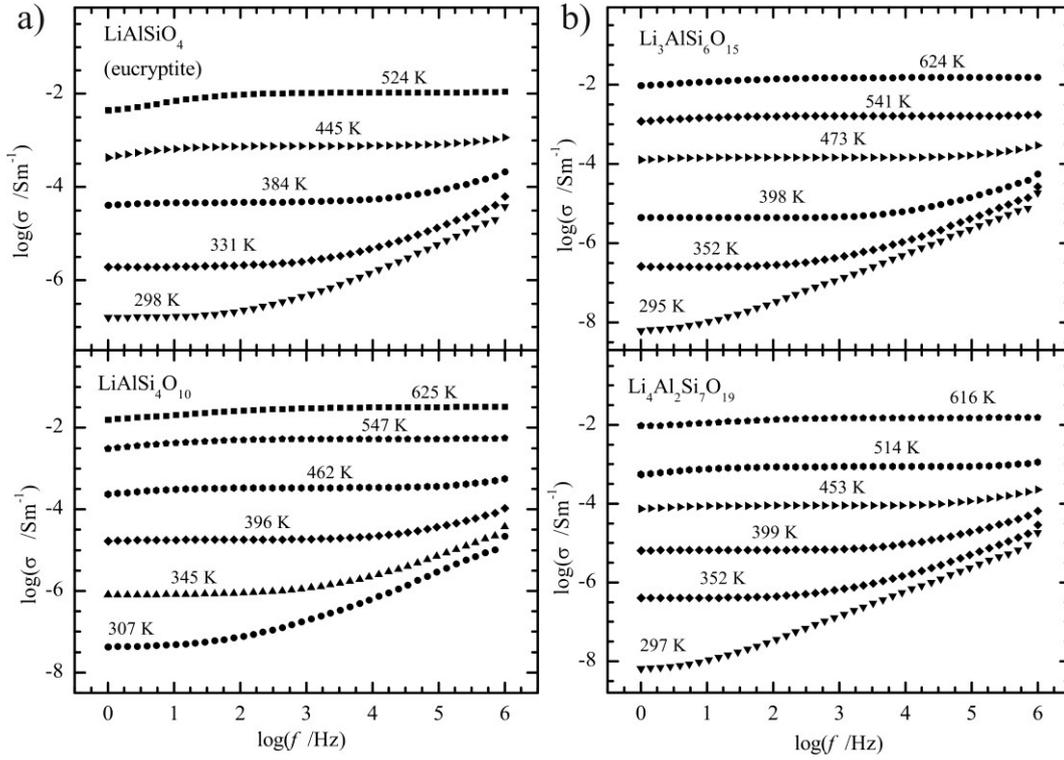
Figure 3: Examples of conductivity plots of polymerized (a) and depolymerized (b) lithium alumosilicate glasses.

Conductivities recorded during the heating and the cooling cycles agree within the 0.10 log units. The specific DC conductivity, σ_{DC}, has been read out from the center of the low frequency DC-conductivity plateau in the plot of the logarithm of the real part of σ vs. logarithm of frequency for each temperature. For each composition the data show a linear dependence of $\log(\sigma_{DC}T)$ on reciprocal temperature in the whole temperature range, i.e. following an Arrhenius relation

$$\sigma_{DC}T = A_0 \exp\left(\frac{-E_a}{RT}\right) \tag{6}$$

where A_0 is the pre-exponential factor and E_a is the activation energy for ionic conduction. The derived temperature dependent conductivity data for all glasses are given in Appendix 5.A to 5.D for polymerized and 5.E to 5.G for depolymerized glasses.

Within the series of polymerized glass the individual $\sigma_{DC}T$ values varied by less than 1 log unit at ~300 K (cf. Fig. 4). A systematic decrease of conductivity from the silica- poor EUC (LiAlSiO$_4$) towards the silica-rich PET (LiAlSi$_4$O$_{10}$) glass is evident. For the depolymerized glasses the differences between the specific conductivities were smaller (within $\approx$ 0.25 log units at 440 K), due to a smaller variation in lithium concentration in these glasses. The activation energies for the polymerized glass series vary between 66.4 and 70.4 kJ/mol (see table 1). The activation energies E_a for the depolymerized glasses were distinctly higher, with values from 76.5 to 78.1 kJ/mol.
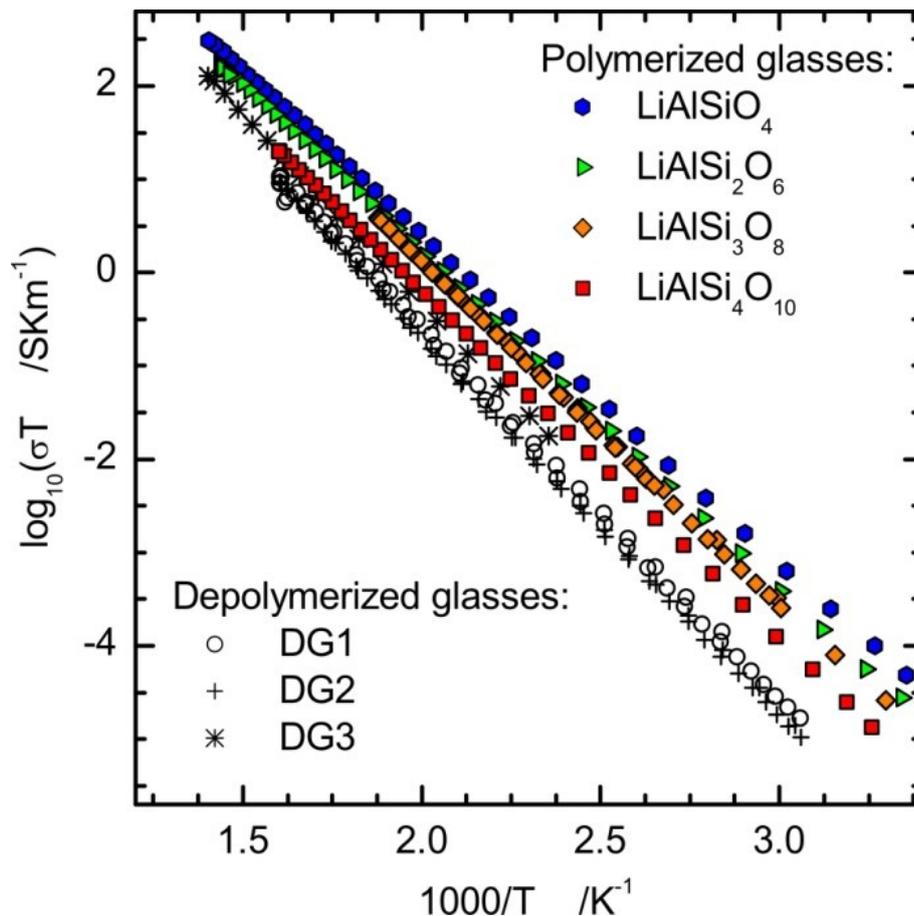
Figure 4: Arrhenius plot for dc electrical conductivity of polymerized and depolymerized glasses. For clarity only the heating cycle for all samples is shown. Data trends are coinciding for cooling cycle measurements.

To compare the diffusion characteristics of the materials diffusion coefficients were calculated with the Nernst-Einstein-Equation [48], [49], [46]:

$$D_{DC} = \frac{\sigma_{DC,spec.} \cdot k \cdot T}{N \cdot q^2}$$
(7)

D_{DC} corresponds to the self-diffusion coefficient of lithium ions. It is calculated from the specific DC conductivity of the sample ($\sigma_{DC, spec.}$), temperature T, the Boltzmann constant k, the charge carrier concentration N and the charge of the diffusing ion q. Charge carrier concentrations are calculated from glass density and lithium content by assuming a statistical distribution of lithium ions in a macroscopic view. The calculated diffusivities are shown in figure 6.

1.5.3 The Raman data on glass structure

The Raman spectra of the polymerized glasses are of good quality and reproducibility. Raw spectra after temperature and baseline corrections are shown in figure 5a. All spectra exhibit three complex bands in the low- and high-frequency regions, centered around 490, 800 and between 950 to 1200 cm^{-1}. With increasing silica content for polymerized glasses (EUC to PET) the low-frequency band is slightly shifted to lower wavenumbers, while high frequency bands are shifted to higher wavenumbers. Raman spectra of depolymerized glasses show the same behavior although less pronounced due to less distinct compositional disparities.
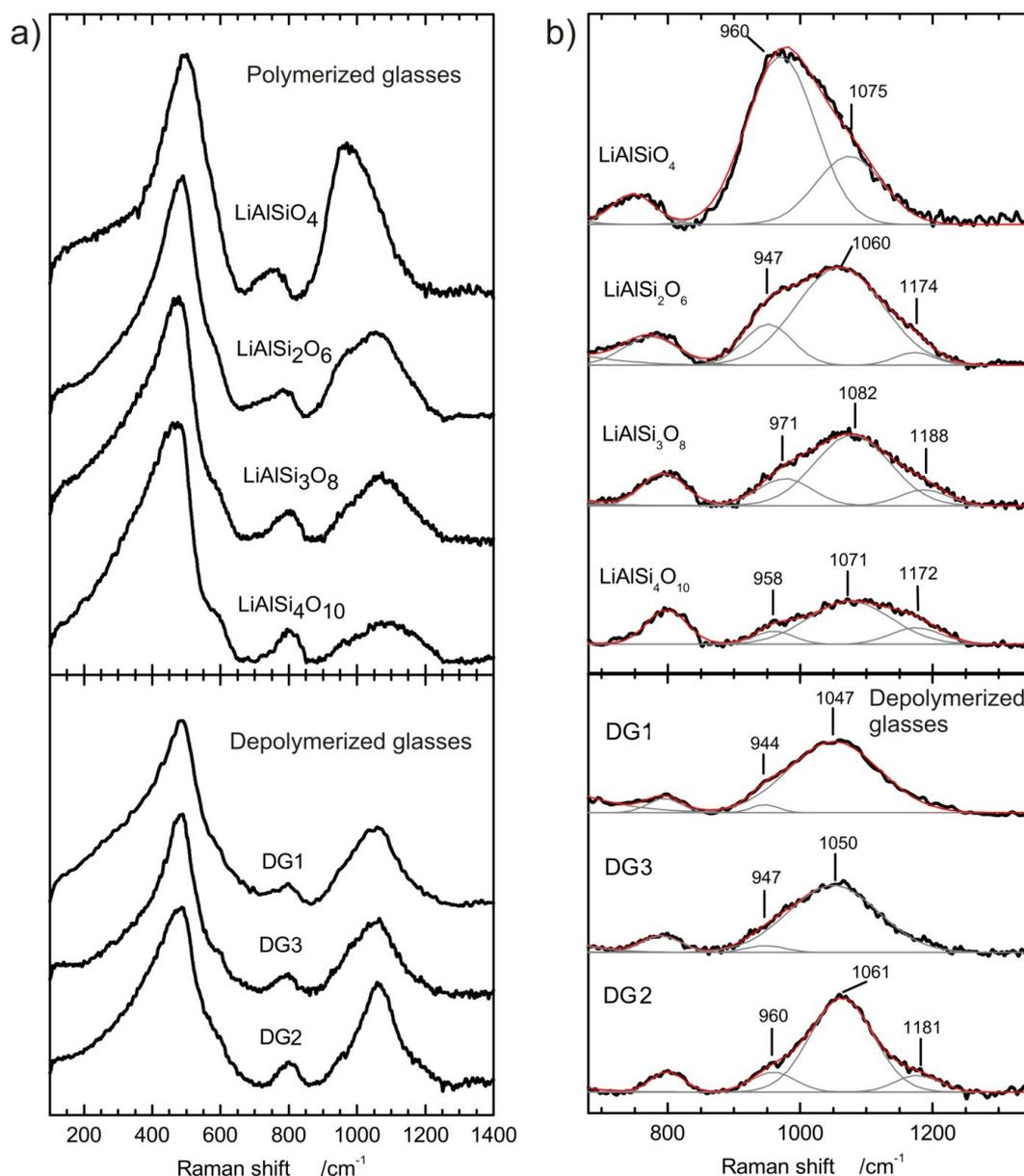
Figure 5: Raman spectra of polymerized (above) and depolymerized (below) glasses after baseline and temperature correction. a) Raman spectra of polymerized (above) and depolymerized glass (below) series after baseline and temperature correction. Spectra of both series have been arranged with respect to the increasing silica content and are scaled to same high of the most intense peak at 496 cm^{-1}. b) Deconvolution of the high energy region of the spectra, originating from T-O stretching vibrations, by Gaussians in order to identify characteristics of the glasses. The peak at highest wavenumber represents SiO$_4$-tetrahedra connected to four SiO$_4$-tetrahedra (Q^4 species). A shift of the peak position towards lower wavenumbers is due to connections of tetrahedral to AlO$_4$-tetrahedra tetrahedral and/or non-bridging oxygen.

The spectra were fitted using Gaussian functions in a non-linear curve fit. Following the structural models of Mysen and McMillan [50], [28], [27], [51], the minimal number of Gaussians

was applied to fit the spectra shape in the range from 200 to 1400 cm^{-1}. Generally the fit reproduced the experimental data with the coefficient of determination R^2 better than 99.8 % and the reduced chi square in the order of 10^{-4}. Fitted and deconvoluted high-energy regions (from 700 to 1400 cm^{-1}) are shown in figure 5b, and the Gaussian profile functions reflect the type and abundance of network-building structural units present. All the conclusions about the structures are made with the assumption of equal Raman scattering cross-section for all postulated structural units.

The low-frequency band was assigned to transverse motions of bridging oxygen atoms in T-O-T (T = Si,Al) configurations [51]. This broad band can be described as a combination of transverse vibrations of the fully polymerized Si-O-Si and Al-O-Si network and, in the case of the depolymerized glasses, interactions with structural units containing non-bridging oxygen atoms [52]. In lithium alumosilicate glasses Al has an effect comparable to NBOs on band positions. The center of the intensive band is close to ~430 cm^{-1} for polymerized glasses with high Si-content (FSP and PET and shifts towards 500 cm^{-1} for glasses with higher Al-content (EUC, SPO). A similar shift is observed when NBOs are introduced in the aluminosilicate structure.

The band at ~800 cm^{-1} can be assigned to vibration movements of silicon and aluminum in the network with a high cation and low oxygen displacement [52]. This band is centered at ~800 cm^{-1} for all glasses with exception of EUC (760 cm^{-1}) and SPO (782 cm^{-1}). The trend indicates that at higher alumina-to-silica ratio a lower bonding strength of Al-O in comparison to Si-O bonds leads to the vibration mode appearing at lower wavenumbers.

Table 3: List of Gaussian replicas used in deconvolution of the unpolarized Raman spectra of each considered composition. Each peak position has been fitted with the less than 10 % uncertainty.

	$LiAlSiO_4$	$LiAlSi_2O_6$	$LiAlSi_3O_8$	$LiAlSi_4O_{10}$	DG1	DG2	DG3
Low-energy region	333	338	385	310	-	-	-
(cm^{-1})	-	432	-	432	400	403	438
	496	490	472	480	472	490	490
	-	584	589	595	595	601	600
High-energy region	760	782	800	800	800	806	794
(cm^{-1})	960	947	971	958	944	960	947
	1075	1060	1082	1071	1047	1061	1050
	-	1174	1188	1172	-	1181	-

The high-frequency region between 900 and 1200 cm^{-1} was deconvoluted using two Gaussians in the case of EUC glass, DG1 and DG3 or three Gaussians in the case of other considered compositions (Fig. 5b). The list of the Gaussians used in modeling is given in table 3. The high-frequency Raman band predominantly arises from stretching vibrations of Si-O, modified by Al in neighboring tetrahedra. Based on studies on alkaline and earth-alkaline alumosilicate glasses [50], [28], in glasses without non-bridging oxygens the high-frequency region consists a combination of up to four main types of symmetric vibrations, defined by the number of neighboring $AlO_4^{(-)}$ tetrahedra connected to a SiO_4 tetrahedron [28]. Following the terminology well established for structural types in pure silicate glasses, the corresponding species can be described as $Q^n(x$ Al) where n characterizes the number of bridging oxygen and x the number of Al in the neighboring tetrahedra [51]. In Li-containing Al-Si-O glasses the peak ~950 cm^{-1} represents the structural unit where one Si-O tetrahedron is connected with three neighboring Al^{3+} via oxygen bridges, (SiO)-Si(OAl)$_3$, or (Q^4(3Al)). The (SiO)$_2$=Si(OAl)$_2$, or (Q^4(2Al)) gives rise to the peak between 1000 and 1060 cm^{-1} and the peak centered at ~1170 cm^{-1} relates to the vibrations of the (SiO)$_3$≡Si(OAl), (Q^4(1Al)). This is consistent with the expectation that a higher number of $AlO_4^{(-)}$ tetrahedra connected to a SiO_4 tetrahedron leads to a decrease in frequency, as Al-O

bonding is weaker in comparison to a Si-O bond. This effect is even more pronounced in depolymerized glasses which in addition contain NBOs, as the neighboring non-bridging oxygen atoms weaken the network bonds in higher degree than Al. [51], [52].

In the series of polymerized glasses the results of structural analyses are consistent with the Al-avoiding principle after Löwenstein [30] and a strong tendency for alternating Si-O-Al structure. The structure of EUC is expected to comprise of alternating Si- and Al-tetrahedra, which would correspond to a Q^4(4Al) structural unit. In the high frequency region of the EUC spectrum the strong peak centered at ~960 cm^{-1} would correspond to this unit, while the additional weaker component at ~1075 cm^{-1} arises from Q^4(3Al) as a result of deviation from Si-O-Al alternation due to the existence of a small number of Al-O-Al bonds. In the spectra of SPO, FSP and PET, the Gaussians centered at ~ 950, ~1070 and ~1170 cm^{-1}, can be generally assigned to Q^4(4Al), Q^4(3Al) and Q^4(2Al) units, respectively (see table 3). The broadness of individual Gaussians however, indicates that various combinations of the main structural units are present and give rise to the discrete peaks which cannot individually be defined in the spectra.

In the depolymerized glasses DG1-3 the number of Gaussian peaks and peak positions differ slightly in comparison to the polymerized series. In depolymerized glasses the silica network is modified by both $AlO_4^{(-)}$ tetrahedra and the NBOs. That means that the high-energy band is far more complex in comparison, with a combination of modes arising from depolymerized silica tetrahedra with one to two NBOs as well as the Al-O-Si species. It is not possible to resolve the overlapping distinct modes of individual species and their combinations with the non-linear curve fit. Keeping this in mind, the high-frequency parts of the depolymerized glasses spectra are comparable with the polymerized series. The spectra fitted with Gaussians reveal broader bands which would generally comprise the combinations of Q^3 with Q^4(3Al) and Q^4(2Al) with the possibility of very weak contribution of Q^2 species. The third Gaussian was needed for fitting the broad additional

peak ~1180 cm^{-1} in DG2 spectra which might correspond to the combination of Q^4 and Q^4(1Al).

1.6. Discussion

1.6.1 Diffusion in oxide glasses

Several models were proposed in the past to describe ion motion in oxide glasses, e.g. the Anderson and Stuart (1954) [53] model, the weak electrolyte model of Ravaine and Souquet 1977 [54] and Ingram et al. 1980 [55], the modified random-network (MRN) transport model of Greaves et al. (1991) [56], the jump relaxation model of Funke (1991) [13], [57], and the site mismatch model of Bunde and Ingram et al. (1991) [58]. An overview of these models is given by Chakraborty (1995) [59]. Ideas of the latter two models are combined in the concept of mismatch and relaxation (CMR) of Funke (1998) [60], and are further elaborated in the universality concept of Funke et al. (2010) [61]. Ion-conducting materials with quite different kinds of disordered structures have been found to show striking similarity in their conductivity spectra. The first universality is that, at high temperatures, plots of log conductivity vs. log frequency yield features as shown in figure 3 which can be considered as a fingerprint of activated ionic hopping along interconnected sites [62], [8], [63]. At low temperatures, e.g. in the cryogenic range, the dielectric loss function, ε'' is virtually independent of both frequency and temperature other. This so-called "second universality" is suggested to reflect non-activated, strictly localized movements of the ions [64], [65], [66].

In structural disordered materials mobile ions do not longer experience a static energy landscape as in crystals, but rather single-particle potentials that are time-dependent and non-periodic. As a consequence, movement of ions is not random, but highly correlated [61]. A key issue is to relate the observed dynamics of ions with the structure of

the potential landscape. The mobility of lithium ions in oxide glasses is determined by short and long range order effects. The short range movement is affected by the direct structural environment of the lithium cation. The activation energy needed for a movement to another place in the structure depends on the coordination of lithium. The lower the energy level of the current location is in comparison to neighboring sites, the higher is the activation energy needed to leave this place. If the ion leaves the place, it can remain at the new position and the surrounding matrix adapt to the new situation (relaxation process) or the ion jumps back to the origin place. A series of successful jumps leads to long range transport phenomena and ions can be transported through the material. This can be supported by forming percolation paths. A jumping lithium ion releases a free site which can be filled by another Li^+. A hopping mechanism is established leading to correlated jump phenomena. Following the jump relaxation model, the movement through these percolation paths are the main transport mechanism for fast ion conductors. The introduction of high field strength cations like Ca^{2+} or Mg^{2+} leads to a blocking of these pathways and, hence, in a dramatic decrease of the conductivity. The importance of these percolation pathways makes this kind of diffusion mechanism generally prone to blocking effects [67], [12].

1.6.2 Diffusion of lithium in the system $Li_2O - Al_2O_3 - SiO_2$

The ionic conductivity is affected by both, the mobility and the concentration of the charge carriers. To get insights to the dynamic of lithium, diffusion coefficients were calculated using the Nernst-Einstein-Equation [48], [49], [46]:

$$D_{DC} = \frac{\sigma_{DC,spec.} \cdot k \cdot T}{N \cdot q^2} \qquad (8)$$

D_{DC} corresponds to the self-diffusion coefficient of lithium ions. It is calculated from the specific DC conductivity of the sample ($\sigma_{DC, spec.}$), the temperature T, the Boltzmann constant k, the charge carrier concentration N and the charge of the diffusing ion q. Charge carrier concentrations are calculated from glass density and glass composition by assuming a statistical distribution of lithium ions. The calculated diffusivities are shown in Fig. 6.
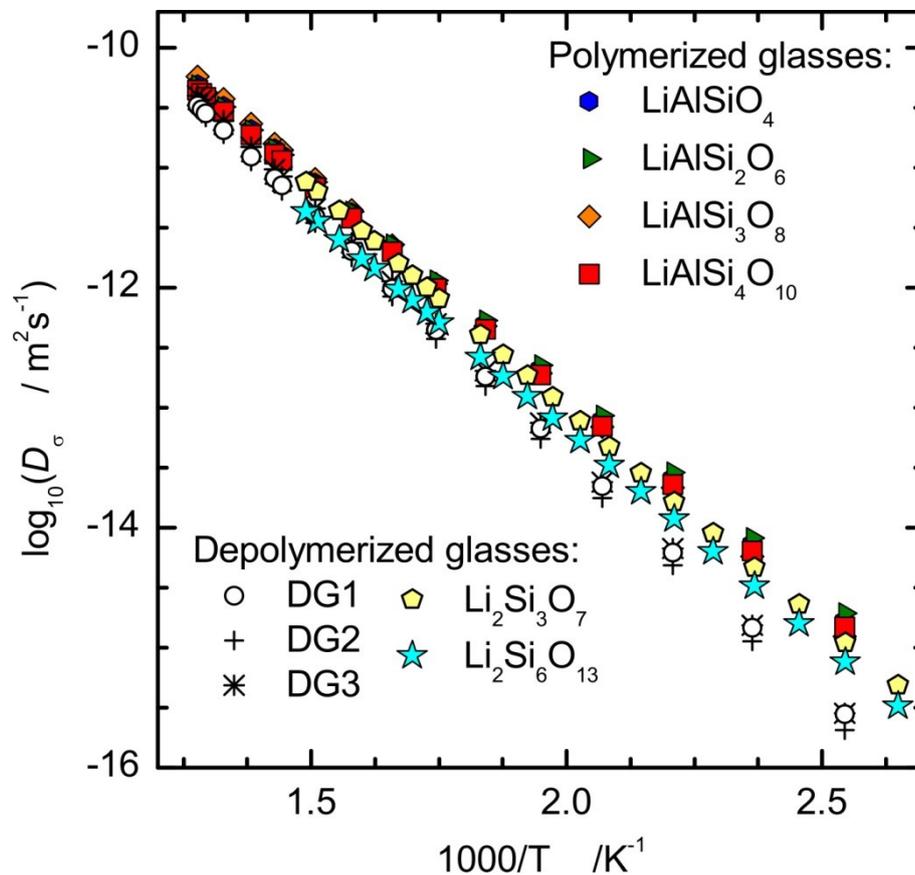
Figure 6: Temperature depending diffusivities for polymerized and depolymerized glasses calculated from $\sigma_{DC}T$ values with the Nernst-Einstein equation.

Diffusivities for the different polymerized glasses are practically indistinguishable. There appears to be a trend of slightly increasing activation energy for lithium diffusion with increasing silica content of the glass, but the effect is rather small compared to the error of E_a (table 2). Lithium diffusivity strongly decreases when introducing NBOs in the

aluminosilicate glass matrix, e.g. by 0.6 log units from FSP to DG2 and DG3 at 400 K (Fig. 7a). Comparison to data for lithium tri-silicate (from Bauer et al. 2013) [24], which has a similar silica content of 75 mol%, indicates a minimum of lithium mobility for systems containing both types of oxygen, NBO and Al-O-Si. The activation energy for diffusion follows the same trend exhibiting a maximum for the depolymerized alumosilicate glasses (Fig.7b). Hence, the differences in lithium mobility increase with decreasing temperature. It is to emphasize, that all impedance measurements were done at temperatures at least 50 K below the glass transition temperature. At these conditions the other constituents of the glass structure (Si, Al, O) can be considered as immobile. Additionally it needs to be stressed that concentrations of other alkalis is below 1% of the lithium concentration and, hence, the conductivity data and the derived diffusivity coefficients for lithium represent solely structural differences in the materials.
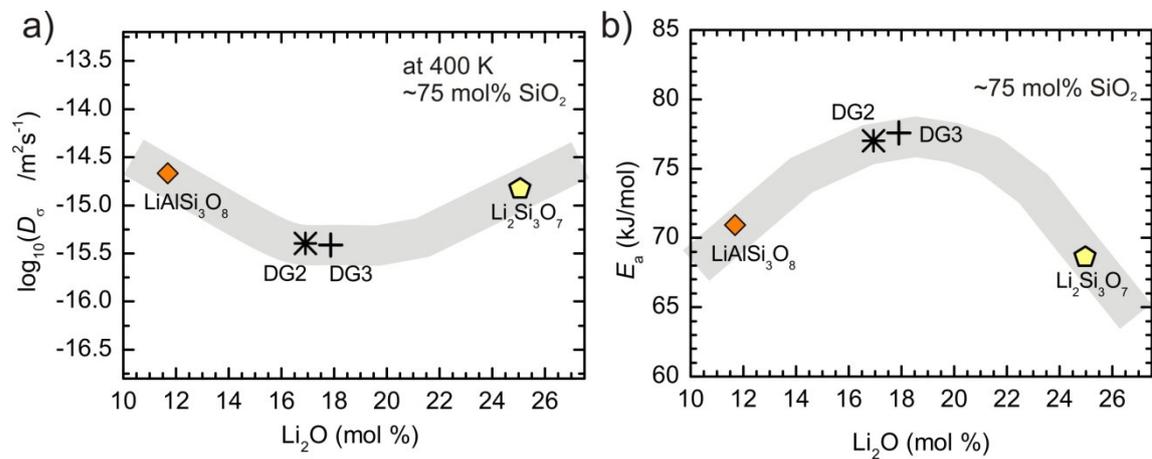
Figure 7: Diffusion coefficient (a) and activation energy (b) depending on Li_2O content for FSP, DG2, DG3 and lithium trisilicate glass, having a nearly constant SiO_2 content.

1.6.3 Implications for lithium migration paths and glass structure

The Raman spectra are consistent with a statistical distribution of AlO_4^- tetrahedra in the network of polymerized lithium alumosilicate glasses. The aluminium avoiding principle theoretically leads for EUC (chemical composition $LiAlSiO_4$) to an alternating sequence of SiO_4- and AlO_4 -units, means each Si-tetrahedron is connected to four Al-tetrahedra and *vice versa.* Lee and Stebbins proofed Al-O-Al (and subsequent Si-O-Si) structural units in alkaline alumosilicate glasses with an Al/Si ratio of 1 by ^{17}O 3QMAS NMR analyses [Lee 2000], but this gives only minor change of this global picture. Thus, in first approximation all oxygen atoms are equal in EUC with a formal charge of -1/4 and potential sites for lithium in the structure are determined by the flexibility of T-O-T bond angles. Incorporation of SiO_2 in the glass leads to an increase of the fraction of Si-O-Si, means oxygen with formal charge of 0. In PET ($LiAlSi_4O_{10}$) glass the fraction of Si-O-Si over total oxygen formally reaches a value of 0.6. Assuming a statistical distribution of types of oxygen, there is still a very high probability for interstitial sites for lithium with 2-3 oxygen bonded to Al. This results in low activation energies for lithium diffusion and the decrease in relative abundance of Si-O-Al may explain the slight increase of E_a with silica content.

On the other hand, for alkali silicate glasses there is strong evidence for an unmixing of structural units on the nanometer scale (see discussions in Bauer et al. 2013) [24]. A separation of Li-rich regions within a Si-rich matrix was observed by different experimental methods [26], [76], [78], [68], [69], [70], [22], [71] as well as in theoretical modeling [26], [72], [73], [74], [75]. Analyses of Li−NBO and Li−BO bond lengths and spatial arrangements by NMR [26], [70], [22], neutron diffraction [76], [69], [77], MDS [26], [72], [73], [74], [75] and the low coordination number of Li [72], [77] strongly point toward elongated channel-like arrangements of the Li-rich regions. Quasielastic neutron scattering results corroborate the

formation of cation channels for fast ion diffusion in the static Si matrix as a feature of all alkali binary silicates [78]. Preferential Li cation migration paths can thus be formed between individual interconnected Li-rich regions by cation hopping over the percolation barriers, localized between the depolymerized Q species. As a consequence, activation energy for lithium diffusion is low, compared to the polymerized alumosilicate glasses.

Although systematic investigation by other spectroscopic methods than Raman is missing, there is no expectation that such kind of phase separation for the depolymerized alumosilicate glasses occur. The driving force for clustering in the alkali silicate glasses is the optimization of oxygen polyhedra around lithium. Oxygen atoms connected to two silicon (Si-O-Si) have relatively small electron density and, therefore, they are not well suited to coordinate lithium ions. In contrary, oxygen bond to aluminum (Si-O-Al) is much better suited to participate in such lithium polyhedra, as evidenced by the findings on polymerized alumosilicate glasses. Even in the glass with lowest aluminum content, DG3, the fraction of Si-O-Al to total oxygen is 0.23 and the total fraction of formally charged oxygen is 0.36. Furthermore, partial depolymerization of the network enhances the relaxation capability of oxygen around lithium ions and, therefore, the creation of deep local potentials. The transition of lithium ions from such regular sites to interstitial sites, requires a high activation energy as indicated by the temperature dependence of electrical conductivity for the depolymerized alumosilicate glasses.

1.7. Conclusion

The impedance spectroscopic and Raman spectroscopic analyses of series of four polymerized and three depolymerized lithium alumosilicate glasses reveal information about the diffusion characteristics of lithium and their structural and compositional dependence. While polymerized alumosilicates are fast lithium ion conductors with a wide distribution of lithium percolation paths, the introduction of an excess of network modifiers leads to depolymerization and a drop in conductivity and lithium diffusivity. This is explained with the strong interaction of lithium with the NBOs creating deep local potentials for lithium and, hence, high barriers for the transition of lithium ions into interstitial sites. When decreasing the concentration of aluminum, the glasses tend to unmixing on the nano-scale, driven by clustering of lithium ions and NBOs. As a consequence, high lithium mobility can be achieved by percolation along channel-like nanostructures. Thus, although lithium diffusivities and activation energies for lithium diffusion are similar in polymerized lithium alumosilicate and in lithium silicate glasses, the network topology and the migration paths differ strongly. The similarity of the transport properties indicate that the barriers for lithium jumps between regularly occupied sites and interstitial sites are comparable for both types of glasses.

Chapter 2: Axial pressure cell development

2.1. Introduction

Physical and chemical characteristics of materials can depend strongly on their mechanical status. While bulk material show a uniform behavior in terms of ionic conductivity, activation energy and diffusion constant (as long as no anisotropic effect occurs), mechanical treated material can show another behavior. By milling and sintering new features like large pores, grain boundaries or other disturbances can be introduced in the material. This can have both, positive or negative effects on transport properties. The diffusivity of mobile species can be increased or decreased in comparison to crystalline and glassy bulk materials depending on the material characteristics [79], [80]. An example for this effect is given by Kuhn et. al. with spodumene glass. While the diffusivity of lithium in crystalline spodumene was enhanced by milling, the diffusivity is decreased for glassy spodumene [22].

The comparison of ionic conductivity in materials of different form is conducted by measuring the bulk materials, mill, press (and optional sinter) the powder and determine the conductivity characteristics of the powdered material afterwards. This approach is suitable to determine the material characteristics but it misses out the information about the pressing and sintering process. This information can be helpful to understand the grain/bulk interaction and, in general to improve the pressing and sintering process. To get such information about the pressing process of powdered materials, a new axial pressure cell was developed.

2.2 Development of axial pressure cell

2.2.1 Objectives

The aim of the construction of the new axial pressure apparatus was to establish a method to measure the pressure, temperature, volume change and impedance spectra (IS) at the same time. This *in situ* impedance spectroscopy allows to follow the pressurization process directly, while other methods only provide data before and after the compaction. Such kind of *in situ* methods are known in literature, but only for multi-anvil presses [81] including a very small sample volume or in a piston cylinder design [82] using a pressure medium, leading to isotropic pressure distribution or a small sample volume [83], [84]. The now developed sample cell is bigger in comparison and allows to measure a larger sample volume without any additional pressure medium. Furthermore the pressure is only applied in axial direction due to two coplanar pistons and a sample chamber limited by a ceramic ring.

2.2.2 Press setup

The technical setup of the press is shown in figure 8. The press frame (1) is made of two aluminium plates (25 x 25 x 3 cm) connected by 4 aluminium bars with screw connections. On the top plate an oil hydraulic piston press is installed which applies pressure by a pressure piston (2) passing through the top plate to two steel pistons. The upper pistons and the hydraulic stamp (3) are isolated by a conical shaped PVC adapter (4) to ensure electrical isolation of the sample material and the pressure frame. The applied pressure is measured by a load cell (20) inserted centrally into a depression in the bottom plate of the aluminium frame. While the hydraulic is controlled by the oil pressure, the load cell in combination with a HBM measuring amplifier (1- MX840A), allows measuring the applied

sample pressure with an accuracy up to 0.05 kN. Both pistons have to be positioned in the center of the frame to allow a uniform pressure application to the sample. Therefore the upper piston is centered by the conical PVC adapter to the oil hydraulic piston. The lower piston is connected by a thread to a circular steel adapter (19), matching the diameter of the load cell to ensure central positioning. The temperature is controlled by a self-build vertical oven (11) mounted at a frame bar and two K-type thermocouples. To protect the oil hydraulic pressure and the load cell from high temperatures two flange like cooling devices (6 and 17) are connected directly to the upper and lower piston while the lower cooling device is electrically isolated by PTFE (15). Between the pistons a ceramic sample cell (12) contains the sample (11). Impedance spectroscopy data can be derived with the help of two contacts at the upper (9) and lower (16) piston while the sample thickness is measured by two way-sensors (5) applied at the upper cooling flange. Fig. 7 also shows a quartz tube (13) with gas in- (8) and outlet (18) through tighten PTFE flanges (7 and 14). These parts are to be integrated into the apparatus and not used for the following measurements and descriptions. In the future the atmospheric conditions might be controlled to analyze the influence of water vapor, acid or alkaline gases.
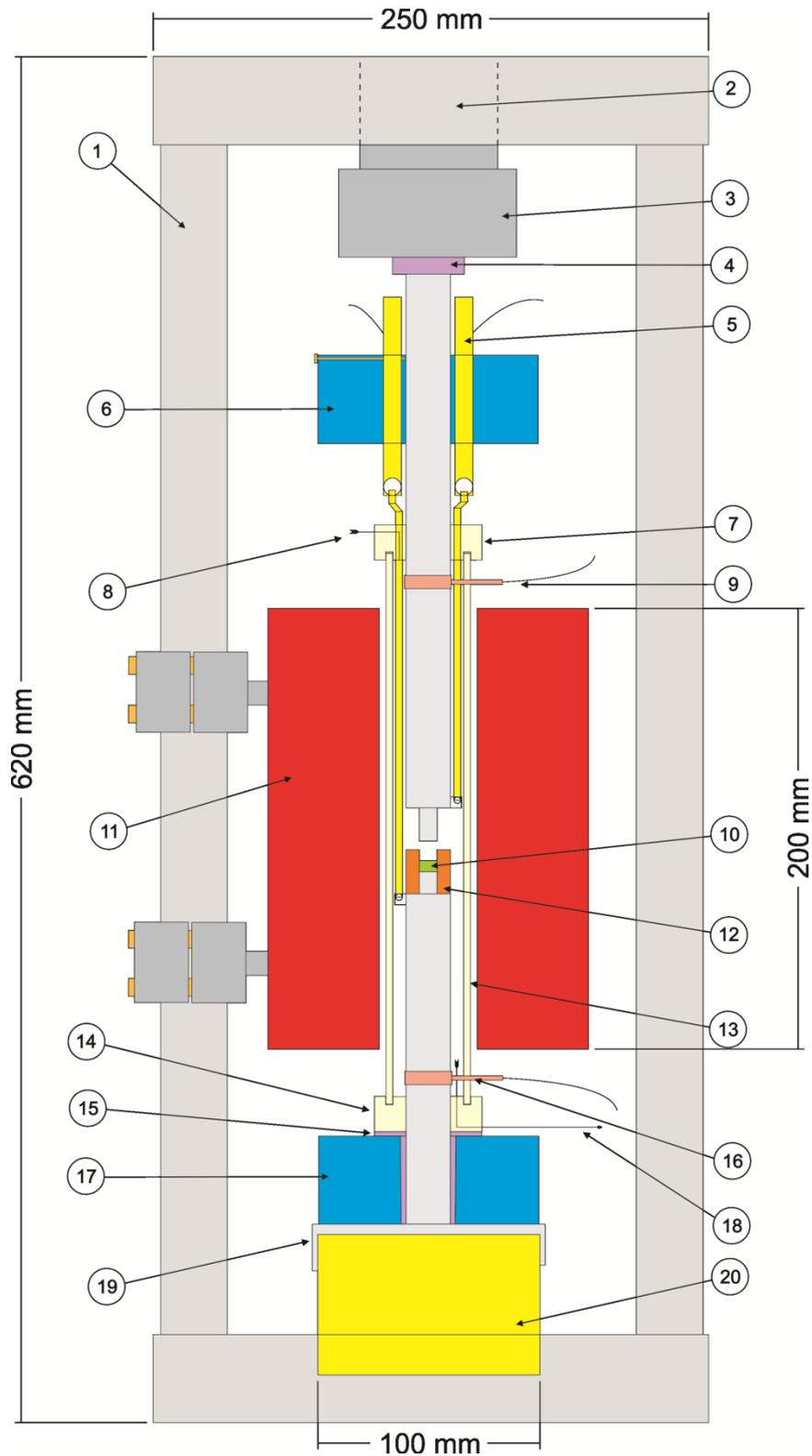
Figure 8: Technical drawing of the developed axial press. 1 = aluminium press frame, 2 = hydraulic stamp, 3 = pressure stamp, 4 = elec. isolation, 5 = way sensor, 6 = cooling device, 7 = PTFE flange, 8 = gas inlet, 9 = IS contact, 10 = sample material, 11 = vertical oven, 12 = ceramic ring sample cell, 13 = quartz tube, 14 = PTFE flange, 15 = elec. isolation, 16 = IS contact, 17 = cooling device, 18 = gas outlet, 19 = piston base plate, 20 = load cell

2.2.3 Control of sample characteristics, temperature and sample thickness

The self-build vertical oven is made of spiraled Kanthal-wire wrapped around an alumina cylinder. To control the oven temperature, a cavernous ceramic bar is placed between the heating wires and the central cylinder. A jacket thermocouple (K-Type) is be placed in during operation to control the oven temperature. A bifilar arrangement of the heating wire minimizes the development of electrical fields which possibly induce a current in the sample material. This may disturb the impedance measurements. The wires were enclosed by refractory cement (Feuerfestmörtel, Quick-Mix) to protect the oven against short circuits. To ensure that cementing and mechanical stress did not generate any damage to the wire, the expected and real resistivity was compared. 20 m of the used Kanthal-wire (specific resistance 1.45 $\Omega mm^2 m^{-1}$) with a diameter of 1.1 mm should show a direct current resistance of 30.5 Ω. After cementing, a heating element resistance of 29.1 Ω was measured. The disparity in resistance does not indicate any shorts in the wire due to cementing. For fastening of the wire ends those were turned to double wires for about 30 cm on both ends. If this difference in length is taken in consideration, the theoretical resistance decreases to 29.6 Ω and is even more according to the measured value indicating a correct manufacturing process. The heating element was placed in an outer cylinder made of aluminum that provides stability and connectors for the power supply and the mechanical connection to the metal frame of the axial press. The gap in between was filled closely with rock wool material (Superwool Paper, Morgan) for thermal isolation.

The temperature distribution of the oven was determined by inserting a 20 mm diameter V2A steel bar with a centrally inserted jacket K-type thermocouple. At a constant electrical power, the thermocouple is moved through the central part of the oven to record the temperature distribution. The maximum temperature was found to be around 160 mm above the bottom line of the oven indicating a 32.5 mm displacement in upper direction

compared to the center of the oven. During this test the oven was open at the top and closed at the bottom. This might have induced a stack effect in the oven by convection what might explain the displacement. Nevertheless, the sample was positioned at this point as best practice.

Two thermocouples (K-type) are inserted into the oven to control the sample and the oven temperature during the experiments. With this arrangement measurements between ambient temperature and 500 °C were carried out. So far, higher temperatures are not suitable because a sufficient heat transport through the upper piston tends to mechanically weaken the PVC isolation despite active cooling. At high temperatures the oil hydraulic press at the top and the load cell at the bottom of the apparatus are protected against high temperatures by water cooling flanges made of brass. They are directly reversible press-connected to the pistons by small screws and cool the top and the bottom part beside the oven. The temperatures of the oven and the sample are recorded by a self-build logging unit. The relative error of the temperature measurements of the combined device is below 1 K for the oven temperature. Due to variations in thermocouple placement and oven positioning relative to the constant temperature zone of the oven, a higher error for the sample temperature has to be assumed. Remarking the temperature distribution experiments, a relative error of ± 1% or ± 5 K at 500 °C is assumed.

To detect the sample thickness, two LVDT way sensors (WI/10mm-T, Hottinger Baldwin Messtechnik GmbH) are applied into the top cooling flange. Two metal slots and the top and bottom piston are connected to the displacement transducers by quartz or ceramic bars. Due to their minor linear thermal extension quartz bars were preferred. In first experiments the electrical connection of the way sensors directly influenced the impedance measurements. An alternative way to detect the sample thickness is to determine the lift of the upper piston in comparison to the lift without sample. This can be measured by a

micrometer caliper. First experiments showed that both ways are suitable, but mounted way sensors are much more accurate.
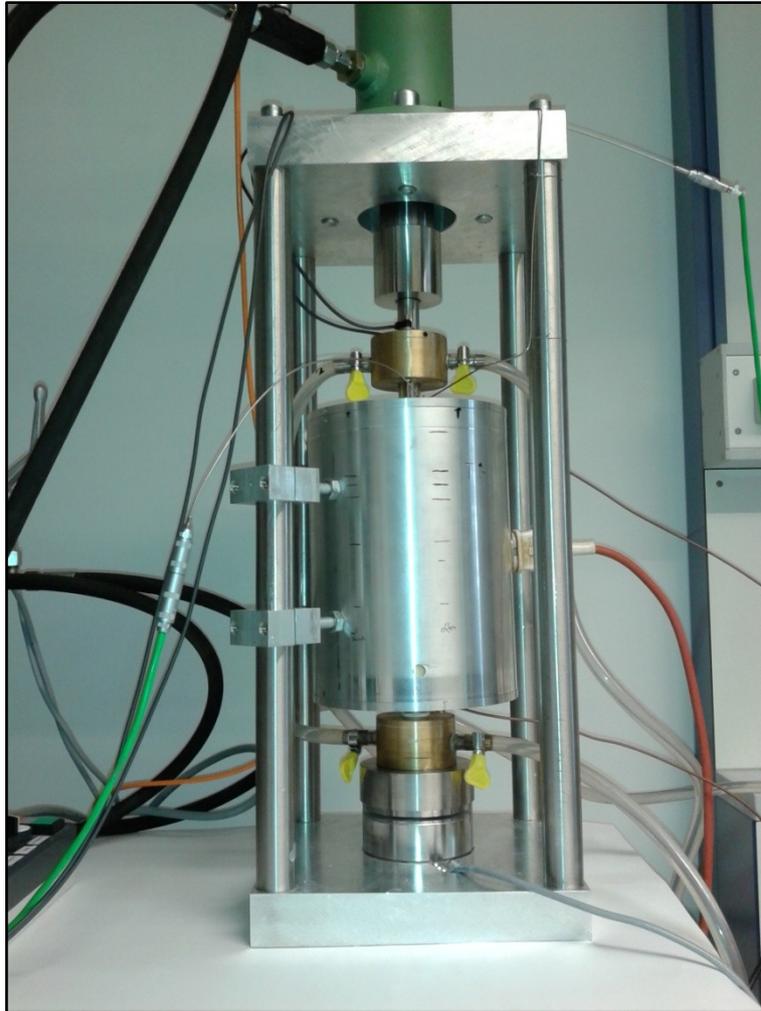
Figure 9: The axial press cell during an experiment

In Fig. 9 an experiment with installed way sensors and cooling flanges shows the practical application. Particularly in the first stages of the pressure experiments the weakest point of the cell was the sample material container. The ceramic ring showed mechanical weaknesses at high pressures. Due to this, a new sample cell design was necessary which is described in the following.

2.2.4 Sample cell design
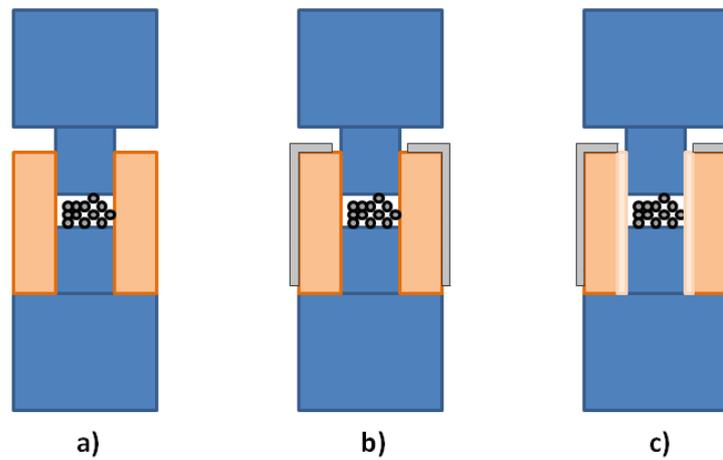
Figure 10: a) sample chamber with a ceramic ring made of alumina (brown), containing sample powder (dark grey) compressed by the steel pistons (blue), b) stabilized by a steel sleeve (light grey), c) stabilized by a steel sleeve and an added inner cylinder of crushable alumina (light brown).

In the first stage of development the ceramic ring tends to crack, splinter and even burst at higher pressures (cf. Fig. 10a). To reach higher pressures the ceramic ring has to be stabilized with an additional steel sleeve. It is important to ensure that the steel sleeve has only contact with the ceramic ring during the impedance spectroscopy measurements. An electrical connection to the upper or lower piston has to be excluded. A 0.5 mm distance between the steel sleeve and the lower, respectively the upper piston, was found to be sufficient for electrically isolation (cf. Fig. 10b).

While the stabilization prevents the splintering of the ceramic ring, cracks develop at higher pressure due to the lateral displacement of the sample material. The powdered material evolves into these cracks and the sample volume properties become unpredictable. To prevent the crack formation, a less hard border between the ductile sample material and the hard ceramic border was inserted. The chosen material is crushable alumina, an

aluminum oxide ceramic with 85 % of the theoretical density due to a lower sintering temperature. An inserted cylinder between the sample and the alumina ring provides a less harder border to absorb the powder horizontal expanding (cf. Fig. 10c).

A disadvantage of this technique becomes visible at higher temperatures and pressures. The less hard crushable alumina is mechanical more instable and reactions between the sample material and the border can occur. This can lead to sample contamination with aluminum oxide.

2.3. Axial pressure cell - method verification and proof of concept

As a proof of concept a set of *in situ* impedance spectroscopy measurements and sample material characterization was done to verify the axial pressure design.

2.3.1 Experimental setup of impedance spectroscopy measurements

Impedance spectroscopy measurements are possible in 4- and 2-wire contact procedures. In this apparatus the pistons act as electrodes for IS spectroscopy in 2-wire measurements. The pistons are directly connected to a ZG4 connecting station (Novocontrol) and an Alpha-A-Analyzer mainframe (Novocontrol). The electrical connection is done by twisted end copper wires at the pistons and BNC-connectors at the measurement instruments. An increase in connection quality became apparent by adding some silver paste at the piston-copper connection during the experiments. However the noise of the dielectric response at low temperatures is increased in comparison to the 4-wire standard sample holder used for bulk glass measurements. This problem disappears almost completely at temperatures higher than approximately 300 to 350 °C, if a higher conductivity is reached. Due to this,

the amount of applied sample material is crucial for this kind of experiments. If the sample thickness is too large to reach a sufficient absolute conductivity, the quality of spectra is insufficient for further interpretation. An insufficient spectrum quality can also be dedicated to a bad contact between the electrodes and the sample powder.

To enhance the interface quality between the pistons and the sample, one piece of gold foil was added at each piston in some experiments at the bottom and on top of the sample. This enhanced the quality of spectra in general, but leads to the problem of a less defined electrode surface area, because the foils are moving during press assembling and pressurization process. A solution for this problem could be a durable noble metal coating of the pistons with sintered platinum paste or comparable materials.

To test the performance of the apparatus, lithium tri-silicate glass ($Li_2O \cdot 3\ SiO_2$) was chosen as sample material. The material was chosen by availability and existing comparative conductivity data on glass plates. The glass was prepared by melting stoichiometric powder mixtures of high purity SiO_2 and Li_2CO_3. Afterward the homogenous material was crushed in a steel mortar and graded into fractions with different grain sizes by sieves of different mesh sizes. For the measurements a mesh fraction of 125 μm and smaller was used. Due to the relatively large inaccuracy of this process due to a missing lower limit, the powder was characterized by scanning electron microscopy and x-ray diffraction before and after the compaction (cf. *3.2*). Three compaction procedures were conducted with the as characterized starting material, with parameters shown in table 4.

The general approach for all three experiments was the same: At first, around 80 mg of the $Li_2O \cdot 3\ SiO_2$ sample material is filled into the ceramic sample cell. Then all other parts of the press are applied outside of the metal press frame. The combined sample and piston apparatus is placed into the press frame and a low pressure of about 0.3 kN is applied on the sample to stabilize the system mechanically. Now the sample is heated up to a certain

temperature (cf. Tab. 4: $T_{pressure\ cycle}$) at constant pressure. The pressure changes with temperature due to thermal expansion of the system. Until the experimental temperature is reached, the pressure is adjusted at a level about 0.3 to 1 kN by hand control of the oil hydraulic press. During this heating period, oven and sample temperature show a time shifted behavior because the system needs to be in steady state with the cooling to show constant temperature and pressure behavior. If this steady state is reached, the pressure is raised stepwise to the maximum while for each pressure step impedance spectra are recorded. If possible, the pressure is reduced stepwise after the experiment to ambient pressure to control on reversibility. The impedance spectra are recorded in the frequency range from 0.1 Hz to 1 MHz.

Table 4: Experimental parameter of the conducted axial pressure experiments.

Measurement	$T_{pressure\ cycle}$ / K	T_{max} / K	f_{max} / kN	p_{max} / kbar
Mess2	693	728	14.70	2.92
Mess3	743	743	21.00	4.18
Mess4	713	717	21.50	4.28

Corresponding to Bauer et al. [24], the glass transition temperature T_g for the lithium tri-silicate glass is 730 K. That means that measurement Mess3 was done 13 K above the glass transition temperature while the measurements Mess2 and Mess3 are carried out below T_g.

2.3.2 Sample material changes during compaction experiments

During the compaction the sample material might change its properties. These changes can influence the impedance spectroscopy measurements and is analyzed in terms of XRD and SEM. These changes can concern crystallization of the amorphous glass powder as well as

Chapter 2: Axial pressure cell development

changes of particle size and particle morphology. Changes in chemical composition are not expected but chemical contamination by interaction with sample cell material might occur.

2.3.2.1 X-ray diffraction results

The x-ray diffraction pattern were done with a Philips PW 1800 coupled with a secondary graphite monochromator. For the analysis Cu $K\alpha_{1,2}$ x-rays at 40 kV tube voltage and 40 mA tube current were used.

Both, the starting material and all compacted powders are amorphous and show no evidence of crystallization processes during the high temperature/high pressure compaction. The x-ray diffraction pattern given in Fig. 11 show no change compared to the fully amorphous starting material.
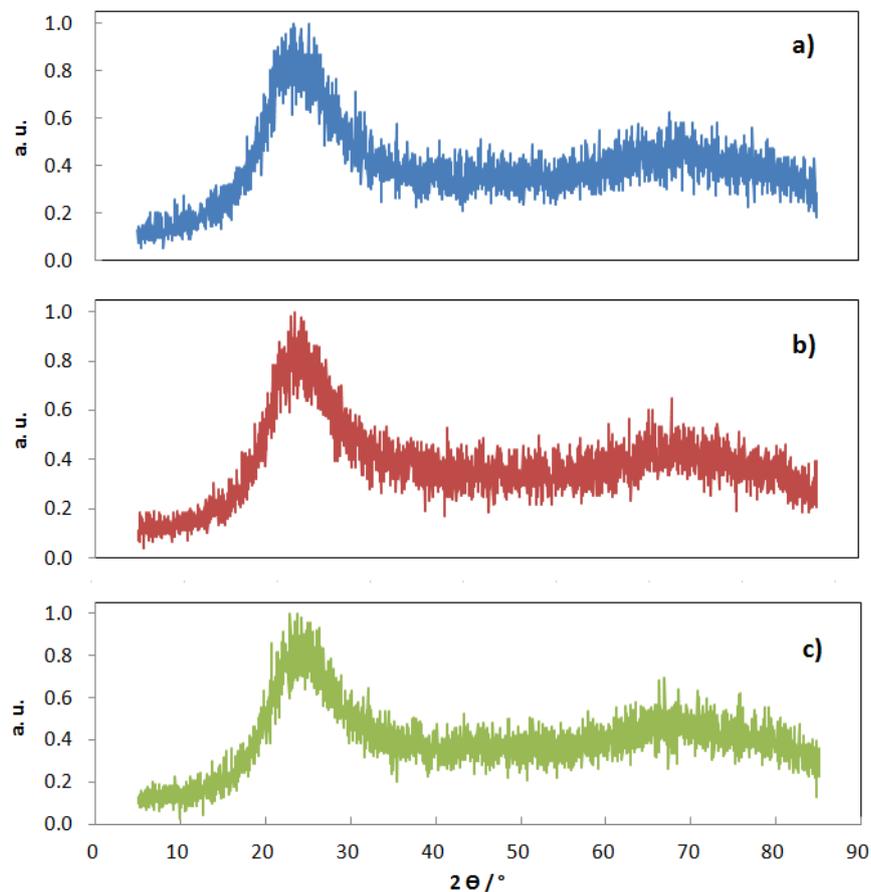
Figure 11: X-ray diffraction patterns of tri-silicate starting material (a), product of measurement Mess2 (b) and product of measurement Mess3 (c).

In contrary, the x-ray diffraction pattern after measurement Mess4 shows a crystalline component (cf. Fig. 12). All peaks can be clearly assigned to aluminum oxide. The explanation for this is a strong connection of the sample material to the crushable cylinder after the pressing process. Parts of the crushable alumina contaminated the sample during its removal from the sample cell.
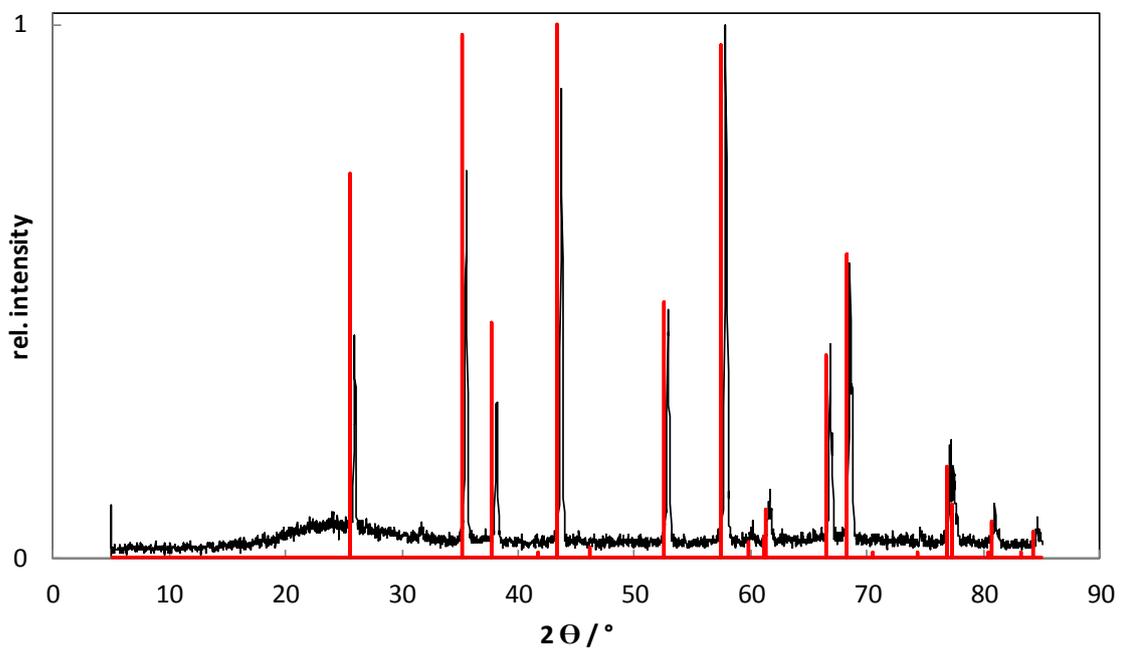
Figure 12: X-ray diffraction pattern after measurement Mess4 (black). Added are the x-ray reference pattern of aluminum oxide (red).

This could be confirmed by energy dispersive x-ray analysis (EDX). Al-containing material was found on the surface of the particles (cf. Appendix 5.H).

2.3.2.2. Scanning electron microscopy

The scanning electron microscopy (SEM) is used to determine the particle morphology and particle size distribution of the starting material and the changes, induced to these parameters by the press process.
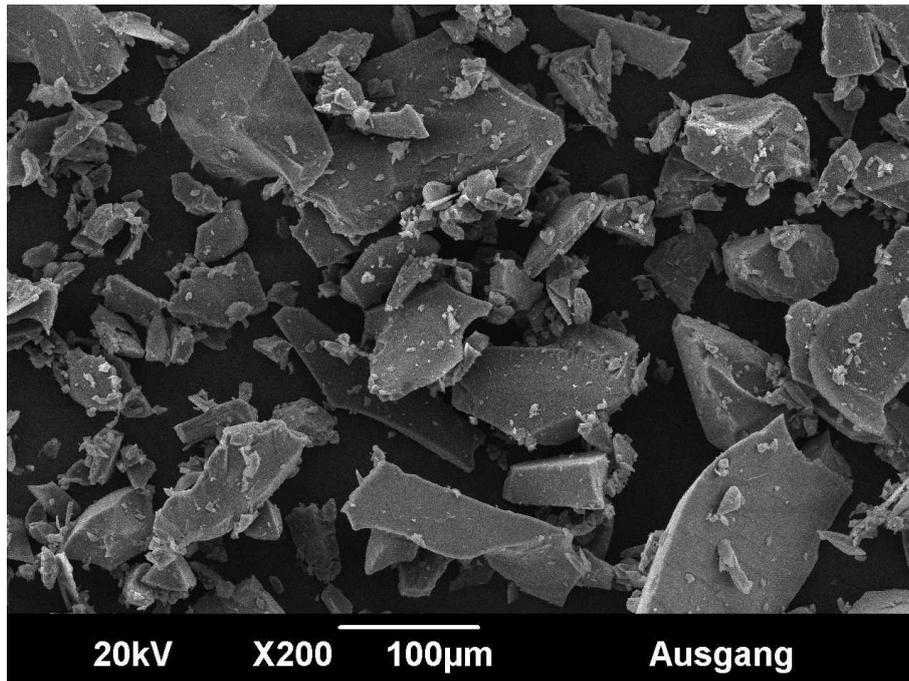
Figure 13: Scanning electron microscopic picture of untreated lithium tri-silicate powder.

In Fig. 13 the starting material before compaction is shown. The particles are sharp and irregular formed. They show a high variation in particle size and a variation in morphology as well. Some particles have a more elongated, thin form, while bigger particles show a more compact form with higher aspect ratio.

The products of *in situ* impedance spectroscopy compaction experiments were analyzed by SEM after compaction to determine changes in morphology and particle size. Possible changes may be break of particles, splintering or sintering. Fig. 14 shows the compaction products. By view only a slight change in morphology and particle size is visible.
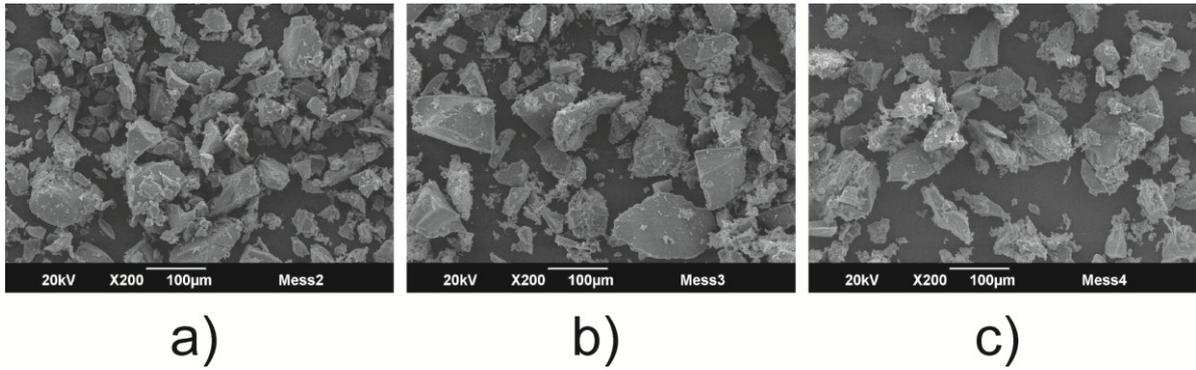
Figure 14: Representative SEM pictures taken after measurement Mess2 (a), Mess3 (b) and Mess4 (c).

To analyze changes during compaction, a SEM image based method is used to determine the particle size distribution. To determine a reproducible particle size distribution a 2-parameter ellipsoidal model is assumed to describe the form and size of each particle. For each particle two length values for the short and long dimension are measured with the help of the graphic software ImageJ [85]. To calculate the arithmetic mean of both values is one approach to get a value for the particle size. A more accurate approach is based on the volume determination of each particle by

$$V_{particle} = \frac{4}{3} \cdot \pi \cdot a \cdot b^2 \qquad (9)$$

with $V_{particle}$ as particle volume, a for the long dimension length and b for the short dimension length. To get a statistical relevant value three SEM pictures were made of each sample. For each picture about 100 particles were measured leading to about 300 particles measured per sample. Results on particle size evaluation are given in Appendix 5.H to 5.L.

2.3.2.2.1 Particle size distribution

The particle size analysis shows clear changes in size and distribution of particles by compaction of the lithium tri-silicate powder. In Fig. 15 the particle volume distribution of the starting material and the products of the compaction are shown.
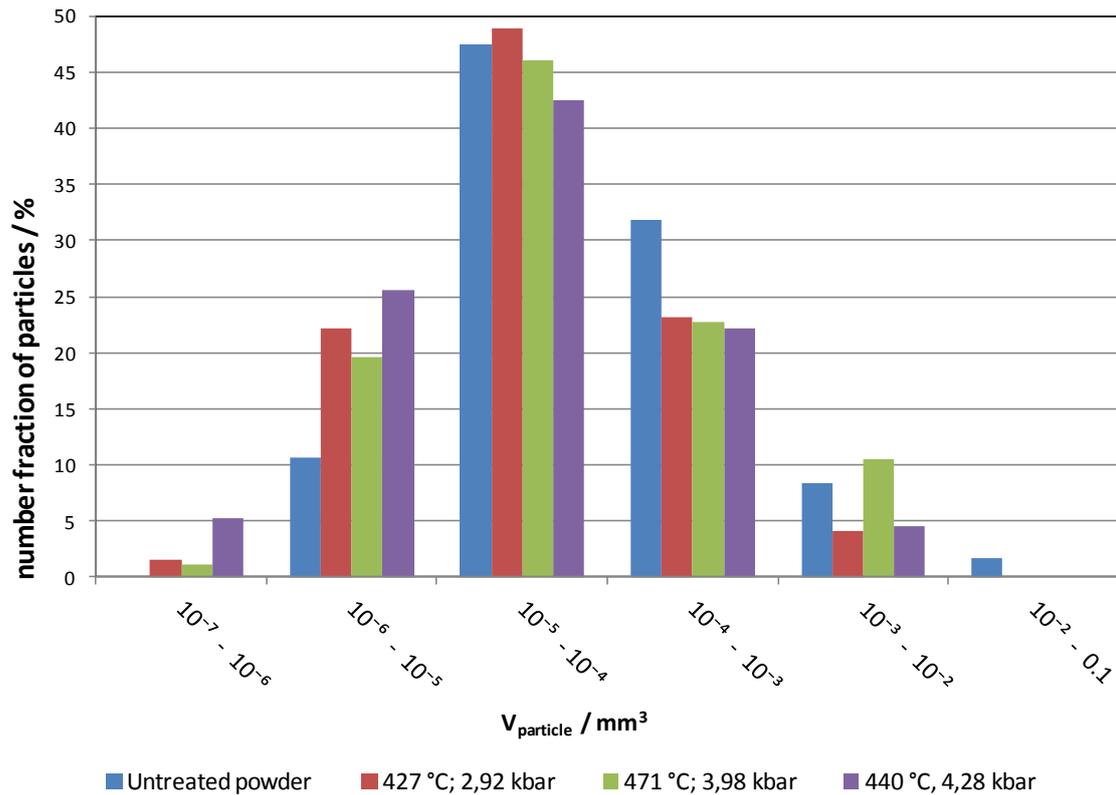
Figure 15: Particle distribution for $Li_2O * 3\ SiO_2$ powder as untreated powder (blue) and after axial compaction under different conditions. Both values, temperature and pressure, are maximum values during the impedance spectroscopy analysis corresponding to the products of experiment Mess2 (red), Mess3 (green) and Mess4 (violet). Every bar gives the procentual particle share for every sample within a certain volume range.

The initial particle size distribution of the starting material is centered at $1 \cdot 10^{-4}$ to $1 \cdot 10^{-5}$ mm^3 and shows a higher share of bigger particles than smaller particles. Due to the logarithmic x-axis the larger particles have a higher volume share.

The compaction products show only small differences among themselves, but a clear change to the starting material is evident. While the starting material distribution shows a

higher share of larger particles, the distributions of compacted powders is symmetrically centered at $1 \cdot 10^{-4}$ to $1 \cdot 10^{-5}$ mm^3. In general, by compaction the share of large particles decreases while the share of small particles increases. Surprisingly the sample treated with the highest pressure and temperature (cf. Fig. 15, Mess3 in green) follows this trend in a less pronounced way. It shows the highest share of particles in the volume fraction of $1 \cdot 10^{-3}$ to $1 \cdot 10^{-2}$ mm^3 and the lowest share of particles in volume fractions below $1 \cdot 10^{-5}$ mm^3. According to table 4 this is the only experiment carried out slightly above T_g of the sample material.

That indicates that the particles do not sinter at the given experimental condition because this would lead to an increase in particle size. While the particle size is changing, the morphology of particles stays nearly the same. To evaluate the particle morphology an anisotropic factor or ellipsoidal aspect ratio for each particle is calculated:

$$f_A = \frac{a}{b} \tag{10}$$

With short ellipsoid dimension a and long ellipsoid dimension b. Due to a high variation of the anisotropic factors, the mean value of all particles of an experiment is compared. The mean value of anisotropic factors of the starting material is 0.67 (means that in average the long particle dimension is 50 % higher than the short dimension). This mean value does not change much for the compacted powders (0.66 at 427 °C, 0.68 at 471 °C and 0.61 at 440 °C)

SEM-pictures and the particle size analysis indicate that the axial compaction of lithium tri-silicate powder leads to breakup of bigger particles to smaller particles with similar morphology and negligible sintering processes. At high pressures the particles tend to establish a smallest volume packaging and are only connected at small faces and edges

due to their irregular particle size distribution and morphology. The contact phases between grains are even under a higher effective force than applied because the contact areas are small in comparison to the particle surface. Mechanical degradation at these points decreases the packaging volume and produces small particles, while the particle size of larger particles is decreased, too. Mess3 shows less pronounced degradation behavior what might be explained by exceeding the glass transition temperature during the experiment. Due to larger structural flexibility the break of bigger particles is decreased and starting sintering processes consume the smallest particles.

2.3.3 Pressure depending impedance spectroscopy

Pressure dependent material characterization with impedance spectroscopy was done at all kind of materials like solid discs [86], [81], liquids [87] or powders [82]. The interpretation of impedance data depends not only on the analyzed material but on different boundary conditions, too. In the analyzed powders, the morphology of particles and the nature of particle contacts can affect the impedance data. Grain boundary effects and bulk conductivity should be the dominating conduction mechanisms in the spectra, while sample-electrode interaction may influence the quality of spectra. To determine if the current press and sample cell design allows concluding on those effects three experiments were done.

The impedance spectroscopy was carried out at constant temperature and varying pressures to analyze the sample material behavior during the pressurization process. In the following, the results of these three experimental runs will be described and afterwards discussed in comparison to available literature data for lithium tri-silicate glasses. The general experimental setup is described in chapter *2.3.1*. Changes to this and design adjustment to improve the performance are discussed with the following results.

Chapter 2: Axial pressure cell development

To exclude disturbing conductivity pathways in the apparatus an isolating sapphire glass disk was measured. From a sapphire bar (10 mm in diameter) a disk of 1.5 mm in thickness was sawed and a quarter cut of this was used for impedance spectroscopy measurements at different temperatures and pressures. Fig. 16 shows conductivity spectra of these measurements.
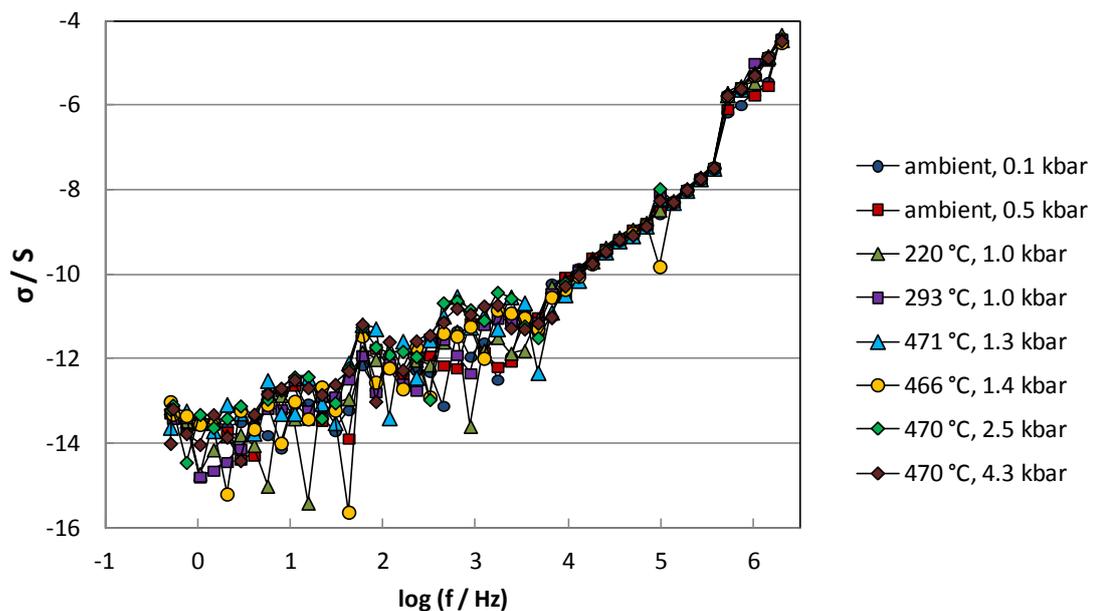
Figure 16: Impedance spectra of a sapphire disk. Absolute conductivity spectra are shown. The cell constant is 0.013 for all measurements. Noise in low frequency region is induced by lower resolution limit of impedance analyzer in combination with the sample cell.

In the spectra no temperature or pressure dependency arises and no distinct plateaus indicate any conducting pathways beside the isolating glass. One crucial point for impedance data interpretation is the conversion of absolute measurement data into material specific data. For this, the knowledge of the cell dimensions, electrode surface area and sample thickness, is necessary. For all pressurization runs the pressure depending sample thickness was measured by a micrometer caliper, while the electrode surface area was assumed to be constant and equals the piston surface area of the pressure cell. Results are given in table 5 and figure 17.

Table 5: Experimental settings of temperature and pressure of impedance spectroscopy experiments. Pressure dependent sample thickness is given as d_{sample}, following cell constant for IS calculation as K.

experiment	T / °C	f / kN	p / kbar	d_{sample} / mm	K / m
Mess2	420	1.60	0.318	0.80	0.063
	420	1.45	0.288	0.80	0.063
	426	2.55	0.507	0.80	0.063
	426	4.27	0.849	0.80	0.063
	426	7.64	1.520	0.70	0.072
	426	9.47	1.884	0.68	0.074
	427	12.54	2.495	0.68	0.074
	422	14.70	2.924	0.68	0.074
Mess3	469	2.40	0.477	0.75	0.067
	470	5.70	1.134	0.71	0.071
	471	13.15	2.616	0.69	0.073
	470	16.00	3.183	0.66	0.076
	471	20.00	3.979	0.63	0.080
Mess4	440	1.14	0.227	0.75	0.067
	440	5.65	1.124	0.70	0.072
	440	10.80	2.149	0.68	0.074
	440	15.60	3.104	0.68	0.074
	439	18.40	3.661	0.67	0.075
	440	21.50	4.277	0.67	0.075
	440	14.90	2.964	0.69	0.073
	434	7.40	1.472	0.70	0.072
	433	0.97	0.193	0.74	0.068

The cell constant equals the electrode area divided by sample thickness. An assumed error in thickness of 0.02 mm and an error of 0.0025 mm^2 in electrode area lead to an estimated error of 0.0002 m or 0.3 % for a cell constant value of 0.06 m.
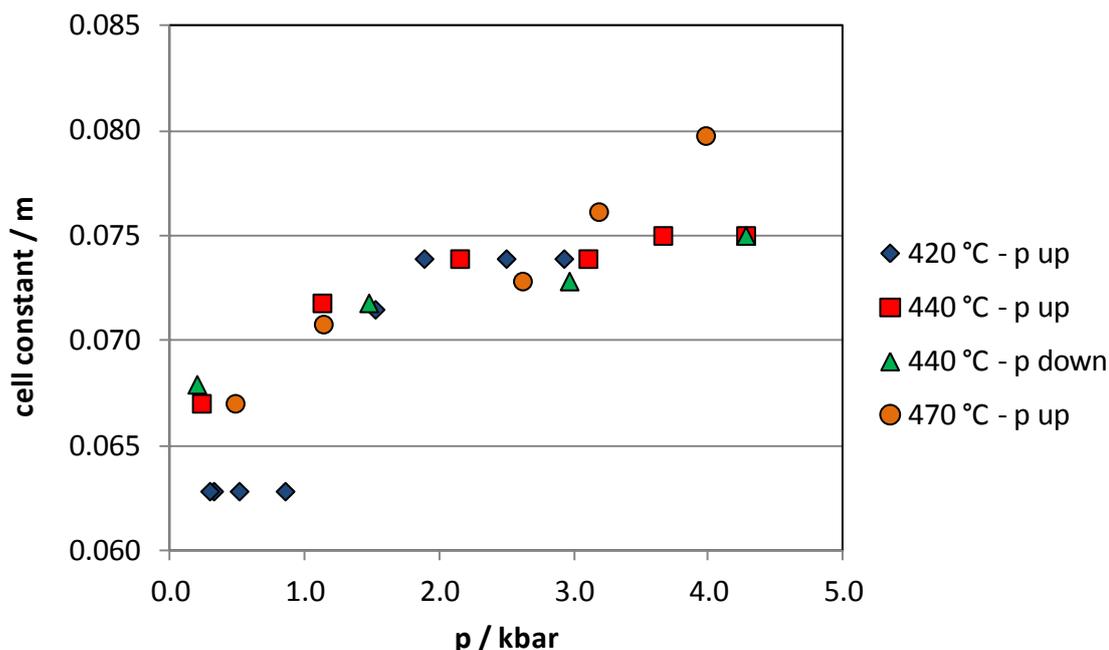
Figure 17: Pressure dependency of cell constants in axial pressure impedance spectroscopy experiments.

Fig. 17 shows an increase of the cell constant values which are expected for decreasing sample thickness with higher pressure. The values vary between 0.063 and 0.080 m. Only for the pressure cycle at 440 °C an up and down cycle was obtained due to a bad spectrum quality at the pressure down cycle for other temperatures. For 440 °C, the cell constants coincide for increasing and decreasing pressure, indicating that the pressurization process is reversible. The shown cell constant values are used for the calculation of the specific conductivity values from measured impedance spectra.

2.3.3.1 Pressure cycle at 420 °C

82 mg of lithium tri-silicate are compacted at 420 °C at pressures from 0.29 to 2.92 kbar. Only for increasing pressures impedance spectra of reasonable quality could be obtained. The recorded impedance data are corrected by cell constant values at distinct pressure to get the specific conductivity spectra. These spectra are shown in figure 18.
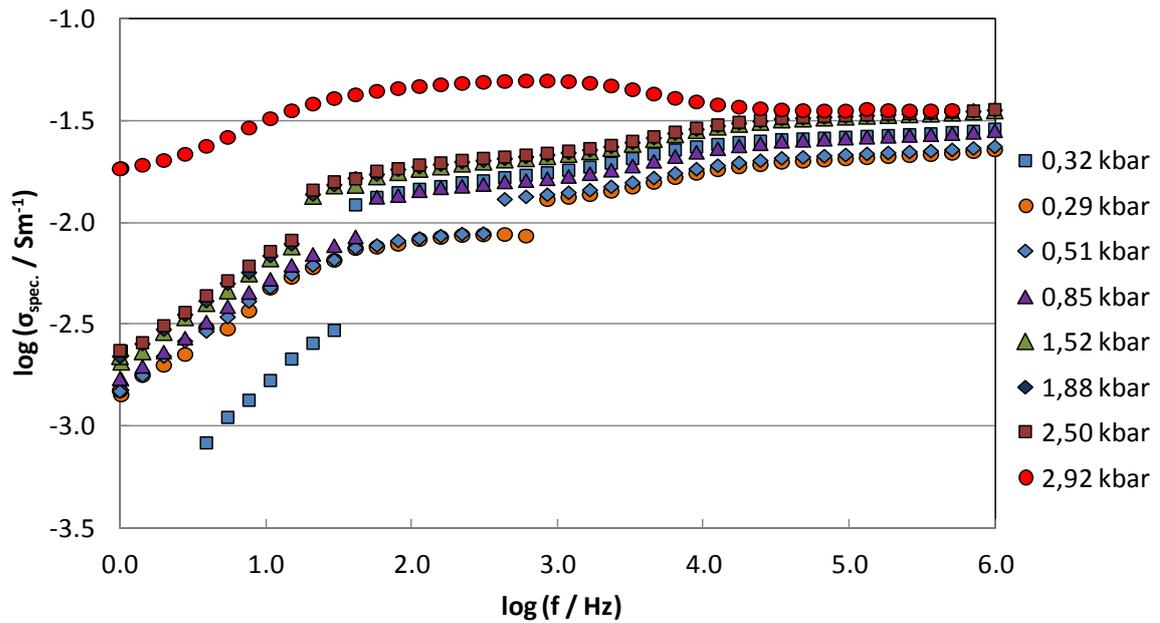
Figure 18: Pressure dependent specific conductivity spectra of $Li_2O \cdot 3\ SiO_2$ at 420 °C in the frequency range of 1 Hz to 1 MHz.

Jumps in specific conductivity in a frequency range from 10 Hz to 100 Hz are observable. From 0.29 to 0.51 kbar, the spectra show an indifferent behavior and a pressure dependence of the specific conductivity is not very likely. This might cause in changes of sample structure: The powder particles are a loose downpour before pressurization. The sample is pressed together and existing cavities are removed due to mechanical changes until the powder is dense enough to be stable against the applied pressure. At higher pressures the specific conductivity raises with increasing pressures. However, the overall spectra quality show good results and two distinct plateaus are clearly distinguishable. A low frequency plateau appears at lower conductivity and a high frequency plateau shows higher conductivity for all pressures beside 2.92 kbar. At this pressure, the spectrum shows a contrary behavior. After the record of this spectrum, no further spectra of sufficient quality could be obtained. This leads to the assumption that a change in the experimental setup is responsible for the not expected behavior. This assumption can be clarified by Cole-Cole-plot analysis. Fig. 19 shows the Cole-Cole-plot of the spectra given in figure 18.
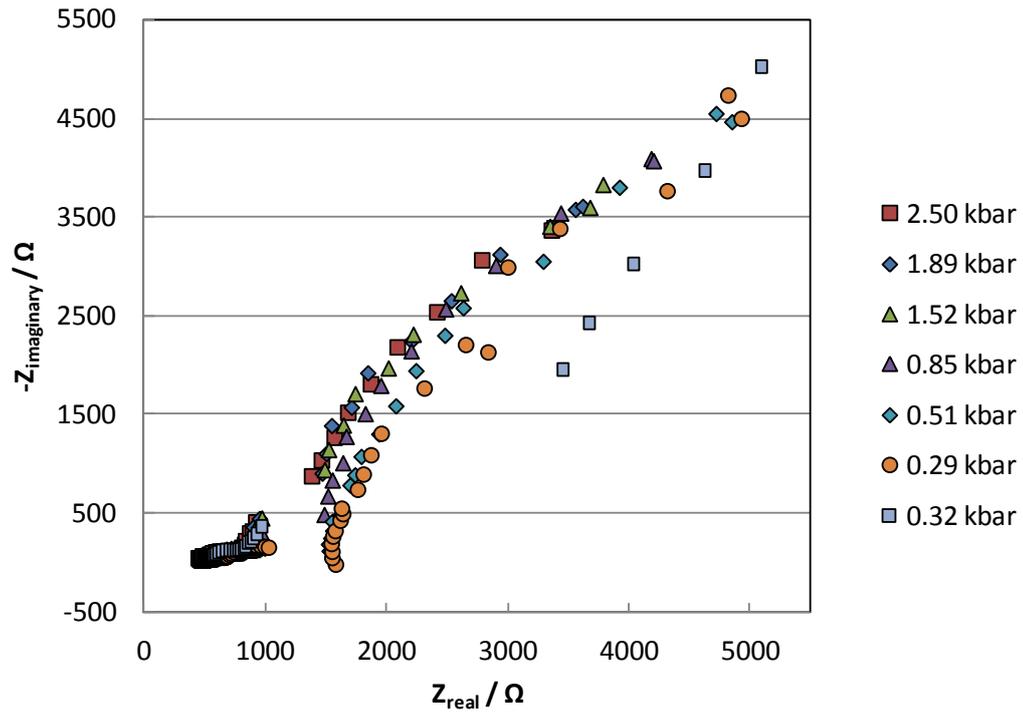
Figure 19: Cole-Cole-plot presentation of impedance spectra measured at 420 °C at increasing pressure.

The spectra show comparable behavior at low resistances, but the form of the curves is not clearly to resolve. With increasing real part of impedance an increase in the imaginary part of impedance occurs. All spectra show a gap which is corresponding to the jumps in the impedance spectra. This indicates that this problem is aroused by a jump in Z_{real} during the measurements. An enlarged presentation of the low resistance part is given in figure 20.
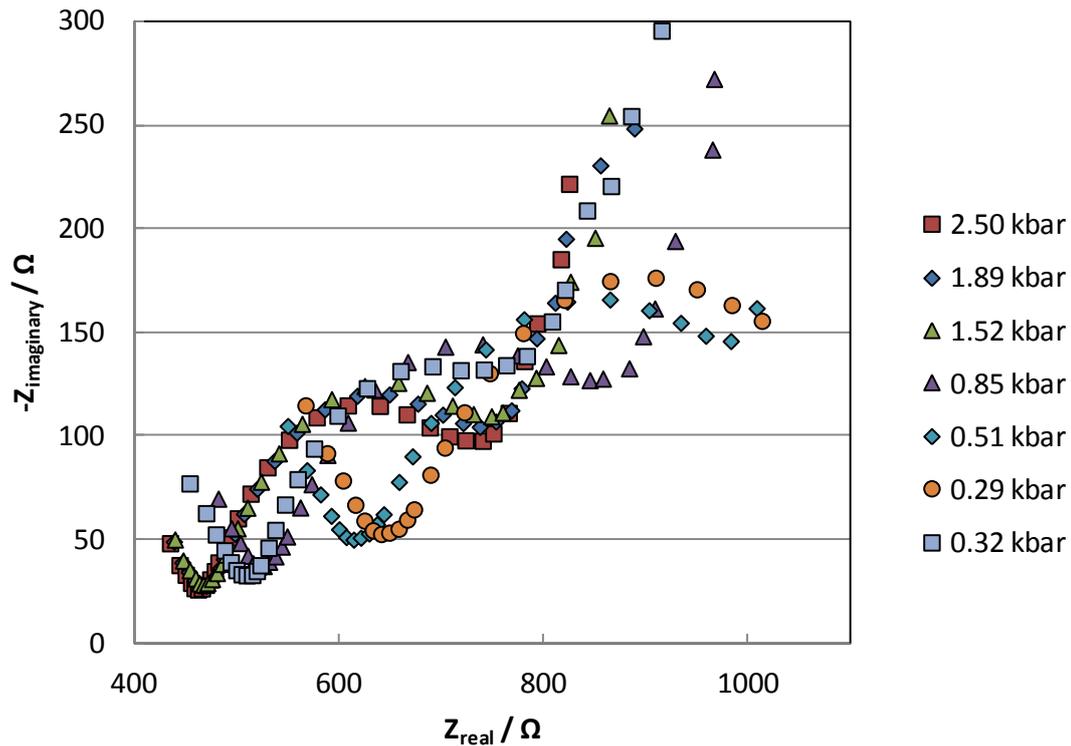
Figure 20: Enlarged presentation of Cole-Cole-plots at 420 °C from 400 to 1000 Ω Z_{real} at increasing pressure to show semicircle behavior more detailed.

All spectra show comparable characteristics: An end tail of a first semicircle at low z_{real} values, followed by a more pronounced semicircle and increasing behavior for high z_{real} values. The center of the dominant semicircle is shifting with increased pressure from high to lower Z_{real} values beside the 0.32 kbar measurement. This measurement showed worst quality and probably the experimental setting had not reached equilibrium during this measurement. Beside this measurement, the Z_{real} coordinate of the semicircle maximum shifts from 920 Ω at 0.29 kbar to 620 Ω at 2.50 kbar. The spectra at 1.52 kbar, 1.89 kbar and 2.50 kbar show comparable semicircle development while the incline of the following increasing part increases with increasing pressure. In the following figure 21, the Cole-Cole-plot of 2.50 and 2.92 kbar measurements are presented with an unexpected behavior in impedance spectra.
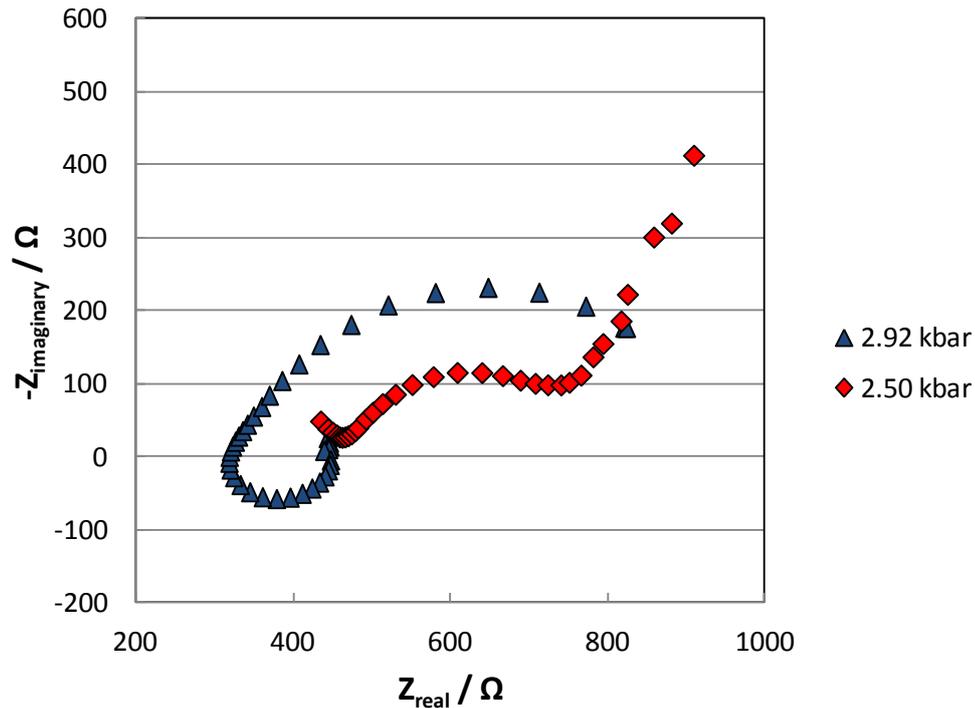
Figure 21: Cole-Cole-plot of high pressure measurements at 420 °C.

At 2.50 kbar the plot is typical for an ionic conductor: A denoted end of a first semicircle at low resistance, a full semicircle at medium resistances and an increasing behavior for large resistances. In the 2.92 kbar measurement a distinct negative semicircle arises at low resistances. This behavior indicates a change in sample contacting during the pressurization process and leads to the assumption of a decrease of sample contact quality. That assumption is supported by the fact that no spectrum of good quality could be obtained after this measurement. Due to this the measurement at 2.92 kbar is not taken in consideration at the further discussion. From the impedance spectra the direct current conductivity can be extracted at the inflection points of the DC plateaus of the spectra.
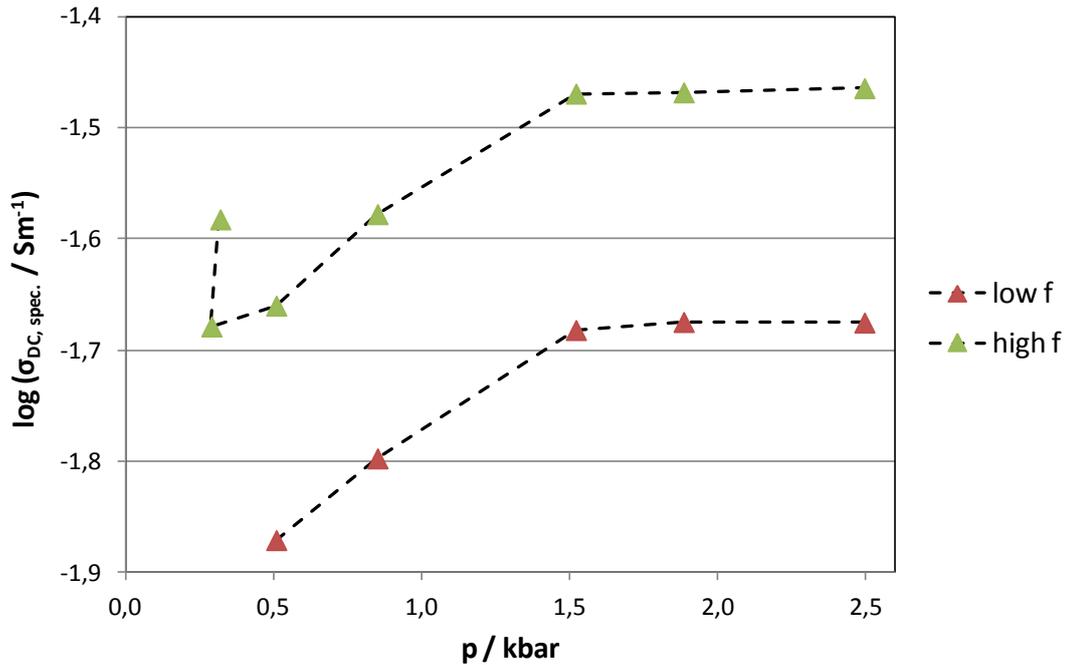
Figure 22: $\sigma_{DC, spec.}$ in dependency of pressure at 420 °C. The low frequency plateau values are marked as "low f" (red), the high frequency plateau values are marked with "high f" (green). Dashed lines are only for a better following and indicate no data fitting.

The values of the specific conductivity at the two observed plateaus can be interpreted as direct current values of two distinct conducting mechanisms in the material. Fig. 22 shows the pressure dependence of these values. With increasing pressure from 0.29 to 1.5 kbar the value increases and stabilizes at 1.5 kbar. This indicates a setting of the sample material in the first pressure steps until all remaining air is carried out and the powder particle are in full contact. To analyze the pressure dependence of the lithium tri-silicate material itself, the focus should be set on a pressure range above 1.5 kbar for the tests. To improve the quality of spectra the following test at 470 °C was run with two gold foils attached to the sample.

2.3.3.2 Pressure cycle at 470 °C

82 mg of $Li_2O \cdot 3 SiO_2$ were placed on a gold foil on the sample cell. Afterwards a second gold foil was attached on top of the powder. A problem was to fit this foil horizontally on top of the powder because it tends to sink into the loose powder. A slight pre compaction of the powder by hand enhanced the stability of the stack up, but did not solve the problem completely. A slight influence of a not perfect fitting upper electrode cannot be excluded. The stack up was heated up to 470 °C at constant pressure of around 0.5 kbar. Then the pressure was raised stepwise from 0.48 kbar to 3.98 kbar. At each pressure step an impedance spectrum was recorded.
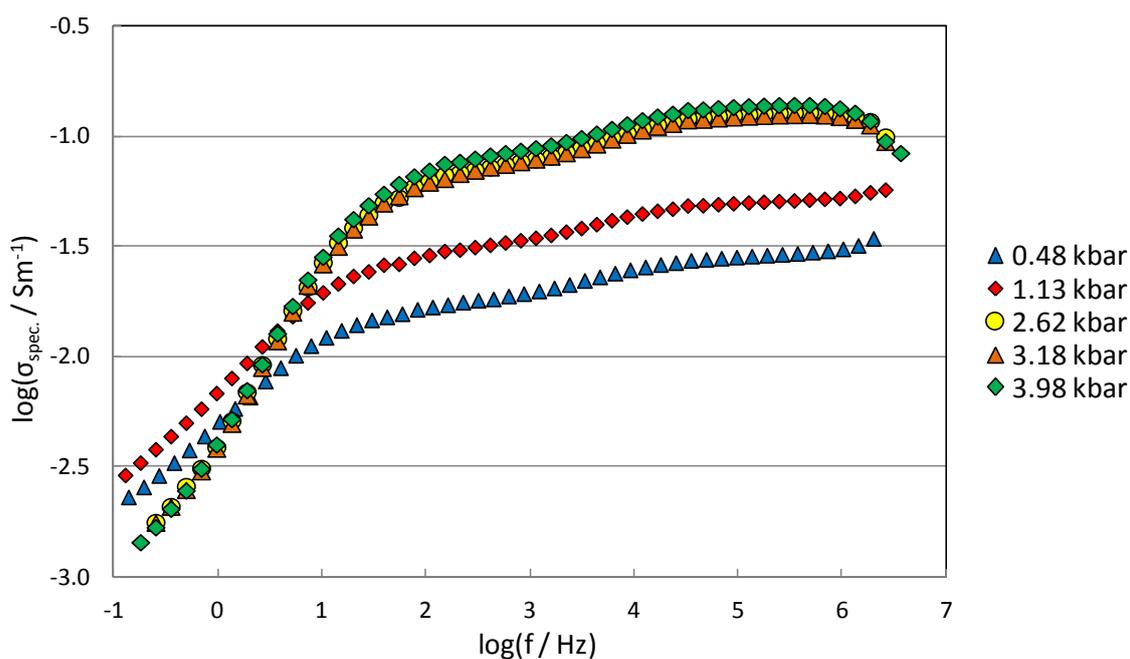
Figure 23: Pressure dependent specific conductivity spectra of $Li_2O \cdot 3 SiO_2$ at 470 °C in the frequency range of 0.1 Hz to 1 MHz.

Fig. 23 presents the obtained spectra. The quality of the impedance spectra is clearly better than for the spectra recorded at 420 °C, what is attributed to the inserted gold electrodes. The spectra show increasing conductivity values for increasing pressure. At low pressure values (0.48 kbar to 2.62 kbar) this behavior is more pronounced than in the pressure range

above 2.62 kbar. There is only a slight increase in conductivity from 2.62 kbar to 3.98 kbar. In the low frequency range the behavior of conductivity change is contrary to the high pressure behavior: While the conductivity raises from 0.48 to 1.13 kbar, it decreases when the pressure is raised above 2.62 kbar and stays nearly unaffected by higher pressures. It seems that the sample material behavior changes drastically at a pressure between 1.13 kbar and 2.62 kbar. One possible explanation for this behavior could be the finished compaction of the material in this pressure range and the outgoing of remaining air in the sample cell.

For all spectra two distinct plateaus are observable. From the plateau values of specific conductivity, the direct current specific conductivity of two assumed conducting mechanism can be taken.
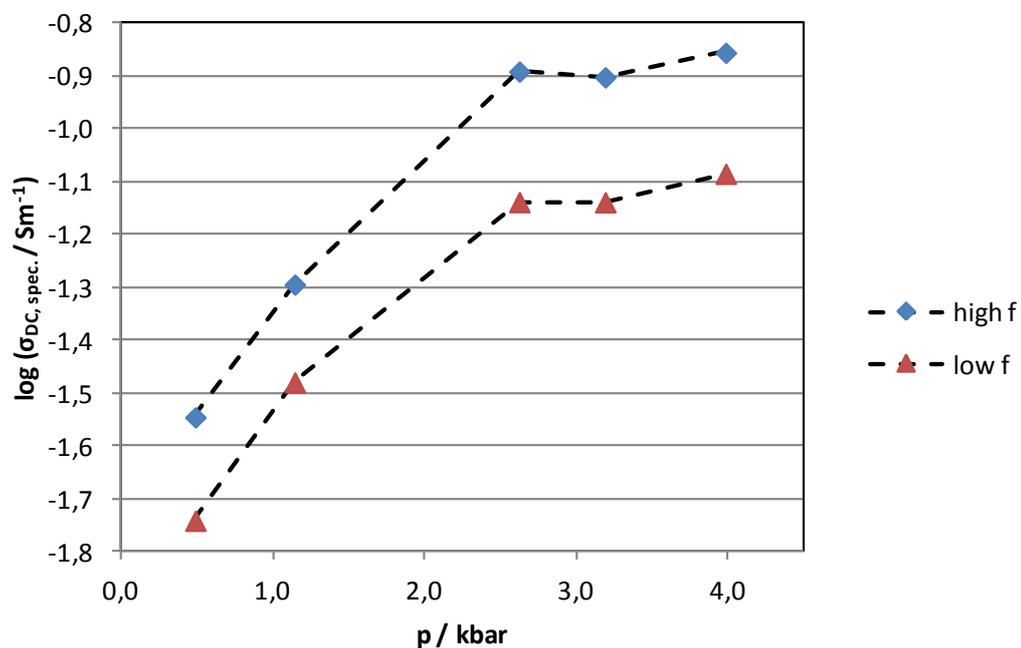
Figure 24: $\sigma_{DC, spec.}$ in dependency of pressure at 470 °C. The low frequency plateau values are marked as "low f" (red), the high frequency plateau values are marked with "high f" (blue). Dashed lines are only for a better following and indicate no data fitting.

Fig. 24 shows the increase in conductivity for increasing pressure. While the increase at low temperatures is high (around 0.4 log units in specific conductivity per kbar pressure) the pressure changes above 2.5 kbar are lower (around 0.36 log units in conductivity per kbar pressure). This difference might fall into the estimated experimental variation.

To connect both experimental runs, a temperature in between 420 and 470 °C was chosen for the next experimental run.

2.3.3.3 Pressure cycle at 440 °C

For this pressure cycle experiment 82 mg of $Li_2O \cdot 3\ SiO_2$ were placed in the sample cell with two gold foils on bottom and on top of the sample material. A slight pre-compaction of the sample material by hand allowed a more accurate positioning of the top gold foil on the sample material. In this case, it was possible to run a full pressure cycle from 0.23 kbar up to 4.28 kbar and back to 0.19 kbar without losing impedance spectra quality, what allows to evaluate the reproducibility of the pressure cycle experiments within this axial pressure and sample cell design. The recorded impedance data was recalculated to specific conductivity values with help of the measured cell constants.

For increasing pressure an increase in conductivity is shown in figure 25. The spectra quality at 0.23 kbar is worse than at higher pressure due to missing set up of the sample stack up and remaining air. With increasing pressure conductivity raises along the whole measured frequency range compared to the 470 °C measurement. One cause for this behavior might be a more accurate measurement due to a better fitting gold foil electrode or a change of the expected inflection point to a lower frequency due to the lower measurement temperature. The coinciding trend of all spectra indicates, that there is no distinct intersection point at lower frequencies, so a better spectra quality is the more probable explanation for this behavior.
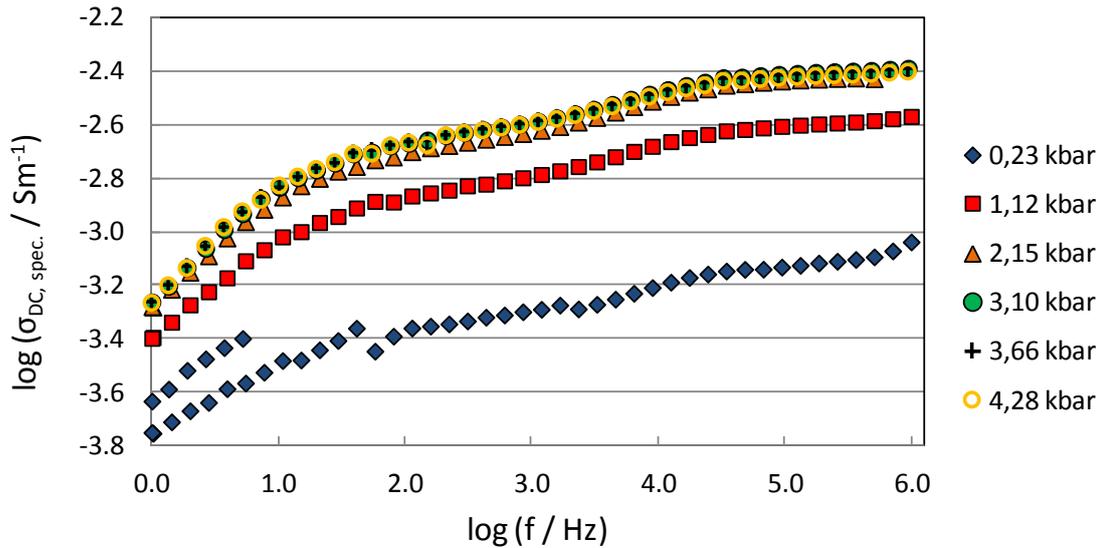
Figure 25: Pressure dependent specific conductivity spectra of $Li_2O \cdot 3 SiO_2$ at 440 °C in the frequency range of 1 Hz to 1 MHz for increasing pressure.

Fig. 26 shows the decreasing pressure cycle at 440 °C. Specific conductivity stays nearly unaffected by pressure down to 1.47 kbar. The drop in conductivity from 1.47 kbar to 0.19 kbar can be explained by a relaxation of sample material.
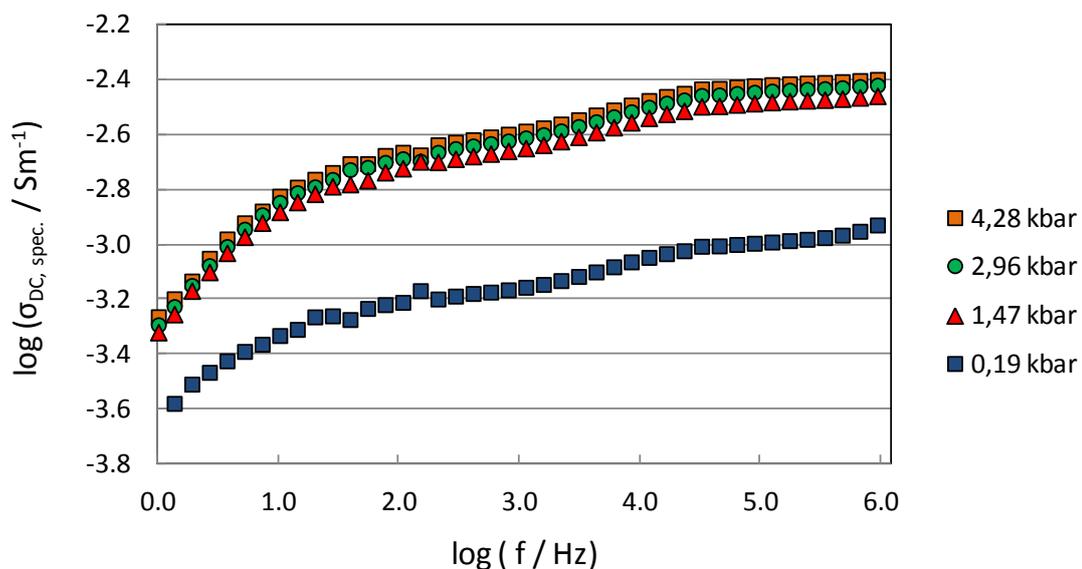
Figure 26: Pressure dependent specific conductivity spectra of $Li_2O \cdot 3 SiO_2$ at 440 °C in the frequency range of 1 Hz to 1 MHz for decreasing pressure.

Compared to the 0.23 kbar measurement from the increasing pressure cycle the specific conductivity value after pressure release is higher. A denser sample material and slight particle interconnection by compaction may explain this. For both, the increasing and the decreasing pressure cycle, two distinct plateau values are observable in all spectra. The specific conductivity values at these plateaus can be interpreted as σ_{DC} values for two distinct conduction mechanisms.
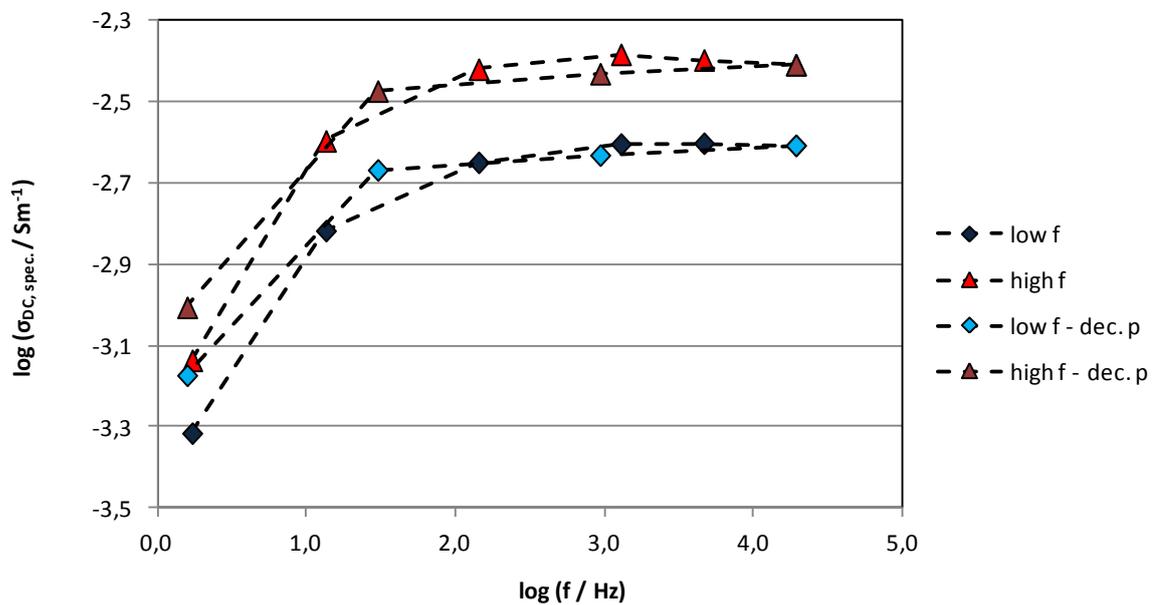
Figure 27: $\sigma_{DC, \text{spec.}}$ in dependency of pressure at 440 °C. The low frequency plateau values are marked as "low f" (dark blue) for increasing pressure and "low f - dec. p" (light blue) for decreasing pressure. The high frequency plateau values are marked with "high f" (red) for increasing pressure and "high f - dec. p" (dark red) for decreasing pressure. Dashed lines are only for a better following and indicate no data fitting.

Fig. 27 shows the dependence of $\sigma_{DC, \text{spec.}}$ values on pressure for high and low frequency plateaus. Both curves show a saturation behavior with increasing pressure like the measurements at 420 °C and 470 °C. The material behavior changes between 1.5 and 2 kbar and further pressurization only slightly affects the specific conductivity.

The increasing and decreasing pressure cycles are in a very good agreement within 0.05 log units at pressures above 1.5 kbar and 0.15 log units at pressures below 1.5 kbar, what supports the measurement reversibility of the current press design. These values are also an indication for error estimations of experiments done with this design.

2.3.3.4 Comparison of pressure depending IS experiments

To get more information about the mechanisms taking place in the sample, two aspects will be analyzed in more detail. Firstly, if the difference between high and low frequency plateau values changes with pressure and secondly, if the temperature dependence of both plateau values can reveal information about the present conducting mechanism with the help of comparison to literature data of the bulk lithium tri-silicate material, available in Bauer et al. [24].

Subtracting the high frequency plateau value of $\sigma_{DC,\ spec.}$ from the low frequency plateau value the difference in pressure dependency of both mechanisms is available. Fig. 28 shows the difference of both plateau values for each spectrum. At 420 °C no clear dependence is observable. At 470 °C an increase in difference between 1 and 2.5 kbar dominates the curve. At 440 °C the increasing pressure cycle and the decreasing pressure cycle follow a hysteresis curve.
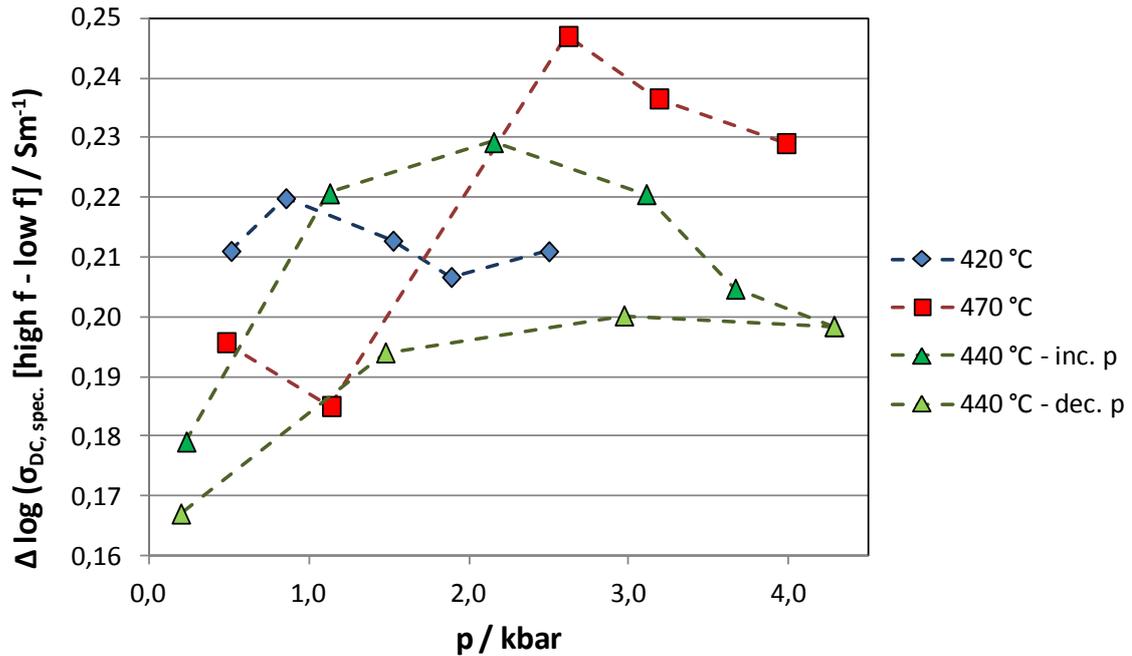
Figure 28: The difference between the high frequency and low frequency plateau value of $\sigma_{DC, spec.}$ plateau values for each impedance spectrum is shown in dependency of applied pressure. For the measurement at 440 °C both pressure cycles, increasing and decreasing pressure, are shown. Dashed lines are only for a better following and indicate no data fitting.

With the assumption that pressure dependency is composed of two effects, closing of cavities by moving particles on the one hand and direct pressure induced bulk material changes on the other hand, the high pressure range above 1.5 to 2 kbar becomes more interesting. Below these pressures the measurement is influenced by cavities in the sample set up and following a not fully established particle contact. In this pressure range Fig. 28 shows a decrease of plateau value differences for the measurements at 470 °C and 440 °C and less pronounced at 420 °C. This decrease leads to the conclusion that the two conductivity mechanisms might have different pressure dependencies. The overall changes with pressure are only slightly pronounced. Additional measurements at samples with varying particle size distributions would be necessary to validate this result. If one mechanism is more affected by pressure changes than the other, the changes in conductivity will lead to a change in difference of specific conductivity at the impedance spectra plateaus. The influence on each plateau could be observed by changing the particle

size distribution and overall surface areas of the sample. The hysteresis behavior at 440 °C can be interpreted as an irreversible effect induced by pressurization. The sample is changed irreversibly during pressurization. Afterwards the Δ values stay significantly lower with lowered pressure. As described in *3.2.2.1* this irreversible change might be explained in the breakdown of particles and the resulting change in particle size distribution.

To analyze the temperature depending behavior of the material, the impedance spectroscopy data for the low and high frequency plateaus are compared in terms of an Arrhenius analysis.
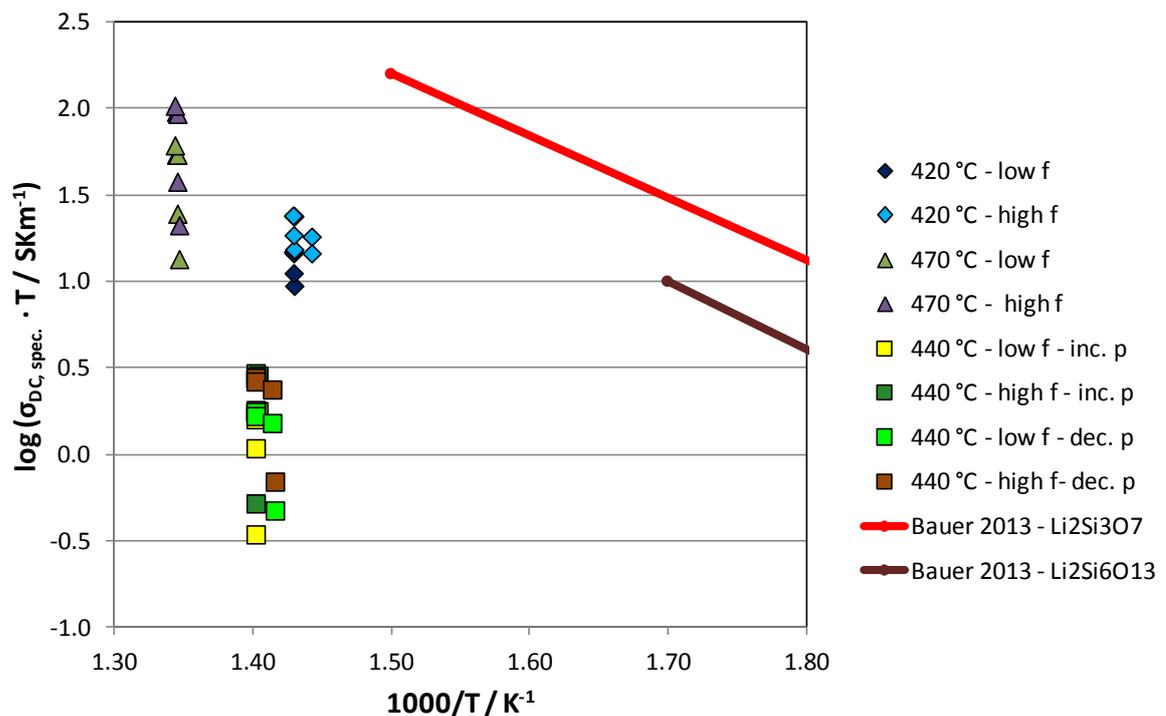
Figure 29: Arrhenius plot of low frequency and high frequency plateaus of pressure depending experiments. As comparison, literature values from Bauer et al. (2013) [24] for lithium tri-silicate and lithium hexa-silicate glasses are shown in red.

The Arrhenius plot (cf. Fig. 29) shows a large variation for the pressure depending experiments. The pressure influence exceeds the temperature influence. But even both plateau values are not clearly distinguishable. Especially the 440 °C data falls off the trend and shows around 1 log unit lower conductivities. Those results are more expected for the 470 °C measurement because it is the only one which was carried out above T_g of lithium tri-silicate glass of 460 °C.

Nevertheless, as shown before the high frequency plateau values show overall higher conductivities and should represent the more conductive mechanism. For the powder with comparable large grain sizes of around 30 μm in diameter (cf. *3.2.2*) a conducting mechanism by bulk material might be assumed. In Fig. 29 the bulk phase of $Li_2Si_3O_7$ shows a higher conductivity than the powdered material. This leads to the conclusion that the high frequency plateau represents the bulk material due to its higher conductivity. Due to the large particles this conducting mechanism should lead to the same IS conductivities as measured in the glasses, but a conductivity around 1 log unit lower than estimated is measured. This might be explained for the 470 °C measurement with two experimental problems which occurred there: The temperature excel the glass transition temperature leading to changes in microscopic sample structure and macroscopic flowing behavior into the crushable alumina ring. This also explains why this sample is the only one containing Al_2O_3 contaminations after compaction.

In general the low measured conductivities in comparison to the bulk glasses might also be explained by the large sample volume. As larger the sample thickness vs. mean particle size is, as more particle-particle contacts exist. These particle contacts act as barriers for the ionic diffusivity, even if a certain ion does not move from one to another particle. The accumulation of charge builds up a space-charge region at the contact areas, hindering the diffusion within the particle.

On the other hand, these particle surfaces can be unique structured zones in which other conducting mechanisms might be introduced, as shown for spodumene glasses by Kuhn [Kuhn 2009] by ball milling and re-sintering of spodumene glass. This sintering process might happen during the compaction in the axial pressure cell leading to new conducting zones at the particle surface. The low frequency plateau might represent this conductivity mechanism. The conductivity is lower there due to the low connectivity of these zones which explains the lower conductivity values measured within the low frequency plateau. Another support for this interpretation is the constant factor between high- and low-frequency plateaus. Fig. 22, Fig. 24 and Fig. 27 show a constant factor of 1.14 at 420 °C, 1.08 at 440 °C and 1.21 at 470 °C between the high frequency and the low frequency plateau. This constant factor should depend strongly on particle size distribution because this determines the share of particle contacts surface. The constant factor in all experiments indicates a constant share of particle surface conducting zones.

Although more experiments would be needed to clarify these mechanisms, conclusions about the pressure cell design can be drawn. Especially further experiments with varied particle size distributions or with different humidity and atmospheric conditions in general could help to distinguish between surface and bulk effects in the powdery sample materials.

2.3.4 Evaluation and proof of concept

The experiments show that the current press and sample cell design allow to measure pressure depending material characteristics. Impedance spectra of good quality can be recorded at elevated temperatures if noble metal surface protection methods are used at the pistons. The accessible pressure and temperature range is suitable for meaningful experiments at amorphous solids and glasses. If other analytical methods like SEM and XRD are used both, a comprehensive view on material changes and behavior during pressurization can be made and a connection between these material changes and their electrochemical and diffusive characteristics is accessible.

Chapter 3: Amorphous lithium ion conductors from CVS synthesis

3.1. Introduction

The combination of amorphous solid state and micro- or nanocrystalline structures might be a suitable combination to obtain fast solid ion conductors. To compare both influences, crystallinity and microstructure, another synthesis route is described in the following. Amorphous ion conductors like glassy alkali silicates and alkali alumosilicates are available by classic melt-quench process. Chapter 1 deals with those lithium alumosilicate glasses as fast lithium ion conductors. Amorphous oxide phases might be prepared by other synthesis routes than melt quench processes like sol-gel preparation [88] or chemical vapor deposition [16]. In this chapter the preparation of amorphous lithium alumosilicates by chemical vapor synthesis will be described. The mobility of lithium ions in the as synthesized powders is analyzed by solid state ^{7}Li solid state NMR spectroscopy. Afterwards, the obtained powders are post-processed by compaction in external heated cold seal pressure vessels (CSPVs) to obtain macroscopic solid disks as fast ion conducting materials. Crystallization and morphology changing processes induced by the compaction are analyzed. The conductivity characteristics of the obtained discs are measured by impedance spectroscopy analysis. The comparison between the alumosilicate glasses, the investigated compaction processes and the products by chemical vapor transport reveal the influence of synthesis route and post-processing on conductivity behavior of a variety of amorphous lithium silicates and lithium alumosilicates.

3.2. Chemical vapor synthesis (CVS)

The chemical vapor synthesis is a variation of the chemical vapor deposition (CVD). CVD processes are mostly used for the preparation of thin films on substrate materials [89], [90] for example to apply functional coatings [91]. Contrary to this, CVS is used here to obtain powdery bulk material [92]. The CVS allows producing a wide range of compositions which are not accessible with classical melt quench techniques.

3.2.1 CVS process

The comprehensive theoretical background of the processes taking place in chemical vapor synthesis may be found at Wilke [93]. A review on crystal growth chemistry and technical applications of single crystal synthesis is given by Hulliger [94]. In the following, a summary of the crucial process steps taking place during the formation of oxidic materials emblazes the chemical background of the conducted experiments.

The crystal growth process in vapor phase starts with the formation of crystal nuclei at atomic scale. The system needs to be in a supersaturated state for the given temperature in which the precursors react to form initial crystal seed (homogeneous crystal formation) or deposit new material on already existing seeds on a substrate (heterogeneous formation). Heterogeneous nucleation is typically seen at CVD processes while CVS routes need homogenous crystal seed nucleation and crystal growth in the vapor phase.

The nucleation rate of the initial reaction depends on the degree of supersaturation of the system. A high degree leads to a high number of new crystals seeds, while a lower degree of supersaturation prefers the growth of already formed particles by adding more precursor molecules. Due to this, a constant vapor phase composition is a crucial factor to produce particles with homogenous composition and phase. The nucleation rate also depends on

temperature [93] and a certain temperature is needed to overcome kinetic barriers in the system. By choosing a certain temperature the ratio of nucleation and crystal growth can be adjusted. The reaction stops when the precursor concentration gets too low and the system is not further in a supersaturated condition or the temperature conditions do not further support the equilibration of the system.

Due to high reactive gaseous precursors not only thermodynamic phases might be produced. Thermodynamic meta-stable products are formed under certain condition, if the degree of supersaturation and temperature allows the nucleation and growth of those phases without supporting the reaction to the thermodynamic stable phase due to higher kinetic barriers.

3.2.2 Lithium alumosilicate powder synthesis

Synthesis was done in a corporate project with the institute of Inorganic Chemistry, University of Hanover within the framework of the Molife Project (FOR1277). All CVS synthesis and pre-compaction material characterizations (with exception of the halogenide analysis by Volhard-titration) were done by Isabella Laskowski, PhD Student at the Institute of Inorganic Chemistry, University Hanover. It is necessary to present the synthesis and analytical data here (chapter *3.2.2* ff.) because it is a required background to interpret the following compaction experiments (chapter *3.3* ff.). The figures concerning synthesis and corresponding analytical work are mainly designed by Isabella Laskowski and are used with her consent. They are marked in brackets.

For chemical vapor synthesis, aluminium-, silicon- and lithium bromides are used as a starting material. As shown in Fig. 30, aluminium bromide is provided in a tube oven (1). It operates at a constant temperature of 448 K to provide a sufficient partial pressure of $AlBr_3$ in the gas phase. Gaseous $AlBr_3$ is transported to the reaction zone with an argon

flow rate between 1 and 5 L/h but syntheses were done typically with a flow rate of 3 L/h. Silicon bromide is vaporized by bubbling argon through the liquid. To increase the partial pressure it is heated by a thermostat (2) at a constant temperature of 338 K. The $SiBr_4$ is transported to the reaction zone by an argon stream with a flow rate of 5 to 8 L/h. All flow rates are controlled by variable area flow-meter. The third halide precursor lithium bromide is provided in a quartz crucible (3) in the reaction zone which is constantly heated to a temperature of 1473 K. The LiBr evaporates at the given temperature in the reaction zone (upper part of reaction tube, marked in orange). All three precursors are mixed with oxygen in the reaction zone. Oxygen is provided by direct gas stream of 10 L/h O_2 to the reaction zone.

All four components react at 1473 K in the reaction zone, where spontaneous nucleation of solid particles takes place. The chemical process may be described with following idealized reaction:

$$x\ LiBr_{(g)} + y\ AlBr_{3\,(g)} + z\ SiBr_{4\,(g)} + \left(\frac{x}{4} + \frac{3y}{4} + z\right) O_{2\,(g)} \Rightarrow Li_x Al_y Si_z O_{\frac{x}{2}+\frac{3y}{2}+2z\,(s)} + \left(\frac{x}{2} + \frac{3y}{2} + 2z\right) Br_{2\,(g)}$$
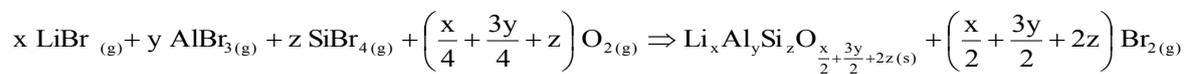
Those particles and remaining precursors are transported through the reaction zone by the combined argon and oxygen streams to the temper zone with a lower temperature of 1373 K. Here the nucleated particles grow and consume the remaining precursor molecules to form bigger particles.

The resulting powdery product is collected in a glass bulb (5). Afterwards the gas stream runs through a washing flask, containing sodium thiosulfate solution for disposal of non-reacted precursors.
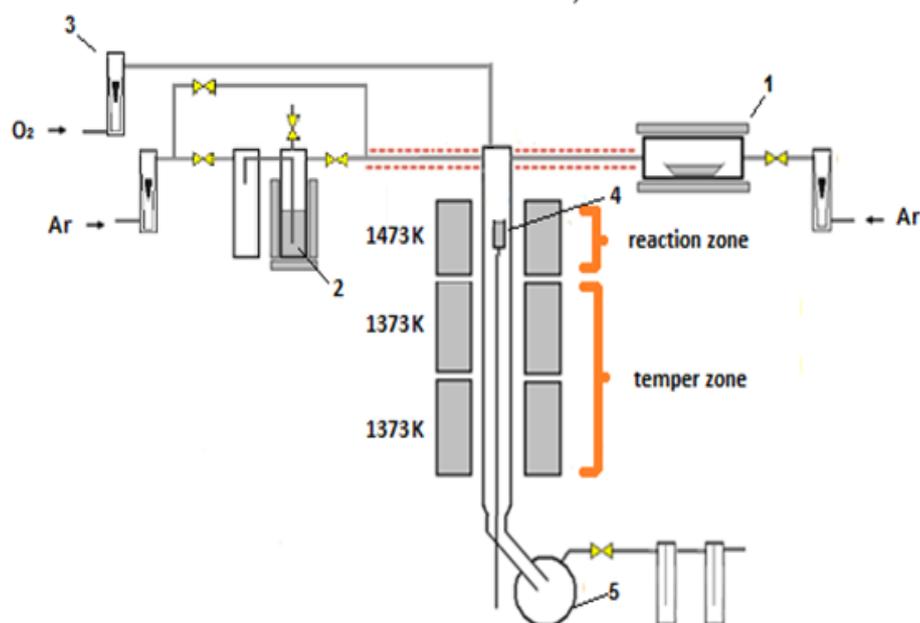
Figure 30: CVS apparatus used by Isabella Laskowski to synthesize lithium aluminosilicates of different composition. (Picture according to Brünig [95], adjusted by and used with the consent of Isabella Laskowski).

Three alternatives of the standard synthesis route were carried out: 1) The oxygen stream was increased to achieve a higher reaction rate in the reaction zone. The samples are marked with "iO" in the sample name. 2) The normally dry oxygen stream from the gas tank was humidified with water by bubbling through a water flask before it enters the reaction zone to a rel. humidity of 100 %. The samples are marked with "W" in the sample name. 3) To achieve a better mixing of bromide precursors before the mixture enters the reaction zone, the oxygen stream was introduced below the lithium halogenide container. For this the end of the oxygen inlet tube was placed approximately 15 mm below the bottom of the quartz crucible. In all variation the synthesize products collected in the collection bulb (5) were white powders. The products were taken out of the bulb and placed in a glove box for further use.

3.2.3. CVS sample characterization

The obtained samples were characterized by XRD for structure determination and SEM for morphology. The composition was determined mainly by EDX analysis. First compaction

and dielectric experiments showed an influence of humidity on the impedance spectroscopy measurements. To clarify if the samples still contain hygroscopic bromide compounds the powders were also analyzed by Volhard-titration analysis to quantify remaining bromide contaminations.

3.2.3.1 Structure and morphology

The XRD analysis of the obtained powders show that the described synthesis route lead to amorphous powders with a small share of crystalline phases as shown in Fig. 31. In most cases these crystalline contents are not clearly to define by comparison with known XRD patterns. For clarification Fig. 31 shows examples where a clear definition of a crystalline phase was possible. Fig. 31a) shows sample ALS-47 as amorphous powder with a share of crystalline $LiAl_5SiO_8$. Fig. 31b) shows sample ASL-81W with a small share of crystalline Li_2SiO_3. Both, lithium alumosilicate and lithium silicate phases occur in the synthesized samples in low share which is not exactly quantifiable with the used XRD techniques.

The XRD pattern given in figure 31c) is the result of a measurement done in absence of air and water in a Mark tube (fused quartz capillary). The major share of this sample is LiOBr, a hygroscopic salt which decompensates in the presence of water. This chemical compound is a hint on remaining halogenide components in the obtained products.
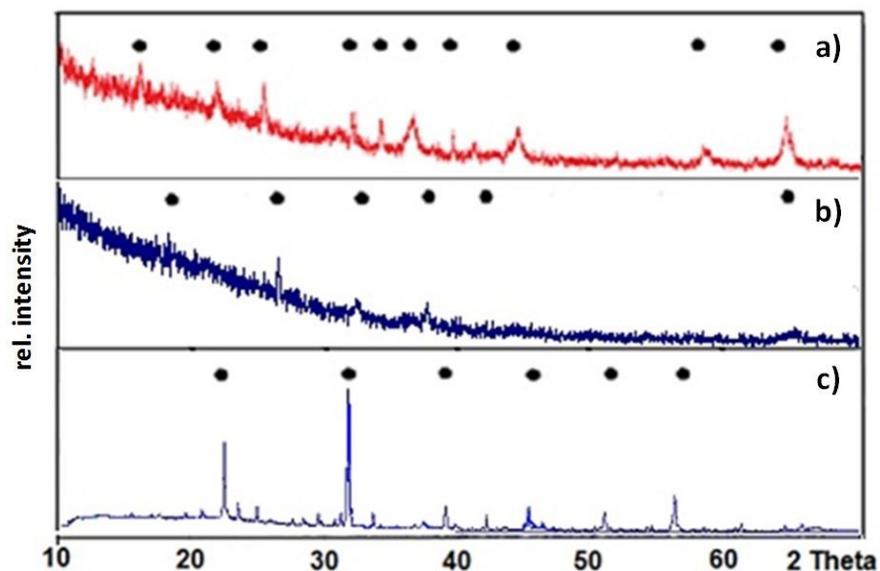
Figure 31: XRD patterns of selected powder compositions: a) Aluminium rich sample ALS-47 with an Al/Si (mass%) ratio of 4.48 (calculated from EDX measurement, cf. table 6). Points indicate the XRD-reflex positions of crystalline LiAl5O8. b) Silicon rich sample ALS-81W with an Al/Si (mass%) ratio of 2.31 (calculated from EDX measurement, cf. table 6) shows a low content of crystalline Li2SiO3 (indicated with points). c) Sample ALS-72 with an Al/Si ratio (mass%) of 2.20 (EDX, cf. table 6) show a high share of crystalline LiOBr (indicated with points). This sample was analyzed in the absence of air in mark tubes. (Picture used with the consent of Isabella Laskowski)

In summary, the XRD results show that on one hand amorphous lithium alumosilicate powders might be obtained by this technique, on the other hand these products also contains small shares of lithium silicate and lithium alumosilicate phases which are not clearly to identify in all cases. In addition the samples still contain bromide bearing compounds causing hygroscopic behavior of the as synthesized powders.

The morphology and size of the particles give information about the expected compaction behavior of the material for following pressure experiments. Figure 32 shows SEM pictures of a comparable Si-rich powder sample (ALS-72, left) and an Al-rich sample (ALS-47, right).
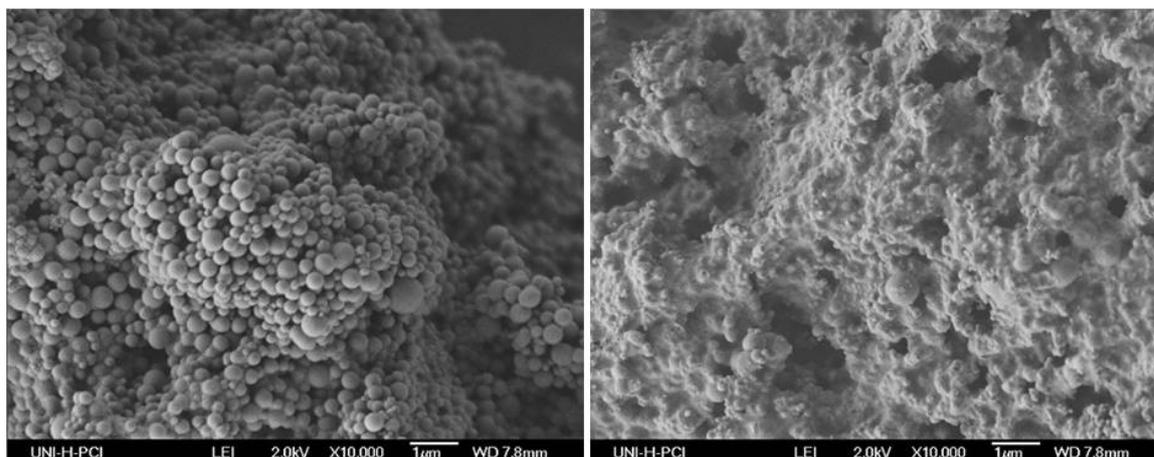
Figure 32: SEM images of a Si-rich (left) ALS-72 with an Al/Si (mass%) ratio of 2.31 and an Al-rich sample (right) ALS-47 with an Al/Si (mass%) ratio of 4.48. Values derived from EDX measurements, cf. table 6. (Picture used with the consent of Isabella Laskowski)

The silicon rich sample is made of clearly distinguishable spherical particles with a consistent particle size around 500 nm (estimated from SEM pictures). The aluminium rich sample on the right has a slurry appearance at the surface and only a small amount of clearly distinguishable spherical particles are observable. The composition of the powders control the morphologic appearance of the material and higher silicon contents lead to a more pronounced spherical and dry appearance. Following the XRD result, a higher content of hygroscopic halogenide phases might explain this result due to hydrolysis reactions taking place at the surface.

3.2.3.2 Composition

The compositions of the powders were determined by EDX analysis. For a more accurate determination of lithium content two samples (cf. remarks in table 6) were analyzed by ICP-OES with the same experimental procedure, given in Chapter *1.4.1.* for lithium content determination of the bulk lithium alumosilicate glasses.

The bromide content of the samples was determined by Volhard titration [96]. For this, all hygroscopic bromide compounds are dissolved by mixing the powder with water.

Afterwards, an excess of silver nitrate solution is added to the solution and the dissolved bromide ions precipitate as solid silver bromide while a certain excess of silver ions remains in solution. For endpoint indication acidified $Fe(NO3)_{3,(aq)}$ is added to the solution. The dissoluted silver ions are precipitated with thiocyanate ions to solid silver thiocyanate by titration with ammonium thiocyanate solution of known concentration. The equivalent point is reached when all silver ions are precipitated and the added thiocyanate ions react with the indicator to form red $Fe(SCN)_{3,(aq)}$. From the consumed volume of standard thiocyanate solution, the original molar content of bromide in the powder can be calculated.

The described determination of bromide content was carried out by inserting around 25 mg of sample powder in 10 mL of deionized water. Then 5 mL of silver nitrate solution with a concentration of 0.1 mol/L are added to the emulsion of water and sample powder. Afterwards 2 mL of a self-made indicator solution are added. The indicator solution was made by adding of 551 mg $Fe(NO_3)_3$ to 16 mL deionized water and 4 mL of 65 wt% nitric acid. The resulting sample solution is then titrated with 0.01 mol/L ammonium thiocyanate solution until a staying color change from colorless to slight red occurs at the equivalent point.

To ensure the necessary accuracy of the method, the titer of the ammonium thiocyanate standard solution was determined before every set of titration analysis was carried out. For this a standard solution of NaCl was made by adding 5.86138 g of dried $NaCl_{(s)}$ (120 °C for 3 to 4 hours) with deionized water as standard titrimetric substance. With this solution the titer of a 0.1 mol/L of self-prepared $AgNO_3$-solution in water was determined with the method of Mohr-titration [Jander 1995], using potassium chromate solution as indicator. Then titer of the ammonium thiocyanate solution was determined by titration with the silver nitrate solution with known concentration. The overall accuracy of the described method including standard solution calibration stays below ± 1.2 rel. %, corresponding to

± 0.6 wt% for high bromide concentration around 50 wt% and ± 0.06 wt% for lower concentration around 5 wt%.

The findings of the halogenide analyses showed high bromide contaminations of the obtained powders. As indicated by XRD analyses the powders do not only contain lithium alumosilicate or lithium silicate phases but other bromide bearing phases like LiOBr, which could not be fully quantified by the used methods. The lithium ions are likely distributed between the amorphous lithium silicate and lithium alumosilicate phases and the hygroscopic bromide bearing phases. For that, the analyzed lithium conducting phenomena cannot be attributed to the silicate and alumosilicate phases alone, but are a collective effect of all enclosed phases.

Table 6 shows a representative selection of obtained powder compositions with the remark that these compositions are idealized results of the EDX analyses and do not take in consideration the not fully quantified occurrence of bromide bearing phases. The amount of bromide in the powders is an indication for their abundance.

The samples show a higher share of aluminium oxide than silicon oxide, what is remarkable in comparison to the analyzed glasses in chapter 1, which contain more silicon oxide than aluminium oxide (with the exception of PET). In general, the bromide phases have a high share in the powders (11.10 to 46.50 wt%). That will influence their conductivity characteristics and the compaction behavior. The highest bromide content can be found in the samples derived from the oxygen inlet pipe synthesis route. These samples show the highest content in lithium, too.

Table 6: Composition of CVS powders obtained by different synthesis routes. Aluminium oxide and silicon oxide contents were determined by EDX analysis, Lithium oxide content calculated to 100 %. Bromide content was determined by Volhard-titration given as wt% of powder weight as indication for bromide bearing phase abundance. Remark: iO = increased oxygen flow, W = humidified oxygen stream, Op = inlet tube for oxygen application. n.b.: not determined. The lithium content of ALS-47 and ALS-72 was also verified by ICP-OES measurements. For ALS-47 a mean of 2 ICP-OES measurements gives an absolute Li content of 39.9 g Li/kg sample (39.6 g Li/kg sample and 40.2 g Li/kg sample) in comparison to 15.1 g Li/kg sample calculated from EDX results. For ALS-72 the ICP-OES measurement gives a Li content 49.8 g Li/kg sample in comparison to 40.7 g Li/kg sample calculated from EDX results. Last column gives information which crystalline phase could be identified in XRD (with unknown share).

Experiment	Li_2O	Al_2O_3	SiO_2	Br	Al/Si	Li/Al	O/Br	crystalline
		mol%		wt%				phase
ALS-85iO	8.70	76.30	15.00	44.10	10.17	0.11	5.42	
ALS-47	9.04	62.90	28.06	n. d.	4.48	0.14		$LiAl_5SiO_8$
ALS-37	10.57	67.20	22.23	n. d.	6.05	0.16		
ALS-86iO	10.60	65.40	24.00	11.80	5.45	0.16	20.47	
ALS-40	13.08	62.77	24.15	n. b.	5.20	0.21		
ALS-46	13.80	59.90	29.30	30.80	4.09	0.23	7.90	
ALS-81W	12.40	47.00	40.60	11.10	2.32	0.26	22.21	Li_2SiO_3
ALS-82W	17.80	42.70	39.50	43.50	2.16	0.42	5.69	
ALS-72	20.70	41.50	37.80	n. b.	2.20	0.50		LiOBr
ALS-87Op	30.10	35.80	34.10	46.50	2.10	0.84	5.35	
ALS-88Op	29.10	33.10	37.80	46.20	1.75	0.88	5.41	
CBS-91	8.91	18.61	72.48	n. d.	0.51	0.48		

This is an indication that lithium is not only bound in the lithium silicate and alumosilicate phases but also has a high abundance in the bromide bearing phase. Especially the identified phase LiOBr exhibits a 1:1 molar ratio of lithium and bromide what supports a relationship between lithium and bromide content. This is not valid for all samples, meaning that the distribution of lithium can be variable between the phases occurring in the powders.

Using the following ternary diagram, the compositions of the amorphous lithium alumosilicate glasses (cf. chapter 1) and the amorphous phases, obtained by CVS, are compared.
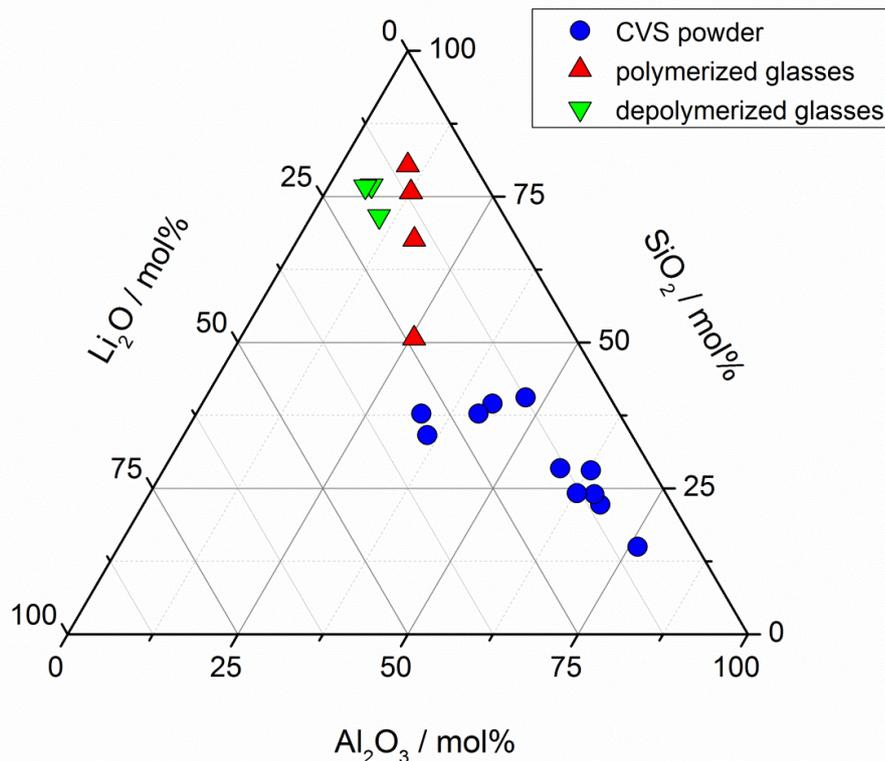
Figure 33: Ternary diagram of powder and glass compositions for comparison of compositions available by different synthesis methods. The ternary diagram is given with the constraint of phase mixing problem and contamination with remaining bromide.

As shown in figure 33, both systems display different compositional regions in the lithium alumosilicate system. The CVS method allows synthesizing aluminium rich amorphous lithium alumosilicate materials, which are less accessible by melt quenching methods. A remarkable drawback in the synthesis route used here, is the contamination with remaining precursors and the difficult evaluation of phase purity and composition.

3.2.4 Li mobility in non-compacted powder samples

The ionic conductivity and diffusive characteristics of ions in powdery materials are difficult to determine, because no solid electrode can be attached to measure a direct or alternating current response of the material without pressing pellets of it. To get access to lithium mobility, a contactless spectroscopic method needs to be applied. We decided to

use ^{7}Li solid state NMR spectroscopy to determine the lithium ion diffusivity characteristics in the synthesized powders, because the determination of lithium mobility in completely untreated powder samples is possible.

3.2.4.1 Solid-state ^{7}Li-NMR results

Solid-state NMR spectroscopy [97] uses electromagnetic pulses to determine the surrounding of an NMR active nucleus. The electromagnetic pulse induces spin alignment of NMR active nuclei. This alignment collapses in absence of the electromagnetic field by interactions with the neighboring matrix. The electromagnetic response of the system allows conclusion on the chemical characteristics of the neighboring structures of the nuclei and its interaction with it. In case of lithium, both stable isotopes (^{6}Li, spin = 1 and ^{7}Li, spin = 3/2) are suitable for solid state NMR analysis [98].

For the analysis the ^{7}Li spin alignment echo NMR is used to analyze the interaction of lithium ions with each other and the surrounding matrix. For this, motional narrowing curves were obtained in collaboration with the Institute for Physical Chemistry at the University of Hanover in the framework of FOR 1277 Molife. Thanks go to Benjamin Rupprecht for measuring the NMR spectra and data processing.

The NMR spectra show a peak for ^{7}Li. The full width at half maximum (fwhm) of this peak is temperature dependent. The temperature dependency of this fwhm value shows typically two plateaus with a transition region as seen in Fig. 34. The broadening of the line width indicates a freezing of the analyzed ion in its chemical matrix due to lower energy of the network building units to vibrate. This state is called rigid lattice. Less movement in the surrounding structures means less probability of interactions and because of this, a hindered decomposition of the induced spin alignment [98], [99].
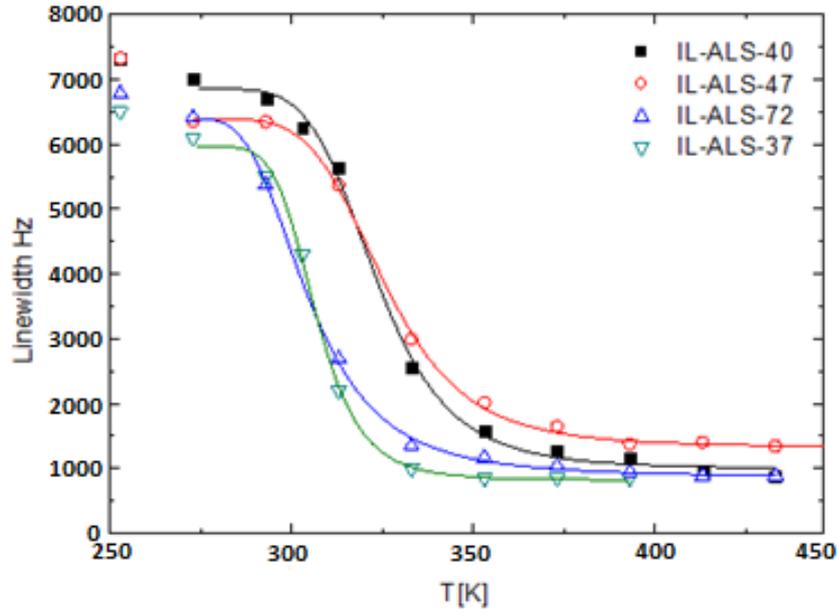
Figure 34: Motional-narrowing-curves from ^{7}Li-NMR-measurements of CVS products. Solid lines represent fits with the Hendrickson-Bray relationship. (Picture used with the consent of Isabella Laskowski)

The obtained curves were fitted with the help of the Hendrickson-Bray relationship [100].

$$w = \frac{A}{1+\left(\frac{A}{B}-1\right)} \cdot e^{\frac{-E_a}{kT}} + D \qquad (11)$$

Where w is the line width at half maximum (or full width at half maximum; fwhm) of the lithium resonance peak. A represents the inverse of the T_{2A} relaxation time of lithium ions in a non-excited state, B represents the inverse T_{2B} relaxation time of lithium ions in a thermally excited state. D is a constant line broadening term. E_a is the activation energy of lithium mobility, T is the absolute temperature and k the Boltzmann constant.

From the obtained curves, three parameters can be derived: $T_{inflection}$, T_{onset} and the *fwhm* value for the rigid lattice $v_{fwhm-rl}$. $T_{inflection}$ corresponds to the temperature at the inflection point of the curve. T_{onset} represents the minimum temperature for starting lithium mobility within the lattice and the point of a weakening of the rigid lattice. It can be seen in Fig. 34

when the fwhm values start to decrease with increasing temperature. This process might be interpreted as a "melt" temperature of the "freezing state" the lithium ions are trapped at low temperatures in the rigid lattice. The theoretical line width at 0 K $v_{fwhm-rl}$ obtained from the motional narrowing curve, allows the calculation of the lithium jump rate $\tau_{Li,\ inf.}$ at the inflection point temperature according to

$$\tau_{Li,inf} = 2 \cdot \pi \cdot v_{fwhm-rl} \tag{12}$$

One major drawback of this method to determine jump rates of lithium in the powders are the large uncertainties. The fit parameters depend strongly on the chosen model and additionally, the fit deviate from measured data especially at low temperatures as seen in Fig. 34. This leads to large errors for derivative parameter. Because of this, the data shown in table 7 are just approximate values. Especially the values for E_a show a large error and are perhaps more methodically based than outcomes of systematically changes in the powders, while the uncertainties in T_{onset} are less pronounced and give an indication for structural differences. There are no indications for a systematic dependence of the calculated parameters and the analyzed chemical composition, represented by the lithium to aluminium ratio in table 7.

Table 7: Motional narrowing parameter obtained from Hendrickson-Bray fit and calculated jump rates at the temperature of the inflection point.

CVS powder	Li/Al	E_a	T_{onset}	T_{inf}	$\tau_{Li,\ inf}$
	at. ratio	eV	K	K	$10^4\,s^{-1}$
ALS-47	0.14	0.460	288	330	4.52
ALS-37	0.16	0.781	283	307	4.10
ALS-40	0.21	0.616	291	324	4.84
ALS-81W	0.26	0.470	297	345	4.60
ALS-72	0.50	0.781	286	308	4.20

The activation energies for lithium mobility show no significant correlation with synthesis route or composition. The E_a value of ALS-37 and ALS-72 are comparable to the activation energy in petalite glasses, described in chapter 1 (PET), ALS-40 shows a slightly lower activation energies than the bulk glasses, but all three samples have a much higher aluminium oxide content than the glasses and there is no correlation between activation energy and composition between the bulk glasses and the powders. The samples ALS-47 and ALS-81W have significantly lower activation energies than all 7 analyzed bulk glasses, but they also show no compositional correlation: ALS-47 has comparable composition like ALS-37, while sample ALS-81W has a similar composition compared to ALS-72. As mentioned above the values for E_a derived from the Hendrickson-Bray fit have a large uncertainty what might explain the missing correlation to composition or synthesis route.

The lithium jump rates are comparable for all analyzed powders, but the inflection point temperature shows larger variation. Powder ALS-37 und ALS-72 reach the jump rate of $4.10 \cdot 10^4$ s^{-1} respectively $4.20 \cdot 10^4$ s^{-1} at lower temperatures of 307 K, while the other samples need higher temperatures to reach those values for $\tau_{Li, inf}$. The given numbers of the jump rates are suitable to show impacts of compaction processes on the powders and their conductivity behavior.

3.3. Compaction of CVS powders

The CVS powders are compacted at elevated temperatures and pressures up to 450 °C and 2 kbar in externally heated cold seal pressure vessels (CSPV). This leads to reactive sintering of the particles and the formation of solid, macroscopic disks. The conductivity characteristics in those disks are determined in terms of using impedance spectroscopy as described in chapter 1.

3.3.1 Compaction procedure

To compact the CVS powders, each sample was placed into a gold capsule of 10 mm length and 4 mm diameter. The capsules were made of a gold tube. Before filling the tube was cleaned in acetone and annealed at 800 °C for 10 minutes to soften the gold. After quenching it in distilled water one end of the tube was shut welded with a Lampert PUK 3 arc welding instrument. Then about 80 mg of the sample powder was weighed into the open capsule and dried in an oven at 120 °C for about 3 to 4 hours to drive out potentially absorbed water from the powder. Afterwards the capsules were shut welded. The now closed capsules were pressed in a bench vise to flat disks to predetermine the later form of the compacted material. The flat capsules are compacted in an externally heated cold seal pressure vessel (CSPV) (cf. Fig. 35 a) by applying 1 to 2 kbar of argon gas pressure to the vessel. The pressure is provided by an oil hydraulic cylinder intensifier (cf. Fig. 35 b).

The samples were compacted at temperatures of 523 to 723 K and at pressures of 1 to 2 kbar for 1 to 2 hours. These experimental parameters were chosen to get a sufficient sintering of the particles, without inducing major crystallization or phase changes in the sample.
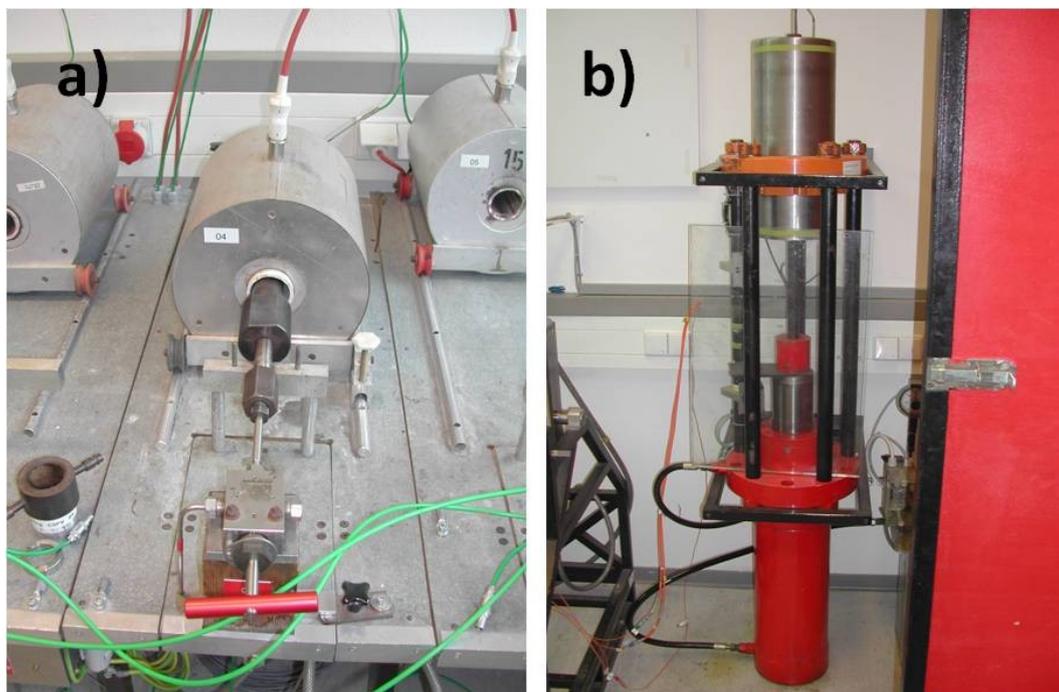
Figure 35: a) Cold seal pressure vessel in a tube furnace with connection to the argon high pressure intensifier. The sample capsule is arranged in the rear part of the autoclave. b) Oil hydraulic pressure intensifier with high pressure exit at the upper end.

After placing the capsule into the autoclave the sample is positioned in the cold zone by rotating the autoclave in a vertical position. Then the autoclave is pressurized to its end pressure and heated to its end temperature controlled by a thermocouple inserted in the back end of the autoclave wall. After reaching a constant temperature and pressure the sample is moved into the heated zone by rotating the whole system (including the oven) in a vertical position. After the sample falls into the hot zone of the autoclave the compaction time starts.

After the compaction at elevated temperatures the samples were quenched by rotating just the autoclave in vertical position outside the oven to let the sample falls down in the cold bottom end of the autoclave. To open the autoclave it was cooled down to room temperature by compressed air cooling. To keep the sample in the cold zone during the heating process and quenching of the sample after the compaction is necessary to achieve a controlled time span at the target temperature. That minimizes changes in the sample

during the heating and cooling process and allows an accurate control of compaction parameter. To investigate the influence of elevated compaction temperatures some powders were compacted at room temperature at 5 kbar for 5 hours with the help of a hand driven oil hydraulic laboratory press typically used to press KBr pellet for infrared spectroscopy.

After compaction of the capsules in CSPV, a disk of approximately 2 to 3 mm in length and width and a thickness about 0.5 mm were cut out the capsules with a circular saw. Most of the samples were mechanically very sensitive and the cutting process was not successful due to mechanical damage of the sample. These samples were not suitable for impedance spectroscopy measurements, because no stable electrical contacts could be attached to them. Another problem was high hygroscopic behavior of these disks. Anyway, out of 23 conducted compaction experiments, 3 lead to solid and mechanically stable disks suitable for applying contacts (13 % of the experiments). These disks were sputtered with gold electrodes on each side for impedance spectroscopy measurements. IS measurements on the disks were carried out with the same experimental procedure described in chapter 1.

3.3.1.1 Crystallization processes

During the compaction crystallization processes occur due to the abundance of instable and reactive amorphous phases. Furthermore, the remaining bromide phases in the powders can induce a higher reactivity and promote crystallization processes. The temperature and duration is chosen to minimize this effect but crystallization processes are observed. Fig. 36a) shows the XRD pattern of the compacted CVS powder sample ALS-37. Before compaction it is amorphous with a low share of crystalline particles. An identification of the crystal phase was not possible. After compaction at 723 K and 2 kbar the sample (compacted disk K1-37 derived from ALS-37) shows a crystalline phase which is not

clearly identified (cf. Fig. 36b). The most intense peak in the pattern at 25° 2Θ is in good accordance with the most intense reference peak of mullite ($Al_6Si_2O_{13}$) in terms of 2Θ and intensity, but the overall accordance with the reference XRD pattern is not good enough for an explicit identification. The presence of crystalline aluminium oxide could be foreclosed by comparison with XRD reference pattern. The comparison with the annealed sample is shown in Fig. 36c): After annealing of the sample at 1273 K in air the XRD pattern could be identified as Lithium aluminium oxide $LiAlO_2$ in good agreement to the reference pattern.
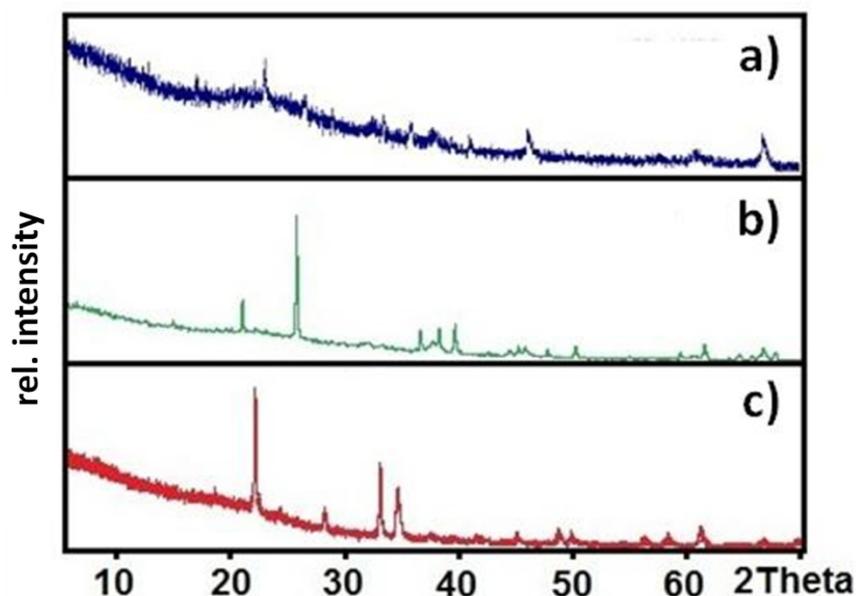
Figure 36: XRD pattern of a CVS powder and its compaction products. a) CVS powder ALS-37. b) Sample K1-37, compacted at 723 K/ 2 kbar. b) After sintering at 1273 K in air (Picture used with the consent of Isabella Laskowski)

The used compaction method at elevated at temperatures up to 723 K and pressures of 1 to 2 kbar leads to an intermediate crystallization of the CVS powder. The formed crystalline phases differ strongly from phases obtained by high temperature sintering.

3.3.2 Conductivity characteristics of compacted powders

The conductivity measurements of compacted CVS powders reveal comparable results to the melted glasses. Fig. 37 shows impedance spectra of the compacted disk K1-37 made of CVS powder sample ALS-37. The spectra quality is reasonable good. The appearance of the curve follows a typical solid ionic conductor behavior with an increasing admittance in the low frequency domain due to ion blocking electrodes used in the experiment. At average frequencies a frequency independent conductivity plateau represent the direct current ionic conductivity value. In the high frequency domain the dispersion region appears in the spectrum measured at 223 °C and is denoted at 293 °C.
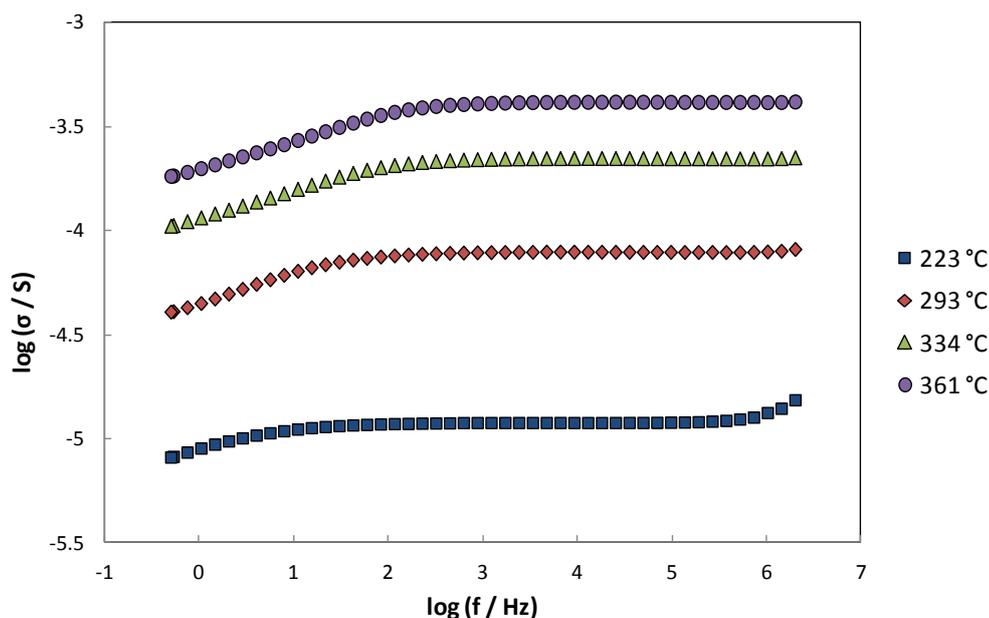
Figure 37: Representative impedance spectra of compacted disk K1-37 at selected temperatures. Cell constant K equals 0.0046 for these measurements.

In figure 38 and figure 39 the Cole-Cole plots [101] (or Nyquist plot [36]) of the impedance spectroscopy response at 432 K of eucryptite glass (cf. chapter 1: sample EUC) and the compacted disk K1-37 is shown. In this data representation the frequency increases from right to left.
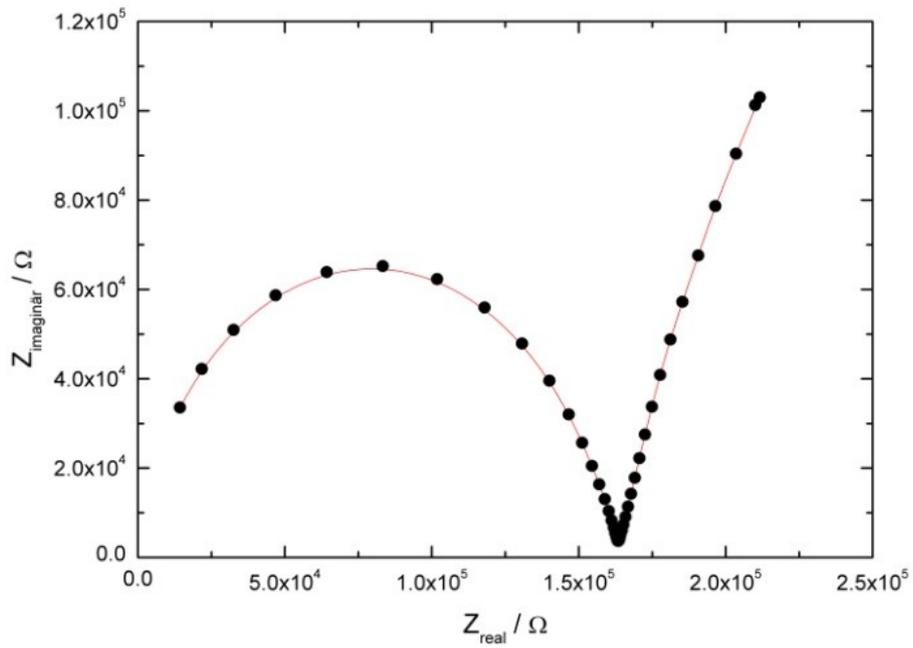
Figure 38: Cole-Cole plot of impedance measurement of LiAlSiO$_4$ glass (EUC) at 423 K.

Both materials show typical behavior of solid ion conductors with one dominant conducting mechanism represented by one half circle.
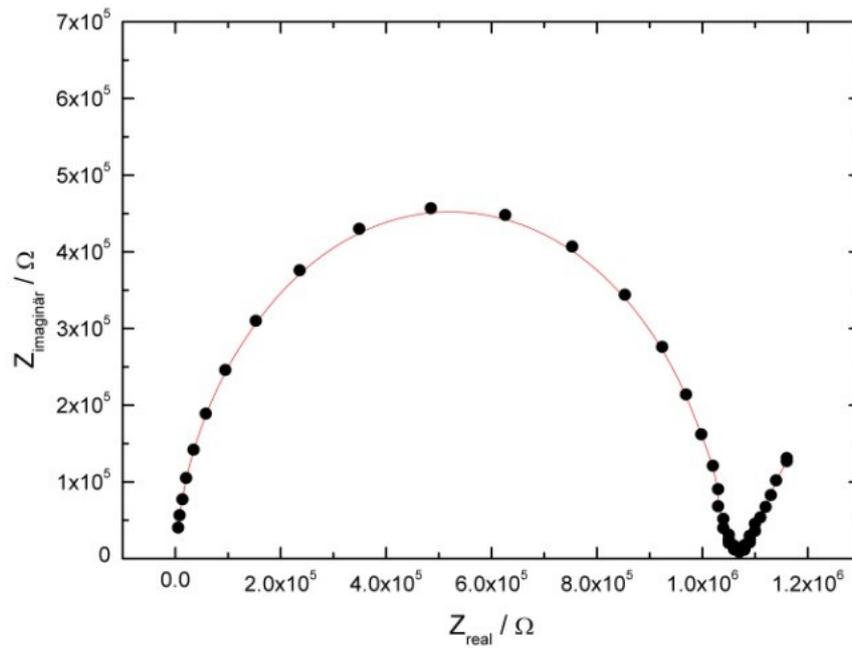
Figure 39: Cole-Cole plot of impedance measurement of compacted sample K1-37 at 423 K.

Although sample K1-37 contains a not negligible share of crystalline phases (cf. Fig. 36) only one mechanism for ion conductivity can be observed here. As first assumption the typically less conducting character of crystalline phases of the analyzed lithium alumosilicate system [33] is covered here by the more conducting characteristics of the amorphous phases. There are indications, that the crystalline share might be mullite (cf. *3.3.1.1*). In this case, no contribution of the crystalline share is expected due to the missing charge carrier in mullite.

For 3 CSPV compacted (K2-91, K3-91, K1-37) and 1 ambient temperature compacted (ATP-40) disks, the temperature dependent specific conductivity values were recorded by impedance spectroscopy. Fig. 40 shows the results in an Arrhenius plot. For comparison bulk glass values of EUC and PET (cf. chapter 1) and data on crystalline spodumene are added.
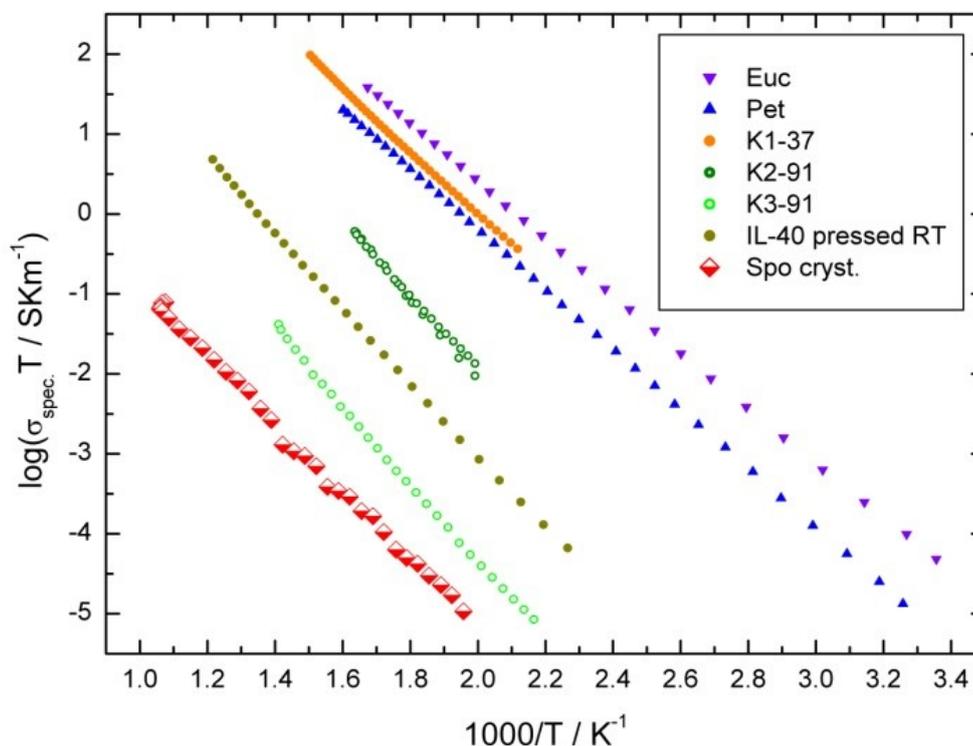
Figure 40: Arrhenius diagram of compacted powders, compared to glasses and spodumene single crystal data. SPO crystal data is taken from Welsch 2012 [33] and represent spodumene (LiALSi$_2$O$_6$) single crystal conductivity data.

All samples show classical Arrhenius behavior with linear dependence of the temperature corrected specific conductivity to the inverse temperature. The crystalline spodumene has the lowest specific conductivity, the amorphous bulk glass sample the highest. At 500 K the temperature corrected specific conductivity of EUC is about 6 orders of magnitude higher than of SPO ($\sim 10^{-5}$ SKm^{-1} for EUC and $\sim 10^{1}$ SKm^{-1} for EUC). Values for the CVSP compacted powders vary within this complete range: Sample K2-91 shows a low specific conductivity comparable to the crystalline spodumene, sample K1-37 has a high specific conductivity comparable to the bulk glasses EUC and PET. The cold pressed sample ATP-40 and sample K2-91 appear in the intermediate range.

From linear fits of the curves Arrhenius parameters following the Nernst-Einstein equation (2) are calculated. The results are shown in table 8. For comparison, the corresponding values for the melt quenched glasses (cf. chapter 1) are given within this table.

Table 8: Arrhenius parameter of conductivity data of CVS powder and glasses. Given Δ-values represent standard deviation values from fit

sample comp. powder	$T_{compaction, max}$ K	Li_2O	Al_2O_3 mol%	SiO_2	Li/Al	A_0 10^6 SKm^{-1}	ΔA_0 10^6 SKm^{-1}	E_a eV	ΔE_a eV
K2-91	623	8.91	18.61	72.48	0.48	40.40	12.00	0.952	0.014
K3-91	723	8.91	18.61	72.48	0.48	0.19	0.02	0.954	0.006
K1-37	723	10.57	67.2	22.23	0.16	77.30	4.70	0.790	0.003
ATP-40	298	13.08	62.77	24.15	0.21	1.96	0.16	0.962	0.004
glasses									
EUC		23.72	25.59	50.69	0.93	29.40	1.60	0.700	0.010
SPO		15.24	17.12	67.63	0.89	26.20	0.57	0.715	0.004
FSP		11.68	12.59	75.73	0.93	30.50	0.92	0.731	0.006
PET		9.81	9.80	80.39	1.00	22.60	1.30	0.752	0.011
DG1		18.44	9.97	71.59	1.85	25.80	2.00	0.793	0.014
DG2		16.88	6.23	76.89	2.71	26.00	1.70	0.800	0.012
DG3		17.92	5.38	76.70	3.33	28.80	1.30	0.808	0.008

Only K1-37 can come up with a comparable conductivity to the analyzed bulk glasses if compacted at elevated temperatures. At ambient temperature, compaction is not suitable even at higher pressures of 5 kbar as seen at ATP-40, which composition is comparable to K1-37. Is the compaction temperature high enough to induce significant crystallization the

conductivity drops, what can be seen in the comparison of K2-91 and K3-91. The specific conductivity of the powder compacted at 632 K is about 2 orders of magnitude higher than in the powder compacted at 732 K, although the disks are made of the same starting material. The activation energies of compacted powders K2-91, K3.91 and ATP-40 are similar and significantly higher than in the bulk glasses (about 0.25 to 0.26 eV in comparison to EUC), but pre-exponential factors are varying strongly from $0.19 \cdot 10^6$ SKm^{-1} for K3-91 to $40.40 \cdot 10^6$ SKm^{-1} for K2-91, more than one order of magnitude. Differences in specific conductivity of these samples seem to be derived from the influence of the compaction parameter on the pre-exponential factor and not on the activation energy. This might be explained with a common characteristic in activation barriers for lithium movement in the materials while the entropy of transition states, connected to the pre-exponential factor, is influenced by compaction temperature and duration.

Activation energy of sample K1-37 is 0.27 eV lower than E_a of the other CSPV-compacted powders and the value of 0.79 eV is more comparable to the bulk glasses. Also the pre-exponential factor is in a similar range as the glasses what leads to a similar specific conductivity as mentioned above.

To compare the compacted materials and solid glasses with the obtained ^{7}Li solid state NMR jump rates given in table 7, the impedance spectroscopy derived conductivity data are calculated into jump rates, using the Einstein-Smulochowsky equation

$$\tau = \frac{a^2}{6 \cdot D} \qquad (13)$$

with diffusion coefficient D, average jump distance a and the jump rate τ. The jump distance a is derived from glass densities and the assumption, that all lithium ions are uniformly distributed within the material. For the compacted powders the density of PET

was assumed because a direct density determination of the powders was not suitable. Diffusion coefficients for the compacted plates were calculated with the Nernst-Einstein equation as described in chapter 1. In Fig. 41 the calculated jump rates for glasses, compacted powders (derived from IS) and non-compacted powders (derived from NMR) are plotted against the inverse temperature.
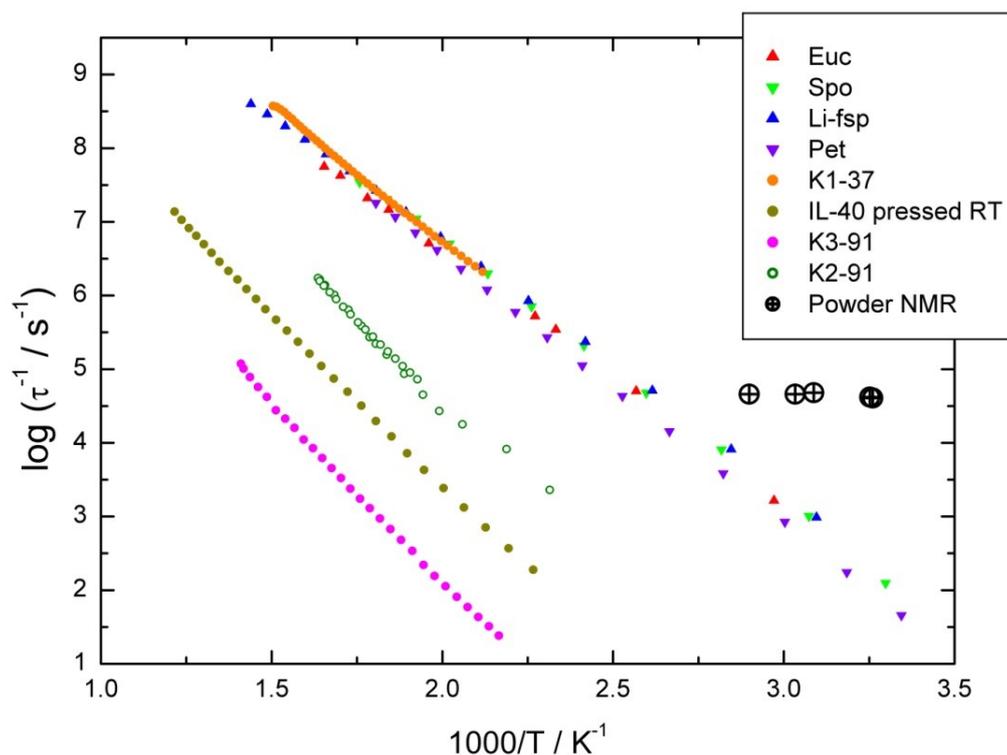
Figure 41: Comparison of jump rates of lithium in glasses, compacted powders and non-compacted as synthesized CVS powders (cf. Tab. 7).

The non-compacted powders show the highest lithium jump rates within the regarded samples. The jump rates in bulk glasses are 2 to 3 orders of magnitude lower than in the as synthesized powders and show a narrow distribution in comparison to the compacted and non-compacted powders. The lowest jump rates are calculated for the compacted powders with exception of sample K1-37, which behaves like the bulk glasses. The values for τ^{-1} in the compacted powders are several orders of magnitude lower, if the linear trends of the curves are interpolated to room temperature.

Lithium mobility in the bulk glasses is determined by the amorphous structure of the alumosilicate matrix as discussed in chapter one. Structural elements like $AlO_4^{(-)}$ sites or non-bridging oxygen atoms influence the lithium mobility there (cf. discussion in chapter 1). The CVS powder synthesis as carried out does not allow the formation of a distinct and homogenous phase and lithium can be incorporated into the amorphous phase or bromide bearing phases (like LiOBr, identified by XRD). The lithium mobility in those powders is not determined by the alumosilicate matrix of the amorphous phase but more likely by the abundance of bromide and mixed phases and their share of lithium in the material.

In bulk glasses the structural differences of lithium alumosilicate phases lead to a maximal difference of 0.5 log units between EUC and PET in terms of jump rates (cf. Fig. 41). The differences within the compacted powders and between compacted powders and as synthesized powders are much larger and cannot be explained just by differences in structural changes of an amorphous alumosilicate matrix with incorporated lithium ions. This is a strong indication, that lithium is mostly incorporated in bromide or oxy-bromide phases. In these phases lithium shows high mobility and jump rates detected by ^{7}Li solid state NMR. The compaction process leads to the formation of particle and grain boundaries in the material. Furthermore, crystallization processes occur. As shown in fig. 40 at the example of spodumene, the crystalline phases exhibit a much lower conductivity than the amorphous lithium alumosilicate phases. But due to the assumption that most lithium ions are not incorporated in those structures, crystallization processes can only explain a small part of the jump rate decrease induced by CSPV compaction. It is more likely that the bromide and oxy-bromide phases where most lithium is bound, do not provide an interconnection for long- and mid-range lithium transport. Assuming a homogenous mixing of all occurring phases in the powder there are no percolation paths for correlated lithium movement like in the bulk glasses.

Additionally, grain boundaries and particle surfaces hinder the lithium mobility in the compacted powders. These boundaries do affect the impedance spectroscopy measurements where the jump rates are derived from, while the NMR spectroscopy is influenced by the local environment of the Li^+ ions and less by long range effects.

Sample K1-37 is an exception to this and has similar activation energy, pre-exponential factor and τ^{-1} values as the bulk glasses. This is an indication, that this sample contains a higher share of lithium in an amorphous alumosilicate environment and can provide interconnected diffusive pathways, like the glasses for lithium ions. But due to the difficult quantification of the lithium share in amorphous alumosilicate phase and bromide or oxy-bromide phases this result can also base on a higher degree of connection of lithium conducting bromide bearing phases. A differentiation of both possibilities cannot be drawn within the data of this study.

To improve the significance of the obtained data, further improvements of the analysis of composition and phase identification have to be made to distinguish between contributions of lithium ions incorporated in a lithium alumosilicate network and lithium ions which are bound to remaining bromide or oxy-bromide phases. Additionally the abundance of water due to the hygroscopic character of at least LiOBr is likely in the powders. These contaminations may induce additional charge carrier possibilities like proton and bromide conduction influencing the conductivity measurements and the compaction process overall.

To improve the suitability of the compacted CVS powders as fast ion conductors, improvements of the CVS process have to be made. The synthesis parameters have to be optimized to allow a complete reaction of all precursor molecules to a pure lithium alumosilicate phase without the formation of bromide or oxy-bromide phases. The experimental setting used here are not suitable to reach this goal. For data interpretation the aspect of the unknown phase distribution and lithium distribution within the phases are the

main drawback to draw conclusions between synthesis parameter and results of lithium conductivity measurements.

3.4. Conclusion

Amorphous lithium alumosilicates derived from chemical vapor synthesis are suitable as precursors for compaction to fast ion conducting solid materials. Under certain conditions they can reach conductivity values comparable to lithium alumosilicate glasses derived from melt quench processes already known for their fast ion conducting characteristics. Although a direct comparison between both materials in terms of composition and conduction mechanism is difficult due to drawbacks of the used CVS process. The used synthesis parameters do not lead to pure amorphous lithium alumosilicate powders and bromide and oxy-bromide bearing phases are precipitated within the process which cannot be easily quantified with the used analytical methods.

To optimize this process, changes in the CVS process have to be made to ensure chemical and phase pure products. Synthesis parameters have to be found to enable a complete reaction of precursors to phase pure products to minimize contamination with remaining precursor. Also a better determination of composition and improved phase analysis is necessary. A combination of ICP-OES and EMPA could be helpful to determine the chemical composition, as it was done with the bulk glasses described in chapter 1. In general, an improved CVS process allows the synthesis of aluminium-rich amorphous lithium alumosilicates which are suitable as precursors for CSPV compaction at elevated temperatures to obtain fast lithium ion conductors.

4. References

[1]   W. van Gool, *Fast Ion Conduction*, Annu. Rev. Mater. Sci., **1974**, 4, 311-335

[2]   W. Nagel, H. Böhm, *Ionic Conductivity Studies on LiAlSIO₄-SiO₂ Solid Solutions of the High Quartz Type*, Solid State Communications, **1982**, 42-9, 265-631

[3]   V. V. Kharton, F. M. B. Marques, A. Atkinson, *Transport properties of solid oxide electrolyte ceramics: a brief review*, Solid State Ionics, **2004**, 174, 135-149

[4]   P. Knauth, *Inorganic solid Li ion conductors: An overview*, Solid State Ionics, **2009**, 180, 911-916

[5]   K. L. Ngai, *The Universal low Frequency Response of Ionic Conductors: A Review of Data and a unified Model Interpretation*, Solid State Ionics, **1981**, 5, 27-34

[6]   A. K. Jonscher, *Dielectric relaxation in solids*, J. Phys. D: Appl. Phys., **1999**, 32, R57-R70

[7]   A. K. Jonscher, *Analysis of the alternating current properties of ionic conductors*, Journal of Materials Science, **1978**, 13, 553-562

[8]   A. K. Jonscher, *The `universal`dielectric response*, Nature, **1977**, 267, 673-678

[9]   S. Kunugi, T. Kyomen, Y. Inaguma, M. Itoh, *Investigations of Isotope Effect of Lithium Ion Conductivity in (La, Li)TiO₃ single Crystal*, Electrochemical and Solid-State Letters, **2002**, 5, A131-A134

[10]   C. A. Angell, *Mobile Ions in Amorphous Solids*, Annu. Rev. Phys. Chem., **1992**, 43, 693-717

[11]   Z. Gadjourova, Y. G. Andreev, D. P. Tunstall, P. G. Bruce, *Ionic conductivity in crystalline polymer electrolytes*, Nature, **2001**, 412, 520 - 523

[12]   H. Mehrer, *Diffusion in Solids – Fundamentals, Methods, Materials, Diffusion-controlled processes*, Springer Verlag Berlin Heidelberg, Series in Solid-State Sci., **2007,** 155 ff.

[13]   K. Funke, *Jump Relaxation in Solid Electrolytes*, Prog. Solid St. Chem., **1993**, 22, 111-195

[14]   A. Kuhn, M. Wilkening, P. Heitjans, *Mechanically induced decrease of the Li conductivity in an alumosilicate glass*, Solid State Ionics, **2009**, 180, 302-307

[15]   D. R. Lide, CRC Handbook of Chemistry and Physics, 82nd Edition, **2001**, published by CRC Press LLC

4. References

[16]   W. G. Lee, S. I. Woo, J. C. Kim, S. H. Choi, K. H. Oh, *Preparation and properties of amorphous TiO2 thin films by plasma enhanced chemical vapor deposition*, Thin Solid Films, **1994**, 237, 105-111

[17]   T. Adachi. S. Sakka, *Preparation of monolithic silica gel and glass by the sol-gel method using N,N-dimethylformamide*, Journal of Materials Science, **1987**, 22, 4407-4410

[18]   F. Mizuno, A. Hayashi, K. Tadanaga, M. Tatsumisago, *New, Highly Ion-Conductive Crystals Precipitated from Li$_2$S-P$_2$S$_5$ Glasses*, Adv. Mater., **2005**, 17, 918-921

[19]   R. J. Hemley, N. W. Ashcroft, *The Revealing Role of Pressure in the Condensed Matter Sciences, Physics Today*, **1998**, Aug., 26-32

[20]   L. Merill, W. A. Bassett, *Miniature diamond anvil pressure cell for single crystal x-ray diffraction studies*, Rev. Sci. Instrum, **1974**, 45-2, 290-294

[21]   H. Huppertz, *Multianvil high-pressure / high-temperature synthesis in solid state chemistry*, Z. Kristallogr., **2004**, 219, 330-338

[22]   A. Kuhn, M. Wilkening, P. Heitjans, *Mechanically induced decrease of the Li conductivity in an alumosilicate glass*, Solid State Ionics **2007,** 180, 302–307

[23]   H. Staesche, S. Murugavel, B. Roling, *Nonlinear Conductivity and Permittivity Spectra of Ion Conducting Glasses*, Z. Phys. Chem. 223, **2009**, 1229-1238

[24]   U. Bauer, A.-M. Welsch, H. Behrens, J. Rahn, H. Schmidt, I. Horn, *Li Diffusion and the Effect of Local Structure on Li Mobility in Li$_2$O-SiO$_2$ Glasses*, J. of Phys. Chem. B, **2013**, 117, 15184-15195

[25]   D. Raistrick, Chun Ho, R. A Huggins, *Ionic Conductivity of Some Lithium Silicates and Aluminosilicates*, J. Electrochem. Soc, **1976**, 123, Vol. 10

[26]   U. Voigt, H. Lammert, H. Eckert, A. Heuer, *Cation clustering in lithium silicate glasses: Quantitative description by solid-state NMR and molecular dynamics simulations, Phys. Rev.* B, **2005**, 72, 064207

[27]   B. Mysen, *Physics and chemistry of silicate glasses and melts*, Eur. J. Mineral, **2003**, 15, 781-802

[28]   B. Mysen, D. Virgo, F. Seifert, *Relationships between properties and structure of alumosilicate melts*, American Mineralogist, **1985**, 70, 88 - 105

[29]   A. M. Hofmeister, A. G. Whittington, *Transport properties of high albite crystals, near-endmember feldspar and pyroxene glasses, and their melts to high temperature*, **2009**, Contrib Mineral Petrol, 158, 381-400

4. References

[30] W. Löwenstein, *The Distribution of Aluminium in the Tetrahedra of Silicates and Aluminates*. Am. Mineral., **1954**, 39, 92−96.

[31] S. K. Lee, J. F. Stebbins, *Al-O-Al and Si-O-Si sites in framework alumosilicates glasses with Si/Al =1: quantification of framework disorder, Journal of Non-Crystalline Solids*, **2000**, 270, 260-264

[32] Z. Xu, F. Stebbins, *^6Li nuclear magnetic resonance chemical shifts, coordination number and relaxation in crystalline and glassy silicates*, Solid State Nuclear Magnetic Resonance, **1995**, 5, 103-112

[33] A.-M. Welsch, H. Behrens, S. Ross, D. Murawski*, , Structural Control of Ionic Conductivity in $LiAlSi_2O_6$ and $LiAlSi_4O_{10}$ Glasses and single Crystals,* Z. Phys. Chem., **2012**, 226, 491

[34] J. R. MacDonald, *Impedance Spectroscopy and its use in Analzing the Steady-State AC Response of Solid and Liquid Electrolytes*, J. Electroanal. Chem., **1987**, 223, 25-50

[35] G. Wedler, *Lehrbuch der physikalischen Chemie*, **1987**, published by VCH Weinheim, 3rd Edition

[36] M. E. Orazem, B. Tribollet, *Electrochemical Impedance Spectroscopy*, **2008**, published at John Wiley & Sons, Inc., 342 ff.

[37] L. Nasdala, D. C. Smith, R. Kaindl, M. A. Ziemann, *Raman spectroscopy: Analytcal perspectives in mineralogical research*, **2004**, EMU Notes in Mineralogy, Vol. 6, Chapter 7

[38] D. L. Rousseau, R. P. Bauman, S. P. S. Porto, *Normal Mode Determination in Crystas*, **1981**, Journal of Raman Spectroscopy, 10, 253-290

[39] D. A. Long, *The Raman effect*, **2002**, John Wiley and Sons Ltd, New York

[40] M. Hass, *Temperature Dependence of the Raman Spectrum of Vitreous Silica*, Solid State Communications, **1969**, 7, 1069-1071

[41] R. Shuker, R. Gammon, *Raman-Scattering Selection-Rule Breaking and the Density of States in Amorphous Materials*, Physical Review Letters, **1970**, 25, 222-225

[42] J. L. Pochou, F. Pichoir: *Electron Probe Quantitation*, Plenum Press Div Plenum Publishing Corp, New York, **1991**, 31

[43] HVG-DGG. http://www.hvg-dgg.de/download/freie-inhalte/standardglas.html (**2013**)

4. References

[44]   R. T. Johnson, R. M. Biefeld, M. L. Knotek, B. Morosin, *Ionic conductivity in Solid Electrolytes Based in Lithium Alumosilicate Glass and Glass-Ceramic*, J. Electrochem. Soc., **1976**, 123, 5, 680 - 687

[45]   P. Maass, A. Bunde, M. D. Ingram, *Ion Transport Anomalies in Glasses*, Physical Review Letters, **1992**, 68-20, 3064-3067

[46]   B. Roling, A. Happe, M. D. Ingram, K. Funke, *Interrelation between Different Mixed Cation Effects in the Electrical Conductivity and Mechanical Loss Spectra of Ion Conducting Glasses*, J. Phys. Chem. B, **1999**, 103, 4122-4127

[47]   M. Tomozawa, *Alkali ionic transport in mixed alkali glasses*, J. of Non-Crystalline Solids, **1993**, 152, 59-69

[48]   C. A. Angell, *Diffusion-Conductance Relations and Free Volume in Molten Salts*, The Journal of Physical Chemistry, **1965**, 69-2, 399-403

[49]   J. L. Souquet, *Ionic Transport in Amorphous Solid Electrolytes*, Ann. Rev. Mater. Sci., **1981**, 11, 211-231

[50]   B. Mysen, D. Virgo, I. Kushiro, *The structural role of aluminum in silicate melts – a Raman spectroscopic study at 1 atm*, Am. Mineral, **1981**, 66, 678-701

[51]   P. McMillan and B. Piriou, *The structures and vibrational spectra of crystals and glasses in the silica-alumina system*, J. Non-Crystalline Solids, **1982,** 53, 279-298

[52]   P. McMillan, *Structural studies of silicate glasses and melts - applications and limitatons of Raman spectroscopy*, American Mineralogist, **1984**, 69, 622-644

[53]   O. L. Anderson, D. A. Stuart, *Calculation of Activation Energy of Ionic Conductivity in Silica Glasses by Classical Methods* J. Amer. Ceram. Soc., **1954**, 37, 573-580

[54]   D. Ravaine, J. L. Souquet, Phys. Chem. Glasses, **1977**, 18, 27 ff.

[55]   M. D. Ingram, *Ionic conductivity and the weak electrolyte theory of glass*, J. Non-Cryst. Sol., **1980**, 38-39, 371-376

[56]   G. N. Greaves, S. J. Gurman, C. R. A. Catlow, A. V. Chadwick, S. Houde-Walter, C. M. B. Henderson, B. R. Dobson, *A structural basis for ionic diffusion in oxide glasses*, Philosophical Magazine A, **1991**, 64-5, 1059-1072

[57]   K. Funke, *Ion transport in fast ion conductors - spectra and models*, Solid State Ionics, **1997** , 94, 27-33

[58]   A. Bunde, M. D. Ingram, P. Maass, K. L. Ngai, *Diffusion with memory: a model for mixed alkali effects in vitreous ionic conductors*, J. Phys. A: Math. Gen., **1991**, 24, L881-L886

4. References

[59]   S. Chakraborty, *Diffusion in silicate melts*, Rev. Mineral. Geochim., **1995**, 32, 411-503

[60]   K. Funke, B. Roling, M. Lange, *Dynamic of mobile ions in crystals, glasses and melts*, Solid State Ionics, **1998**, 105, 195-208

[61]   K. Funke, R. D. Banhatti, D. M. Laughman, L. G. Badr, M. Mutke, A. Santic, W. Wrobel, E. M. Fellberg , C. Biermann, *First and Second Universalities: Expeditions Towards and Beyond*. Z. Phys. Chem., **2010**, 224, 1891–1950

[62]   K. Funke, T. Lauxtermann, D. Wilmer, S. M. Bennington, *Creation and Recombination of Frenkel Defects in AgBr*, Z. Naturforsch., **1995**, 50a, 509 ff.

[63]   B. Roling, *Scaling properties of the conductivity spectra of glasses and supercooled melts*, Solid State Ionics, **1998**, 105, 185-193.

[64]   J. C. Dyre, *The random free-energy barrier model for ac conduction in disordered solids*, Appl. Phys., **1988**, 64**,** 2456 ff.

[65]   H. Jain, *"Jellyfish" Atom Movement in Inorganic Glasses*, Metals Mater. Process., **1999**, 11**,** 317.

[66]   H. Kahnt, *Ionic Transport in Oxide Glasses and Frequency Dependence of Conductivity*, Ber. Bunsenges. Phys. Chem., **1991**, 95, 1021 ff.

[67]   H. Kahnt, *Ionic transport in glasses*, Journal of Non-Crystalline Solids, **1996**, 203, 225-231

[68]   S. K. Lee, J. F. Stebbins, *Effects of the Degree of Polymerization on the Structure of Sodium Silicate and Aluminosilicate Glasses and Melts: An ^{17}O NMR Study*, Geochim. Cosmochim. Acta, **2009**, 73, 1109−1119.

[69]   H. Uhlig, M. J. Hoffmann, H.-P.Lamparter, F. Aldringer, R. Bellissent, S. S. Steeb, *Short-Range and Medium-Range Order in Lithium Silicate Glasses, Part I: Diffraction Experiments and Results*, J. Am. Ceram. Soc., **1996**, 79, 2833−2838.

[70]   E. Göbel, W. Müller-Warmuth, H. Olyschläger, H. Dutz, *^{7}Li-NMR-Spectra, Nuclear-Relaxation, and Lithium Ion Motion in Alkali Silicate, Borate, and Phospate-Glasses*, J. Magn. Reson., **1979**, 36, 371−387.

[71]   S. Sen, T. A. Mukerji, *Molecular Dynamics Simulation Study of Ionic Diffusion and NMR Spin-Lattice Relaxation in Li2Si4O9 Glass*, J. Non-Cryst. Solids, **2001**, 293−295, 268−278.

[72]   J. Du, L. R. Corrales, *Structure, Dynamics, and Electronic Properties of Lithium Disilicate Melt and Glass*. J. Chem. Phys. **2006**, 125, 114702/1−114702/12.

4. References

[73] H. Lammert, A. Heuer, *Emergence of Conduction Channels in Lithium Silicate*, Phys. Rev. B, **2004**, 70, 024204/1−024204/5.

[74] J. Habasaki, Y. Hiwatari, *Molecular Dynamics Study of the Mechanism of Ion Transport in Lithium Silicate Glasses: Characteristics of the Potential Energy Surface and Structures*, Phys. Rev. B 2004, 69, 144207/1−144207/17.

[75] R. Prasada Rao, T. D. Tho, S. Adams, *Ion Transport Pathways in Molecular Dynamics Simulated Lithium Silicate Glasses*, Solid State Ionics, **2010**, 181, 1−6.

[76] J. Zhao, P. H. Gaskell, M. M. Cluckie, A. K. Soper, *A Neutron Diffraction, Isotopic Substitution Study of the Structure of $Li_2O \cdot 2\,SiO_2 Glass$,* J. Non-Cryst. Solids, **1998**, 232−234, 721−727.

[77] A. C. Hannon, B. Vessal, J. M. Park, *The Structure of Alkali Silicate-Glasses*, J. Non-Cryst. Solids, **1992**, 150, 97−102.

[78] F. Kargl, A. Meyer, M. M. Koza, H. Schober, *Formation of Channels for Fast-Ion Diffusion in Alkali Silicate Melts: A Quasielastic Neutron Scattering Study*, Phys. Rev. B, **2006**, 74, 014304/1−014304/5.

[79] P. Mondal, A. Klein, W. Jaegermann, H. Hahn, *Enhanced specific grain boundary conductivity in nanocrystalline Y_2O_3-stabilized zirconia*, Solid State Ionics, **1999**, 118, 331-339

[80] K. L. Nagy, B. J. Giletti, *Grain diffusion of oxygen in a macroperthitic feldspar*, Geochimica et Cosmochimica Acta, **1986**, 50, 1151-1158

[81] P. Scarlato, B. T. Poe, C. Freda, *High-pressure and high-temperature measurements of electrical conductivity in basaltic rocks from Mount Etna, Sicily, Italy*, Journal of Geophysical Research, **2004**, 109, B02210

[82] J. H. Ter Heege, J. Renner, *In situ impedance spectroscopy on pyrophyllite and $CaCO_3$ at high pressure and temperature: phase transformations and kinetics of atomistic transport*, Phys. Chem. Minerals, **2007**, 34, 445-465

[83] R. Hinrichs, J. A. H. da Jornada, *Piston-cylinder apparatus for high-pressure impedance spectroscopy*, Review of Scientific Instruments, **1997**, 68, 193-196

[84] N. Bagdassarov, H.-C. Freiheit, A. Putnis, *Ionic conductivity and pressure dependence of trigonal-to-cubic phase transition in lithium sodium sulphate*, Solid State Ionics, **2001**, 285-296

[85] http://imagej.nih.gov/ij, Homepage of the national institute of Health, Last modified 17. November **2004**

4. References

[86]   N. Bagdassarov, J. Maumus, B. Poe, A. Slutskiy, V. Bulatov, *Pressure dependence of T_g in silicate glasses from electrical impedance measurements*, Phys. Chem. Glasses, 45(3), **2004**, 197-214

[87]   C. Roland, S. Hensel-Bielowka, M. Paluch, R. Casalini, *Supercooled dynamics of glass-forming liquids and polymers under hydrostatic pressure*, Reports on Progress in Physics, 68, **2005**, 1405-1478

[88]   G. Frenzer, W. F. Maier, *Amorphous Porous Mixed Oxides: Sol-Gel Ways to a Highly Versatile Class of Materials and Catalysts*, Annu. Rev. Mater. Res., **2006**, 36, 281-331

[89]   J. Kane, H. P. Schweizer, W. Kern, *Chemical Vapor Deposition of Transparent, Electrically Conductive Tin Oxide Films Formed from Dibutyl Tin Diacetate*, J. Electrochem. Soc.: Solid-State Science and Technology, **1975**, 122, No. 8, 1144-1149

[90]   G. Lucovsky, P. D. Richard, D. V. Tsu, S. Y. Lin, R. J, Markunas, *Deposition of silicon dioxide and silicon nitride by remote plasma enhanced chemical vapor deposition*, Journal of Vacuum Science and Technology A, **1986**, 4, 681-688

[91]   S. Veprek, J. Weidmann, F. Glatz, *Plasma chemical vapor depostition and properties of hard C3N4 thin films*, Journal of Vacuum Science and Technology A, **1995**, 13, 2914-2919

[92]   V.V. Srdic, M. Winterer, H. Hahn, *Sintering Behavior of Nanocrystalline Zirconia Prepared by Chemical Vapor Synthesis*, J. Am. Ceram. Soc., **2000**, 83, 729-736

[93]   K.-Th. Wilke, J. Bohm, *Kristallzüchtung*, Harri Deutsch, Thun; Frankfurt/Main, 1**988**.

[94]   Jürg Hulliger, *Chemistry and Crystal growth*, Angew. Chem. Int. Ed. Engl., **1994**, 33, 143-162

[95]   C. Brünig, Gasphasensynthese oxidischer Lithiumionenleiter, Dissertation at University of Hanover, 2010

[96]   J. Strähle, E. Schweda, *Jander/Blasius. Einführung in das anorganisch-chemische Praktikum*, 14. edition, **1995**, published by S. Hirzel Verlag GmbH & Co.

[97]   C. P. Schlichter, *Principles of Magnetic resonance*, **1990**, published by Springer

[98]   M. Wilkening, A. Kuhn, P. Heitjans, *Atomic-scale measurement of ultraslow Li motions in glassy LiAlSi2O6 by two-time 6Li spin-alihgnment echo NMR correlation spectroscopy*, Physical Review B, **2008**, 78, 0,543031-9

4. References

[99] A. Kuhn, S. Narayanan, L. Spencer, G. Goward, V. Thangadurai, M. Wilkening, *Li self-diffusion in garnet-type $Li_7La_3Zr_2O_{12}$ as probed directly by diffusion-induced ^7Li spin-lattice relaxation NMR spectroscopy*, Physical Review B, **2011**, 83

[100] J. R. Hendrickson, P. J. Bray, *A Phenomenological Equation for NMR Motional Narrowing in Solids*, Journal of Magnetic Resonance, **1973**, 9, 341-357

[101] K. S. Cole, R. H. Cole, *Dispersion and Absorption in Dielectrics - II. Direct Current Characteristics*, Journal of Chemical Physics**, 1942**, 10, 98-105

5. Appendix

5.A Impedance spectroscopy data derived from IS spectra for sample EUC

Sample EUC, LiAlSiO$_4$ c(Li) / #Li / m^3 =   1.16E+28

T	1000/T	σ_{dc}	$\log(\sigma_{DC,spez.} * T)$	D_{dc}	$\log(D_{dc})$
K	K^{-1}	S/m	$\log(/ SKm^{-1})$	m^2 s^{-1}	$\log(m^2 s^{-1})$
297.9	3.3563	1.62E-07	-4.32	2.24E-18	-17.65
306.0	3.2680	3.24E-07	-4.00	4.59E-18	-17.34
318.1	3.1436	7.79E-07	-3.61	1.15E-17	-16.94
331.1	3.0204	1.91E-06	-3.20	2.92E-17	-16.53
344.3	2.9041	4.63E-06	-2.80	7.39E-17	-16.13
357.9	2.7939	1.08E-05	-2.41	1.79E-16	-15.75
371.8	2.6895	2.33E-05	-2.06	4.01E-16	-15.40
384.5	2.6006	4.65E-05	-1.75	8.28E-16	-15.08
396.3	2.5235	8.73E-05	-1.46	1.60E-15	-14.79
408.3	2.4489	1.56E-04	-1.20	2.95E-15	-14.53
420.9	2.3761	2.74E-04	-0.94	5.34E-15	-14.27
433.3	2.3080	4.63E-04	-0.70	9.30E-15	-14.03
445.3	2.2455	7.53E-04	-0.47	1.55E-14	-13.81
457.0	2.1882	1.18E-03	-0.27	2.49E-14	-13.60
468.3	2.1354	1.78E-03	-0.08	3.86E-14	-13.41
480.3	2.0820	2.64E-03	0.10	5.88E-14	-13.23
491.5	2.0345	3.86E-03	0.28	8.79E-14	-13.06
502.1	1.9914	5.52E-03	0.44	1.29E-13	-12.89
513.1	1.9488	7.74E-03	0.60	1.84E-13	-12.74
523.9	1.9088	1.06E-02	0.74	2.56E-13	-12.59
534.4	1.8711	1.42E-02	0.88	3.51E-13	-12.46
545.2	1.8343	1.89E-02	1.01	4.78E-13	-12.32
556.4	1.7972	2.48E-02	1.14	6.39E-13	-12.19
566.8	1.7642	3.21E-02	1.26	8.44E-13	-12.07
576.7	1.7339	4.11E-02	1.37	1.10E-12	-11.96
587.0	1.7035	5.16E-02	1.48	1.40E-12	-11.85
597.4	1.6739	6.41E-02	1.58	1.77E-12	-11.75

5. Appendix

5.B Impedance spectroscopy data derived from IS spectra for sample SPO

Sample SPO, LiAlSi$_2$O$_6$ c(Li) / #Li / m^3 = 7.68E+27

T	1000/T	σ_{dc}	$\log(\sigma_{DC,spez.} * T)$	D_{dc}	$\log(D_{dc})$
K	K^{-1}	S/m	log(/ SKm^{-1})	m^2 s^{-1}	log(m^2 s^{-1})
299.3	3.3410	9.17E-08	-4.56	1.92E-18	-17.72
308.5	3.2411	1.82E-07	-4.25	3.94E-18	-17.40
320.5	3.1198	4.63E-07	-3.83	1.04E-17	-16.98
333.0	3.0034	1.16E-06	-3.41	2.72E-17	-16.57
345.7	2.8926	2.84E-06	-3.01	6.89E-17	-16.16
358.7	2.7881	6.55E-06	-2.63	1.65E-16	-15.78
371.3	2.6933	1.39E-05	-2.29	3.62E-16	-15.44
384.1	2.6032	2.73E-05	-1.98	7.34E-16	-15.13
395.4	2.5291	5.04E-05	-1.70	1.40E-15	-14.86
406.7	2.4586	8.88E-05	-1.44	2.53E-15	-14.60
418.6	2.3887	1.54E-04	-1.19	4.51E-15	-14.35
430.6	2.3224	2.59E-04	-0.95	7.80E-15	-14.11
442.1	2.2617	4.18E-04	-0.73	1.29E-14	-13.89
453.4	2.2054	6.52E-04	-0.53	2.07E-14	-13.68
464.3	2.1536	9.82E-04	-0.34	3.19E-14	-13.50
475.0	2.1052	1.44E-03	-0.16	4.80E-14	-13.32
485.9	2.0581	2.10E-03	0.01	7.14E-14	-13.15
497.2	2.0111	2.99E-03	0.17	1.04E-13	-12.98
507.7	1.9696	4.17E-03	0.33	1.48E-13	-12.83
517.6	1.9321	5.72E-03	0.47	2.07E-13	-12.68
527.8	1.8948	7.70E-03	0.61	2.85E-13	-12.55
537.9	1.8591	1.02E-02	0.74	3.85E-13	-12.41
548.1	1.8243	1.35E-02	0.87	5.17E-13	-12.29
558.3	1.7911	1.75E-02	0.99	6.83E-13	-12.17
568.3	1.7596	2.23E-02	1.10	8.90E-13	-12.05
578.3	1.7293	2.82E-02	1.21	1.14E-12	-11.94
588.1	1.7003	3.52E-02	1.32	1.45E-12	-11.84
598.1	1.6719	4.35E-02	1.42	1.82E-12	-11.74
608.9	1.6424	5.36E-02	1.51	2.29E-12	-11.64
618.2	1.6175	6.53E-02	1.61	2.83E-12	-11.55
628.1	1.5921	7.92E-02	1.70	3.48E-12	-11.46
638.0	1.5674	9.52E-02	1.78	4.26E-12	-11.37
647.9	1.5434	1.13E-01	1.86	5.13E-12	-11.29
657.9	1.5201	1.36E-01	1.95	6.25E-12	-11.20
667.9	1.4972	1.60E-01	2.03	7.49E-12	-11.13
678.0	1.4750	1.89E-01	2.11	8.96E-12	-11.05
688.5	1.4525	2.23E-01	2.19	1.08E-11	-10.97
695.7	1.4375	2.47E-01	2.23	1.20E-11	-10.92
696.7	1.4354	2.50E-01	2.24	1.22E-11	-10.91
696.6	1.4356	2.46E-01	2.23	1.20E-11	-10.92
696.4	1.4361	2.39E-01	2.22	1.17E-11	-10.93
696.2	1.4365	2.36E-01	2.21	1.15E-11	-10.94
693.6	1.4418	2.23E-01	2.19	1.08E-11	-10.96

5. Appendix

5.C Impedance spectroscopy data derived from IS spectra for sample FSP

Sample FSP, LiAlSi$_3$O$_8$ $c(Li) / \#Li / m^3 =$ 5.66E+27

T	1000/T	σ_{dc}	$\log(\sigma_{DC,spez.} * T)$	D_{dc}	$\log(D_{dc})$
K	K^{-1}	S/m	$\log(/ SKm^{-1})$	m^2 s^{-1}	$\log(m^2 s^{-1})$
303.2	3.2985	8.61E-08	-4.58	2.48E-18	-17.61
316.9	3.1556	2.51E-07	-4.10	7.56E-18	-17.12
334.3	2.9917	9.80E-07	-3.48	3.11E-17	-16.51
354.1	2.8242	3.83E-06	-2.87	1.29E-16	-15.89
373.7	2.6759	1.27E-05	-2.33	4.49E-16	-15.35
392.3	2.5488	3.49E-05	-1.86	1.30E-15	-14.89
410.4	2.4369	8.47E-05	-1.46	3.30E-15	-14.48
428.4	2.3344	1.90E-04	-1.09	7.74E-15	-14.11
445.9	2.2429	3.93E-04	-0.76	1.66E-14	-13.78
462.6	2.1616	7.51E-04	-0.46	3.30E-14	-13.48
479.1	2.0873	1.36E-03	-0.19	6.18E-14	-13.21
496.2	2.0153	2.35E-03	0.07	1.11E-13	-12.96
511.5	1.9551	3.88E-03	0.30	1.89E-13	-12.72
525.5	1.9028	5.94E-03	0.49	2.97E-13	-12.53
531.5	1.8814	7.05E-03	0.57	3.56E-13	-12.45
532.4	1.8784	7.22E-03	0.58	3.65E-13	-12.44
529.5	1.8887	6.63E-03	0.55	3.34E-13	-12.48
522.9	1.9125	5.46E-03	0.46	2.71E-13	-12.57
515.2	1.9412	4.32E-03	0.35	2.12E-13	-12.67
507.4	1.9710	3.37E-03	0.23	1.63E-13	-12.79
500.0	1.9999	2.61E-03	0.12	1.24E-13	-12.91
491.4	2.0350	2.01E-03	-0.01	9.39E-14	-13.03
483.3	2.0690	1.53E-03	-0.13	7.05E-14	-13.15
476.0	2.1009	1.16E-03	-0.26	5.23E-14	-13.28
467.9	2.1370	8.74E-04	-0.39	3.88E-14	-13.41
459.8	2.1746	6.52E-04	-0.52	2.85E-14	-13.55
452.1	2.2119	4.83E-04	-0.66	2.08E-14	-13.68
444.2	2.2511	3.51E-04	-0.81	1.48E-14	-13.83
436.2	2.2926	2.51E-04	-0.96	1.04E-14	-13.98
428.0	2.3366	1.75E-04	-1.12	7.13E-15	-14.15
419.5	2.3838	1.20E-04	-1.30	4.80E-15	-14.32
410.9	2.4335	8.05E-05	-1.48	3.15E-15	-14.50
402.6	2.4836	5.37E-05	-1.66	2.06E-15	-14.69
394.4	2.5356	3.55E-05	-1.85	1.33E-15	-14.88
386.5	2.5875	2.33E-05	-2.05	8.56E-16	-15.07
381.6	2.6204	1.79E-05	-2.17	6.49E-16	-15.19
380.6	2.6273	1.63E-05	-2.21	5.91E-16	-15.23
383.7	2.6060	2.07E-05	-2.10	7.56E-16	-15.12
393.2	2.5434	3.47E-05	-1.87	1.30E-15	-14.89

5. Appendix

T	1000/T	σ_{dc}	$\log(\sigma_{DC,spez.} * T)$	D_{dc}	$\log(D_{dc})$
404.8	2.4703	6.24E-05	-1.60	2.40E-15	-14.62
417.2	2.3971	1.11E-04	-1.33	4.41E-15	-14.36
429.5	2.3285	1.92E-04	-1.08	7.82E-15	-14.11
441.3	2.2659	3.16E-04	-0.86	1.33E-14	-13.88
452.7	2.2091	4.98E-04	-0.65	2.14E-14	-13.67
463.6	2.1572	7.55E-04	-0.46	3.33E-14	-13.48
474.3	2.1084	1.12E-03	-0.27	5.05E-14	-13.30
485.1	2.0613	1.64E-03	-0.10	7.54E-14	-13.12
495.8	2.0171	2.33E-03	0.06	1.10E-13	-12.96
507.0	1.9726	3.27E-03	0.22	1.57E-13	-12.80
516.6	1.9356	4.47E-03	0.36	2.19E-13	-12.66
525.8	1.9020	5.91E-03	0.49	2.95E-13	-12.53
530.6	1.8846	6.81E-03	0.56	3.44E-13	-12.46
531.7	1.8809	7.00E-03	0.57	3.54E-13	-12.45
529.9	1.8873	6.65E-03	0.55	3.35E-13	-12.47
523.9	1.9089	5.58E-03	0.47	2.78E-13	-12.56
516.3	1.9368	4.43E-03	0.36	2.18E-13	-12.66
508.4	1.9669	3.48E-03	0.25	1.68E-13	-12.77
500.4	1.9986	2.69E-03	0.13	1.28E-13	-12.89
493.1	2.0282	2.06E-03	0.01	9.66E-14	-13.02
484.6	2.0637	1.57E-03	-0.12	7.21E-14	-13.14
476.1	2.1005	1.18E-03	-0.25	5.34E-14	-13.27
468.2	2.1359	8.85E-04	-0.38	3.94E-14	-13.40
460.3	2.1724	6.59E-04	-0.52	2.88E-14	-13.54
452.4	2.2105	4.84E-04	-0.66	2.08E-14	-13.68
444.4	2.2504	3.49E-04	-0.81	1.48E-14	-13.83
436.1	2.2929	2.48E-04	-0.97	1.03E-14	-13.99
427.7	2.3383	1.71E-04	-1.14	6.96E-15	-14.16
419.5	2.3839	1.17E-04	-1.31	4.65E-15	-14.33
411.0	2.4330	7.74E-05	-1.50	3.02E-15	-14.52
401.8	2.4885	5.13E-05	-1.69	1.96E-15	-14.71
393.4	2.5416	3.35E-05	-1.88	1.25E-15	-14.90
385.2	2.5958	2.14E-05	-2.08	7.82E-16	-15.11
377.3	2.6505	1.37E-05	-2.29	4.93E-16	-15.31
369.8	2.7040	8.75E-06	-2.49	3.07E-16	-15.51
362.9	2.7553	5.72E-06	-2.68	1.97E-16	-15.70
357.2	2.7992	3.90E-06	-2.86	1.32E-16	-15.88
351.4	2.8455	2.70E-06	-3.02	9.03E-17	-16.04
345.7	2.8930	1.89E-06	-3.19	6.19E-17	-16.21
340.9	2.9337	1.37E-06	-3.33	4.43E-17	-16.35
336.6	2.9705	1.02E-06	-3.46	3.26E-17	-16.49
332.8	3.0044	7.70E-07	-3.59	2.43E-17	-16.61

5. Appendix

5.D Impedance spectroscopy data derived from IS spectra for sample PET

Sample PET, LiAlSi$_4$O$_{10}$ c(Li) / #Li / m^3 =   4.52E+27

T	1000/T	σ_{dc}	log($\sigma_{DC,spez.}$ * T)	D_{dc}	log(D_{dc})
K	K^{-1}	S/m	log(/ SKm^{-1})	m^2 s^{-1}	log(m^2 s^{-1})
307.0	3.2578	4.35E-08	-4.87	1.59E-18	-17.80
313.7	3.1878	8.02E-08	-4.60	2.99E-18	-17.52
323.5	3.0916	1.74E-07	-4.25	6.68E-18	-17.18
334.3	2.9913	3.78E-07	-3.90	1.50E-17	-16.82
345.2	2.8968	8.07E-07	-3.55	3.31E-17	-16.48
355.4	2.8135	1.68E-06	-3.22	7.11E-17	-16.15
366.0	2.7324	3.31E-06	-2.92	1.44E-16	-15.84
376.9	2.6531	6.13E-06	-2.64	2.75E-16	-15.56
387.2	2.5824	1.07E-05	-2.38	4.94E-16	-15.31
396.2	2.5237	1.79E-05	-2.15	8.44E-16	-15.07
405.5	2.4662	2.89E-05	-1.93	1.40E-15	-14.86
415.2	2.4086	4.62E-05	-1.72	2.28E-15	-14.64
425.0	2.3530	7.23E-05	-1.51	3.65E-15	-14.44
435.0	2.2989	1.10E-04	-1.32	5.71E-15	-14.24
444.7	2.2488	1.64E-04	-1.14	8.66E-15	-14.06
453.4	2.2055	2.37E-04	-0.97	1.28E-14	-13.89
462.0	2.1646	3.37E-04	-0.81	1.85E-14	-13.73
470.7	2.1246	4.69E-04	-0.66	2.63E-14	-13.58
479.5	2.0857	6.46E-04	-0.51	3.68E-14	-13.43
488.3	2.0481	8.79E-04	-0.37	5.10E-14	-13.29
497.2	2.0111	1.18E-03	-0.23	6.98E-14	-13.16
506.4	1.9749	1.56E-03	-0.10	9.40E-14	-13.03
514.1	1.9452	2.03E-03	0.02	1.24E-13	-12.91
522.2	1.9148	2.63E-03	0.14	1.63E-13	-12.79
530.4	1.8853	3.35E-03	0.25	2.11E-13	-12.68
538.6	1.8568	4.22E-03	0.36	2.70E-13	-12.57
547.1	1.8279	5.30E-03	0.46	3.44E-13	-12.46
555.7	1.7994	6.60E-03	0.56	4.36E-13	-12.36
563.4	1.7750	8.16E-03	0.66	5.46E-13	-12.26
571.3	1.7505	9.99E-03	0.76	6.78E-13	-12.17
579.3	1.7262	1.21E-02	0.85	8.34E-13	-12.08
587.3	1.7028	1.46E-02	0.93	1.02E-12	-11.99
595.2	1.6801	1.75E-02	1.02	1.24E-12	-11.91
604.0	1.6557	2.08E-02	1.10	1.50E-12	-11.83
611.6	1.6351	2.47E-02	1.18	1.80E-12	-11.75
619.0	1.6154	2.91E-02	1.26	2.14E-12	-11.67
623.7	1.6034	3.19E-02	1.30	2.37E-12	-11.63
624.7	1.6009	3.22E-02	1.30	2.39E-12	-11.62
624.5	1.6013	3.19E-02	1.30	2.37E-12	-11.63
625.1	1.5999	3.16E-02	1.30	2.35E-12	-11.63
624.4	1.6014	3.12E-02	1.29	2.32E-12	-11.63
620.8	1.6108	2.93E-02	1.26	2.17E-12	-11.66
613.6	1.6298	2.50E-02	1.19	1.82E-12	-11.74

5. Appendix

T	1000/T	σ_{dc}	$\log(\sigma_{DC,spez.} * T)$	D_{dc}	$\log(D_{dc})$
605.4	1.6519	2.09E-02	1.10	1.50E-12	-11.82
597.1	1.6748	1.72E-02	1.01	1.22E-12	-11.91
589.4	1.6966	1.41E-02	0.92	9.90E-13	-12.00
581.7	1.7191	1.17E-02	0.83	8.06E-13	-12.09
573.1	1.7448	9.54E-03	0.74	6.50E-13	-12.19
565.0	1.7698	7.81E-03	0.64	5.25E-13	-12.28
557.0	1.7955	6.30E-03	0.54	4.17E-13	-12.38
548.9	1.8219	5.04E-03	0.44	3.29E-13	-12.48
540.8	1.8492	3.99E-03	0.33	2.57E-13	-12.59
533.4	1.8749	3.17E-03	0.23	2.01E-13	-12.70
525.2	1.9039	2.50E-03	0.12	1.56E-13	-12.81
516.7	1.9353	1.94E-03	0.00	1.19E-13	-12.92
508.5	1.9664	1.51E-03	-0.12	9.10E-14	-13.04
500.3	1.9988	1.15E-03	-0.24	6.81E-14	-13.17
492.0	2.0326	8.56E-04	-0.38	5.01E-14	-13.30
483.5	2.0685	6.35E-04	-0.51	3.65E-14	-13.44
475.7	2.1022	4.62E-04	-0.66	2.61E-14	-13.58
467.0	2.1415	3.35E-04	-0.81	1.86E-14	-13.73
458.0	2.1833	2.39E-04	-0.96	1.30E-14	-13.89
449.4	2.2253	1.69E-04	-1.12	9.04E-15	-14.04
440.7	2.2691	1.16E-04	-1.29	6.09E-15	-14.22
431.8	2.3157	7.86E-05	-1.47	4.03E-15	-14.39
422.8	2.3653	5.14E-05	-1.66	2.58E-15	-14.59
413.9	2.4158	3.27E-05	-1.87	1.61E-15	-14.79
404.2	2.4741	2.08E-05	-2.08	9.98E-16	-15.00
395.1	2.5312	1.30E-05	-2.29	6.08E-16	-15.22
386.4	2.5882	8.01E-06	-2.51	3.68E-16	-15.43
378.2	2.6443	5.01E-06	-2.72	2.25E-16	-15.65
370.6	2.6984	3.16E-06	-2.93	1.39E-16	-15.86
363.7	2.7495	2.00E-06	-3.14	8.67E-17	-16.06
358.0	2.7930	1.36E-06	-3.31	5.81E-17	-16.24
352.2	2.8389	9.38E-07	-3.48	3.93E-17	-16.41
346.4	2.8869	6.54E-07	-3.64	2.69E-17	-16.57
341.6	2.9278	4.73E-07	-3.79	1.92E-17	-16.72
337.3	2.9648	3.51E-07	-3.93	1.41E-17	-16.85
333.5	2.9984	2.67E-07	-4.05	1.06E-17	-16.98

5. Appendix

5.E   Impedance spectroscopy data derived from IS spectra for sample DG1

Sample DG1 $c(Li) / \#Li / m^3 = $ 1.08E+28

T	1000/T	σ_{dc}	$\log(\sigma_{DC,spez.} * T)$	D_{dc}	$\log(D_{dc})$
K	K^{-1}	S/m	$\log(/ SKm^{-1})$	$m^2 s^{-1}$	$\log(m^2 s^{-1})$
328.3	3.0457	6.99E-08	-4.64	1.14E-18	-17.94
340.0	2.9409	1.70E-07	-4.24	2.87E-18	-17.54
352.4	2.8379	4.05E-07	-3.85	7.10E-18	-17.15
365.0	2.7399	9.06E-07	-3.48	1.64E-17	-16.78
377.1	2.6519	1.87E-06	-3.15	3.51E-17	-16.46
388.2	2.5757	3.63E-06	-2.85	7.00E-17	-16.15
398.8	2.5077	6.65E-06	-2.58	1.32E-16	-15.88
409.6	2.4415	1.17E-05	-2.32	2.39E-16	-15.62
420.8	2.3766	2.03E-05	-2.07	4.25E-16	-15.37
432.5	2.3121	3.43E-05	-1.83	7.36E-16	-15.13
443.3	2.2556	5.59E-05	-1.61	1.23E-15	-14.91
453.2	2.2064	8.81E-05	-1.40	1.98E-15	-14.70
463.8	2.1562	1.35E-04	-1.20	3.11E-15	-14.51
473.8	2.1107	2.01E-04	-1.02	4.73E-15	-14.33
483.4	2.0687	2.98E-04	-0.84	7.16E-15	-14.15
493.5	2.0265	4.37E-04	-0.67	1.07E-14	-13.97
503.4	1.9866	6.23E-04	-0.50	1.56E-14	-13.81
513.6	1.9469	8.68E-04	-0.35	2.22E-14	-13.65
523.2	1.9112	1.19E-03	-0.21	3.08E-14	-13.51
532.1	1.8793	1.60E-03	-0.07	4.23E-14	-13.37
541.2	1.8476	2.14E-03	0.06	5.75E-14	-13.24
550.6	1.8161	2.83E-03	0.19	7.75E-14	-13.11
560.0	1.7856	3.65E-03	0.31	1.02E-13	-12.99
569.9	1.7548	4.76E-03	0.43	1.35E-13	-12.87
578.9	1.7273	6.05E-03	0.54	1.74E-13	-12.76
587.6	1.7019	7.66E-03	0.65	2.24E-13	-12.65
596.6	1.6761	9.68E-03	0.76	2.87E-13	-12.54
605.9	1.6505	1.19E-02	0.86	3.57E-13	-12.45
624.2	1.6022	1.75E-02	1.04	5.42E-13	-12.27
624.2	1.6022	1.67E-02	1.02	5.18E-13	-12.29
597.3	1.6741	9.04E-03	0.73	2.69E-13	-12.57
572.8	1.7457	4.68E-03	0.43	1.33E-13	-12.88
549.9	1.8186	2.44E-03	0.13	6.66E-14	-13.18
528.8	1.8912	1.26E-03	-0.18	3.31E-14	-13.48
510.0	1.9609	6.52E-04	-0.48	1.65E-14	-13.78
492.0	2.0327	3.40E-04	-0.78	8.31E-15	-14.08
474.7	2.1065	1.78E-04	-1.07	4.19E-15	-14.38
459.2	2.1778	9.40E-05	-1.36	2.15E-15	-14.67
445.0	2.2471	5.12E-05	-1.64	1.13E-15	-14.95
431.9	2.3153	2.79E-05	-1.92	6.00E-16	-15.22
420.4	2.3784	1.51E-05	-2.20	3.15E-16	-15.50
409.4	2.4428	8.63E-06	-2.45	1.76E-16	-15.76
398.4	2.5101	5.02E-06	-2.70	9.94E-17	-16.00

5. Appendix

T	1000/T	σ_{dc}	$\log(\sigma_{DC,spez.} * T)$	D_{dc}	$\log(D_{dc})$
388.7	2.5726	2.95E-06	-2.94	5.71E-17	-16.24
380.1	2.6308	1.79E-06	-3.17	3.38E-17	-16.47
372.3	2.6861	1.13E-06	-3.38	2.08E-17	-16.68
365.8	2.7339	7.19E-07	-3.58	1.31E-17	-16.88
359.3	2.7832	4.75E-07	-3.77	8.47E-18	-17.07
352.7	2.8353	3.15E-07	-3.95	5.52E-18	-17.26
347.2	2.8800	2.19E-07	-4.12	3.78E-18	-17.42
342.4	2.9204	1.56E-07	-4.27	2.66E-18	-17.57
338.4	2.9548	1.15E-07	-4.41	1.93E-18	-17.71
334.7	2.9879	8.62E-08	-4.54	1.43E-18	-17.84
330.8	3.0228	6.61E-08	-4.66	1.09E-18	-17.96
327.1	3.0571	5.18E-08	-4.77	8.42E-19	-18.07
324.1	3.0854	4.16E-08	-4.87	6.71E-19	-18.17
321.5	3.1106	3.42E-08	-4.96	5.47E-19	-18.26

5. Appendix

5.F Impedance spectroscopy data derived from IS spectra for sample DG2

Sample DG2 $\qquad$ c(Li) / #Li / m^3 = $\quad$ 8.81E+27

T	1000/T	σ_{dc}	$\log(\sigma_{DC,spez.} * T)$	D_{dc}	$\log(D_{dc})$
K	K^{-1}	S/m	$\log(/\,SKm^{-1})$	$m^2\,s^{-1}$	$\log(\,m^2\,s^{-1}\,)$
360.5	2.7741	4.93E-07	-3.75	1.08E-17	-16.96
367.6	2.7200	8.08E-07	-3.53	1.81E-17	-16.74
379.5	2.6349	1.64E-06	-3.20	3.81E-17	-16.42
391.7	2.5529	3.30E-06	-2.89	7.90E-17	-16.10
403.4	2.4792	6.28E-06	-2.60	1.55E-16	-15.81
414.6	2.4118	1.15E-05	-2.32	2.91E-16	-15.54
426.3	2.3460	2.04E-05	-2.06	5.32E-16	-15.27
437.6	2.2850	3.49E-05	-1.82	9.32E-16	-15.03
449.1	2.2264	5.71E-05	-1.59	1.57E-15	-14.81
459.8	2.1750	9.02E-05	-1.38	2.53E-15	-14.60
469.4	2.1304	1.38E-04	-1.19	3.95E-15	-14.40
479.5	2.0857	2.07E-04	-1.00	6.06E-15	-14.22
489.7	2.0422	3.06E-04	-0.82	9.15E-15	-14.04
500.5	1.9982	4.45E-04	-0.65	1.36E-14	-13.87
510.4	1.9594	6.34E-04	-0.49	1.97E-14	-13.70
519.5	1.9251	8.83E-04	-0.34	2.80E-14	-13.55
528.9	1.8908	1.21E-03	-0.19	3.91E-14	-13.41
538.2	1.8579	1.64E-03	-0.06	5.38E-14	-13.27
548.3	1.8240	2.19E-03	0.08	7.33E-14	-13.14
557.9	1.7924	2.90E-03	0.21	9.87E-14	-13.01
566.8	1.7644	3.80E-03	0.33	1.31E-13	-12.88
575.7	1.7369	4.92E-03	0.45	1.73E-13	-12.76
584.8	1.7099	6.31E-03	0.57	2.25E-13	-12.65
594.4	1.6824	8.01E-03	0.68	2.91E-13	-12.54
603.9	1.6560	1.01E-02	0.79	3.73E-13	-12.43
612.7	1.6320	1.27E-02	0.89	4.76E-13	-12.32
621.1	1.6101	1.57E-02	0.99	5.94E-13	-12.23
625.7	1.5983	1.74E-02	1.04	6.65E-13	-12.18
626.6	1.5960	1.76E-02	1.04	6.74E-13	-12.17
626.9	1.5953	1.75E-02	1.04	6.68E-13	-12.17
626.2	1.5971	1.73E-02	1.03	6.61E-13	-12.18
625.3	1.5992	1.70E-02	1.03	6.49E-13	-12.19
610.8	1.6373	1.19E-02	0.86	4.45E-13	-12.35
587.2	1.7030	6.50E-03	0.58	2.33E-13	-12.63
563.6	1.7744	3.27E-03	0.27	1.12E-13	-12.95
541.4	1.8471	1.66E-03	-0.05	5.49E-14	-13.26
520.8	1.9202	8.65E-04	-0.35	2.75E-14	-13.56
501.6	1.9936	4.38E-04	-0.66	1.34E-14	-13.87
484.2	2.0653	2.31E-04	-0.95	6.84E-15	-14.17
468.2	2.1358	1.20E-04	-1.25	3.42E-15	-14.47
454.0	2.2029	6.44E-05	-1.53	1.78E-15	-14.75
440.4	2.2707	3.48E-05	-1.81	9.35E-16	-15.03
427.2	2.3407	1.90E-05	-2.09	4.97E-16	-15.30

5. Appendix

T	1000/T	σ_{dc}	$\log(\sigma_{DC,spez.} * T)$	D_{dc}	$\log(D_{dc})$
415.3	2.4080	1.06E-05	-2.36	2.68E-16	-15.57
404.5	2.4724	6.00E-06	-2.62	1.48E-16	-15.83
394.7	2.5335	3.50E-06	-2.86	8.43E-17	-16.07
386.2	2.5894	2.07E-06	-3.10	4.89E-17	-16.31
377.4	2.6498	1.24E-06	-3.33	2.87E-17	-16.54
369.5	2.7067	7.72E-07	-3.54	1.74E-17	-16.76
362.5	2.7584	4.93E-07	-3.75	1.09E-17	-16.96
356.5	2.8052	3.22E-07	-3.94	7.01E-18	-17.15
351.3	2.8462	2.18E-07	-4.12	4.67E-18	-17.33
346.0	2.8905	1.50E-07	-4.29	3.16E-18	-17.50
340.8	2.9343	1.06E-07	-4.44	2.20E-18	-17.66
336.5	2.9719	7.71E-08	-4.59	1.58E-18	-17.80
332.7	3.0057	5.76E-08	-4.72	1.17E-18	-17.93
329.4	3.0362	4.41E-08	-4.84	8.86E-19	-18.05
326.9	3.0591	3.45E-08	-4.95	6.89E-19	-18.16
323.6	3.0904	2.76E-08	-5.05	5.44E-19	-18.26
320.6	3.1188	2.25E-08	-5.14	4.41E-19	-18.36
318.3	3.1419	1.89E-08	-5.22	3.67E-19	-18.43
316.2	3.1624	1.63E-08	-5.29	3.14E-19	-18.50
315.0	3.1750	1.42E-08	-5.35	2.73E-19	-18.56
313.3	3.1915	1.27E-08	-5.40	2.42E-19	-18.62
311.1	3.2140	1.14E-08	-5.45	2.17E-19	-18.66
309.5	3.2307	1.05E-08	-5.49	1.99E-19	-18.70
308.3	3.2437	9.89E-09	-5.52	1.86E-19	-18.73
307.8	3.2491	9.39E-09	-5.54	1.76E-19	-18.75
306.9	3.2589	9.00E-09	-5.56	1.69E-19	-18.77

5. Appendix

5.G   Impedance spectroscopy data derived from IS spectra for sample DG3

Sample DG3 $c(Li) / \#Li / m^3 =$ 8.18E+27

T	1000/T	σ_{dc}	$\log(\sigma_{DC,spez.} * T)$	D_{dc}	$\log(D_{dc})$
K	1000/T / K^{-1}	S/m	log(/ SKm^{-1})	m^2 s^{-1}	log(m^2 s^{-1})
339.8	2.9428	1.05E-07	-4.45	2.34E-18	-17.63
352.0	2.8407	2.54E-07	-4.05	5.87E-18	-17.23
364.3	2.7451	5.78E-07	-3.68	1.38E-17	-16.86
376.6	2.6555	1.21E-06	-3.34	3.00E-17	-16.52
387.5	2.5809	2.37E-06	-3.04	6.05E-17	-16.22
398.3	2.5109	4.40E-06	-2.76	1.15E-16	-15.94
409.1	2.4442	7.84E-06	-2.49	2.11E-16	-15.68
420.6	2.3777	1.37E-05	-2.24	3.80E-16	-15.42
432.2	2.3136	2.34E-05	-1.99	6.66E-16	-15.18
442.3	2.2607	3.87E-05	-1.77	1.12E-15	-14.95
452.7	2.2090	6.17E-05	-1.55	1.84E-15	-14.74
462.9	2.1603	9.53E-05	-1.36	2.90E-15	-14.54
473.1	2.1139	1.43E-04	-1.17	4.46E-15	-14.35
483.7	2.0675	2.13E-04	-0.99	6.78E-15	-14.17
493.4	2.0269	3.12E-04	-0.81	1.01E-14	-13.99
502.9	1.9883	4.49E-04	-0.65	1.49E-14	-13.83
512.6	1.9507	6.34E-04	-0.49	2.14E-14	-13.67
522.2	1.9151	8.75E-04	-0.34	3.00E-14	-13.52
532.0	1.8799	1.19E-03	-0.20	4.15E-14	-13.38
541.5	1.8467	1.60E-03	-0.06	5.69E-14	-13.25
550.3	1.8171	2.13E-03	0.07	7.71E-14	-13.11
559.5	1.7872	2.81E-03	0.20	1.04E-13	-12.98
568.8	1.7581	3.68E-03	0.32	1.37E-13	-12.86
578.2	1.7295	4.74E-03	0.44	1.80E-13	-12.74
587.7	1.7015	6.05E-03	0.55	2.34E-13	-12.63
596.4	1.6768	7.67E-03	0.66	3.01E-13	-12.52
605.4	1.6518	9.70E-03	0.77	3.86E-13	-12.41
614.6	1.6270	1.22E-02	0.87	4.91E-13	-12.31
621.8	1.6083	1.43E-02	0.95	5.85E-13	-12.23
624.1	1.6024	1.50E-02	0.97	6.14E-13	-12.21
624.0	1.6026	1.49E-02	0.97	6.13E-13	-12.21
623.2	1.6045	1.48E-02	0.96	6.06E-13	-12.22
622.9	1.6053	1.47E-02	0.96	6.00E-13	-12.22
616.8	1.6212	1.26E-02	0.89	5.12E-13	-12.29
595.7	1.6787	7.36E-03	0.64	2.88E-13	-12.54
572.1	1.7479	3.79E-03	0.34	1.43E-13	-12.85
548.9	1.8220	1.93E-03	0.02	6.96E-14	-13.16
527.4	1.8961	9.81E-04	-0.29	3.40E-14	-13.47
507.9	1.9690	5.01E-04	-0.59	1.67E-14	-13.78
489.9	2.0411	2.58E-04	-0.90	8.31E-15	-14.08
474.1	2.1092	1.34E-04	-1.20	4.18E-15	-14.38
458.5	2.1811	7.05E-05	-1.49	2.13E-15	-14.67
443.8	2.2534	3.82E-05	-1.77	1.11E-15	-14.95

5. Appendix

T	1000/T	σ_{dc}	$\log(\sigma_{DC,spez.} * T)$	D_{dc}	$\log(D_{dc})$
430.6	2.3221	2.04E-05	-2.06	5.78E-16	-15.24
418.6	2.3889	1.15E-05	-2.32	3.15E-16	-15.50
407.8	2.4519	6.42E-06	-2.58	1.72E-16	-15.76
398.1	2.5122	3.68E-06	-2.83	9.64E-17	-16.02
387.9	2.5778	2.16E-06	-3.08	5.50E-17	-16.26
379.2	2.6374	1.29E-06	-3.31	3.23E-17	-16.49
371.4	2.6928	8.00E-07	-3.53	1.95E-17	-16.71
364.3	2.7449	5.01E-07	-3.74	1.20E-17	-16.92
358.4	2.7899	3.25E-07	-3.93	7.66E-18	-17.12
352.5	2.8365	2.16E-07	-4.12	5.01E-18	-17.30
346.7	2.8845	1.47E-07	-4.29	3.35E-18	-17.48
341.8	2.9258	1.03E-07	-4.45	2.32E-18	-17.63
337.5	2.9632	7.46E-08	-4.60	1.66E-18	-17.78
334.2	2.9926	5.52E-08	-4.73	1.21E-18	-17.92
330.6	3.0249	4.17E-08	-4.86	9.06E-19	-18.04
326.7	3.0608	3.22E-08	-4.98	6.93E-19	-18.16
323.7	3.0897	2.57E-08	-5.08	5.46E-19	-18.26
321.1	3.1147	2.09E-08	-5.17	4.41E-19	-18.36
319.1	3.1339	1.75E-08	-5.25	3.66E-19	-18.44
317.3	3.1514	1.49E-08	-5.33	3.10E-19	-18.51

5. Appendix

5.H   EDX data on Al$_2$O$_3$ detection in lithium tri-silicate powder after Mess4:

EDX spectrum on dark powder surface (yellow cross):
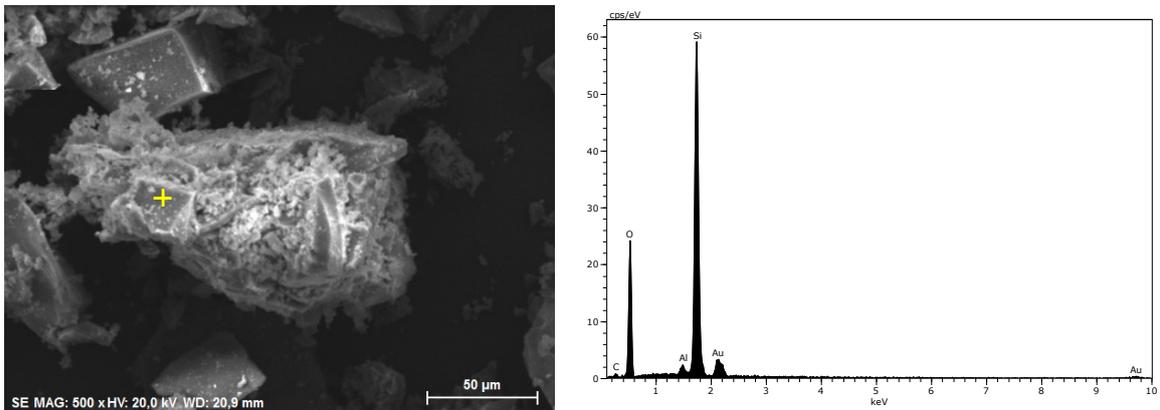
EDX spectrum on bright surface contamination (yellow cross):
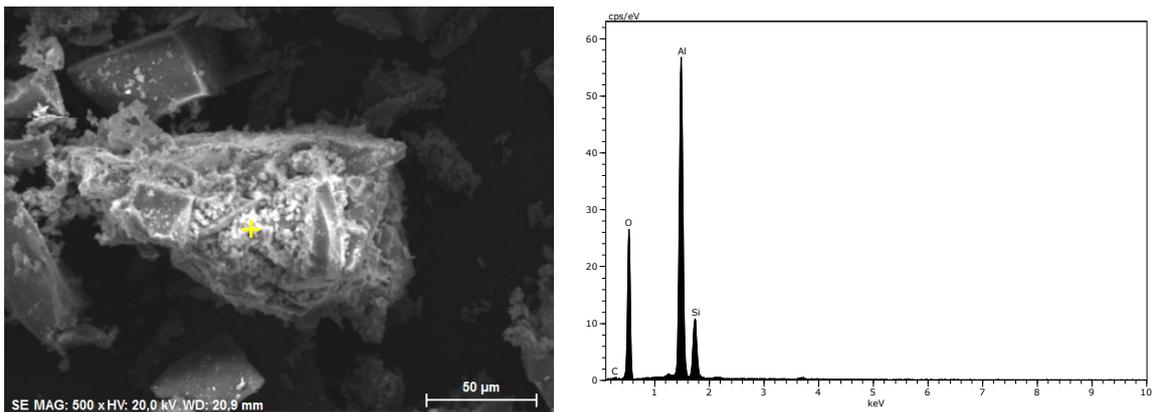
EDX mapping of particles (mapped region is marked by green rectangular):
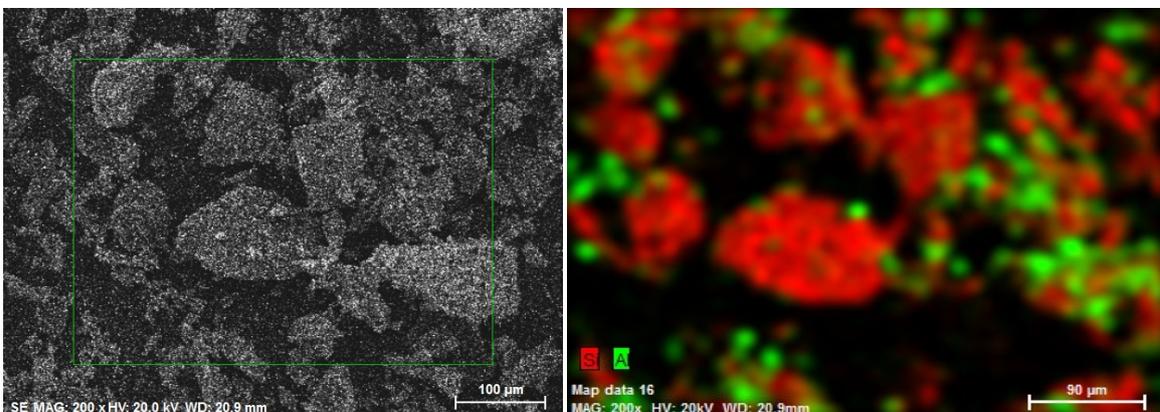
5. Appendix

5.I   Results on particle size measurement of untreated lithium tri-silicate powder

cons. no.	Ø a μm	Ø b μm	f_A μm/μm	$V_{particle}$ mm^3	cons. no.	Ø a μm	Ø b μm	f_A μm/μm	$V_{particle}$ mm^3
1	10.59	9.20	0.87	3.75E-06	46	24.67	14.17	0.57	2.07E-05
2	11.50	7.75	0.67	2.89E-06	47	24.99	24.20	0.97	6.13E-05
3	12.04	10.74	0.89	5.82E-06	48	25.04	24.94	1.00	6.52E-05
4	12.24	11.42	0.93	6.68E-06	49	25.09	7.89	0.31	6.54E-06
5	12.55	10.37	0.83	5.65E-06	50	25.30	9.74	0.38	1.01E-05
6	12.72	11.39	0.90	6.91E-06	51	25.67	16.23	0.63	2.83E-05
7	12.94	12.94	1.00	9.09E-06	52	25.78	17.35	0.67	3.25E-05
8	13.25	8.61	0.65	4.11E-06	53	26.04	14.43	0.55	2.27E-05
9	13.34	8.91	0.67	4.44E-06	54	26.60	11.06	0.42	1.36E-05
10	14.28	12.51	0.88	9.36E-06	55	26.62	17.41	0.65	3.38E-05
11	14.28	12.53	0.88	9.40E-06	56	27.69	20.39	0.74	4.82E-05
12	14.49	13.87	0.96	1.17E-05	57	27.79	26.02	0.94	7.88E-05
13	14.64	12.92	0.88	1.02E-05	58	28.38	10.30	0.36	1.26E-05
14	14.86	9.16	0.62	5.22E-06	59	28.49	21.75	0.76	5.64E-05
15	15.26	14.14	0.93	1.28E-05	60	28.56	15.40	0.54	2.84E-05
16	15.36	11.91	0.78	9.13E-06	61	28.79	10.50	0.36	1.33E-05
17	15.51	14.74	0.95	1.41E-05	62	28.85	14.59	0.51	2.57E-05
18	16.02	10.47	0.65	7.36E-06	63	29.22	25.68	0.88	8.07E-05
19	16.07	7.98	0.50	4.29E-06	64	29.69	28.24	0.95	9.92E-05
20	16.20	10.04	0.62	6.85E-06	65	29.85	28.85	0.97	1.04E-04
21	16.39	12.24	0.75	1.03E-05	66	30.04	22.18	0.74	6.19E-05
22	16.50	12.64	0.77	1.10E-05	67	30.23	22.01	0.73	6.13E-05
23	16.78	13.75	0.82	1.33E-05	68	30.42	22.34	0.73	6.36E-05
24	17.65	8.43	0.48	5.26E-06	69	30.75	27.93	0.91	1.00E-04
25	18.41	16.47	0.89	2.09E-05	70	30.78	16.43	0.53	3.48E-05
26	18.57	13.75	0.74	1.47E-05	71	30.82	16.82	0.55	3.65E-05
27	19.17	12.62	0.66	1.28E-05	72	31.43	29.81	0.95	1.17E-04
28	19.58	16.85	0.86	2.33E-05	73	31.67	27.33	0.86	9.91E-05
29	19.67	15.49	0.79	1.98E-05	74	32.33	20.41	0.63	5.64E-05
30	19.68	12.38	0.63	1.26E-05	75	32.40	23.10	0.71	7.24E-05
31	19.73	16.13	0.82	2.15E-05	76	32.62	12.19	0.37	2.03E-05
32	20.18	12.19	0.60	1.26E-05	77	32.70	31.08	0.95	1.32E-04
33	20.32	9.27	0.46	7.32E-06	78	32.91	14.70	0.45	2.98E-05
34	20.67	15.94	0.77	2.20E-05	79	32.94	23.39	0.71	7.55E-05
35	20.76	20.42	0.98	3.63E-05	80	33.41	28.80	0.86	1.16E-04
36	20.83	14.35	0.69	1.80E-05	81	33.49	21.15	0.63	6.28E-05
37	21.06	18.05	0.86	2.87E-05	82	33.55	26.50	0.79	9.87E-05
38	21.12	14.72	0.70	1.92E-05	83	33.93	16.29	0.48	3.77E-05
39	21.17	16.69	0.79	2.47E-05	84	34.03	29.77	0.87	1.26E-04
40	22.38	20.09	0.90	3.79E-05	85	34.15	12.72	0.37	2.31E-05
41	22.83	15.14	0.66	2.19E-05	86	34.32	19.53	0.57	5.48E-05
42	23.00	18.83	0.82	3.42E-05	87	34.54	28.40	0.82	1.17E-04
43	23.09	20.06	0.87	3.89E-05	88	34.54	26.28	0.76	9.99E-05
44	23.43	13.82	0.59	1.87E-05	89	34.89	17.61	0.50	4.53E-05
45	23.75	18.95	0.80	3.57E-05	90	34.92	22.50	0.64	7.40E-05

5. Appendix

cons. no.	Ø a μm	Ø b μm	f_A μm/μm	$V_{particle}$ mm³	cons. no.	Ø a μm	Ø b μm	f_A μm/μm	$V_{particle}$ mm³
91	35.13	34.03	0.97	1.70E-04	136	54.94	46.37	0.84	4.95E-04
92	35.82	21.94	0.61	7.22E-05	137	55.38	27.13	0.49	1.71E-04
93	36.07	27.88	0.77	1.17E-04	138	55.50	28.43	0.51	1.88E-04
94	36.49	19.46	0.53	5.79E-05	139	55.79	48.55	0.87	5.51E-04
95	36.82	18.64	0.51	5.36E-05	140	57.72	45.32	0.79	4.97E-04
96	37.31	14.88	0.40	3.46E-05	141	59.26	51.62	0.87	6.61E-04
97	37.71	19.76	0.52	6.17E-05	142	59.77	56.34	0.94	7.95E-04
98	38.08	34.41	0.90	1.89E-04	143	60.38	36.10	0.60	3.30E-04
99	38.42	13.93	0.36	3.12E-05	144	61.58	48.37	0.79	6.03E-04
100	38.44	18.90	0.49	5.75E-05	145	61.62	52.51	0.85	7.12E-04
101	38.72	35.21	0.91	2.01E-04	146	61.85	26.59	0.43	1.83E-04
102	39.58	18.84	0.48	5.88E-05	147	61.98	19.66	0.32	1.00E-04
103	39.76	37.61	0.95	2.36E-04	148	63.80	22.27	0.35	1.33E-04
104	40.31	17.91	0.44	5.42E-05	149	66.06	33.89	0.51	3.18E-04
105	40.74	37.01	0.91	2.34E-04	150	66.15	19.00	0.29	1.00E-04
106	41.98	28.57	0.68	1.44E-04	151	66.17	26.15	0.40	1.89E-04
107	42.43	28.00	0.66	1.39E-04	152	67.69	35.06	0.52	3.49E-04
108	42.76	22.89	0.54	9.38E-05	153	69.32	59.21	0.85	1.02E-03
109	43.25	37.46	0.87	2.54E-04	154	70.52	32.18	0.46	3.06E-04
110	43.48	7.60	0.17	1.05E-05	155	70.74	45.05	0.64	6.01E-04
111	43.62	42.08	0.96	3.24E-04	156	74.34	52.60	0.71	8.62E-04
112	43.80	8.91	0.20	1.46E-05	157	75.57	26.01	0.34	2.14E-04
113	44.10	19.83	0.45	7.26E-05	158	79.23	26.29	0.33	2.29E-04
114	44.54	14.33	0.32	3.83E-05	159	79.31	50.08	0.63	8.33E-04
115	44.78	15.99	0.36	4.80E-05	160	85.57	66.12	0.77	1.57E-03
116	45.02	36.87	0.82	2.56E-04	161	90.12	32.96	0.37	4.10E-04
117	45.45	26.97	0.59	1.38E-04	162	94.36	26.62	0.28	2.80E-04
118	45.82	31.40	0.69	1.89E-04	163	96.58	80.49	0.83	2.62E-03
119	46.22	7.97	0.17	1.23E-05	164	96.97	30.40	0.31	3.75E-04
120	47.25	15.97	0.34	5.05E-05	165	98.91	60.56	0.61	1.52E-03
121	47.26	32.73	0.69	2.12E-04	166	105.10	70.30	0.67	2.18E-03
122	47.45	40.39	0.85	3.24E-04	167	105.64	65.09	0.62	1.88E-03
123	47.48	43.38	0.91	3.74E-04	168	112.24	52.42	0.47	1.29E-03
124	48.50	22.52	0.46	1.03E-04	169	116.20	56.35	0.48	1.55E-03
125	48.80	47.03	0.96	4.52E-04	170	121.47	116.67	0.96	6.93E-03
126	49.04	34.57	0.70	2.45E-04	171	122.71	101.24	0.83	5.27E-03
127	49.06	44.71	0.91	4.11E-04	172	128.33	95.19	0.74	4.87E-03
128	49.07	16.34	0.33	5.49E-05	173	128.65	91.52	0.71	4.51E-03
129	50.03	26.91	0.54	1.52E-04	174	132.66	96.98	0.73	5.23E-03
130	50.34	41.52	0.82	3.64E-04	175	147.99	125.48	0.85	9.76E-03
131	51.19	20.18	0.39	8.73E-05	176	156.12	91.07	0.58	5.42E-03
132	52.15	27.75	0.53	1.68E-04	177	174.94	161.59	0.92	1.91E-02
133	52.41	23.30	0.44	1.19E-04	178	177.23	131.64	0.74	1.29E-02
134	53.17	19.28	0.36	8.28E-05	179	219.66	118.76	0.54	1.30E-02
135	54.34	13.16	0.24	3.94E-05					

5. Appendix

5.J   Results on particle size measurement of lithium tri-silicate powder after Mess2

cons. no.	Ø a μm	Ø b μm	f_A μm/μm	$V_{particle}$ mm³	cons. no.	Ø a μm	Ø b μm	f_A μm/μm	$V_{particle}$ mm³
1	7.02	6.35	0.91	1.19E-06	46	16.08	15.16	0.94	1.55E-05
2	7.43	2.74	0.37	2.33E-07	47	16.09	15.31	0.95	1.58E-05
3	8.64	4.55	0.53	7.50E-07	48	16.48	12.43	0.75	1.07E-05
4	8.68	8.65	1.00	2.72E-06	49	16.54	8.23	0.50	4.70E-06
5	9.00	4.50	0.50	7.63E-07	50	16.67	8.94	0.54	5.59E-06
6	9.08	7.55	0.83	2.17E-06	51	16.70	7.16	0.43	3.59E-06
7	9.91	3.09	0.31	3.97E-07	52	16.74	13.20	0.79	1.22E-05
8	10.38	8.40	0.81	3.07E-06	53	16.74	15.38	0.92	1.66E-05
9	10.40	6.65	0.64	1.92E-06	54	16.85	14.17	0.84	1.42E-05
10	10.58	10.25	0.97	4.66E-06	55	16.99	10.70	0.63	8.15E-06
11	10.60	7.33	0.69	2.39E-06	56	17.06	12.89	0.76	1.19E-05
12	11.10	10.61	0.96	5.24E-06	57	17.14	15.89	0.93	1.81E-05
13	11.28	8.10	0.72	3.10E-06	58	17.16	16.43	0.96	1.94E-05
14	11.48	7.26	0.63	2.53E-06	59	17.17	7.93	0.46	4.53E-06
15	11.58	9.46	0.82	4.34E-06	60	17.19	14.70	0.86	1.56E-05
16	11.68	6.24	0.53	1.91E-06	61	17.30	12.27	0.71	1.09E-05
17	12.00	12.00	1.00	7.24E-06	62	17.44	11.71	0.67	1.00E-05
18	12.08	2.59	0.21	3.40E-07	63	17.48	10.60	0.61	8.23E-06
19	12.13	11.51	0.95	6.73E-06	64	17.53	17.17	0.98	2.16E-05
20	12.33	6.68	0.54	2.31E-06	65	17.54	13.83	0.79	1.40E-05
21	12.85	10.23	0.80	5.63E-06	66	17.71	15.39	0.87	1.76E-05
22	12.91	12.84	0.99	8.92E-06	67	17.79	14.63	0.82	1.60E-05
23	13.00	9.19	0.71	4.60E-06	68	17.79	15.37	0.86	1.76E-05
24	13.47	9.87	0.73	5.50E-06	69	17.81	7.99	0.45	4.77E-06
25	13.49	7.83	0.58	3.47E-06	70	18.09	15.73	0.87	1.87E-05
26	13.54	9.17	0.68	4.77E-06	71	18.14	8.99	0.50	6.14E-06
27	13.86	5.10	0.37	1.51E-06	72	18.17	10.41	0.57	8.24E-06
28	14.02	8.64	0.62	4.38E-06	73	18.27	16.44	0.90	2.07E-05
29	14.26	9.84	0.69	5.78E-06	74	18.32	7.85	0.43	4.73E-06
30	14.37	14.26	0.99	1.22E-05	75	18.40	7.39	0.40	4.20E-06
31	14.45	10.07	0.70	6.14E-06	76	18.45	14.93	0.81	1.72E-05
32	14.47	12.14	0.84	8.93E-06	77	18.46	18.32	0.99	2.60E-05
33	14.58	14.15	0.97	1.22E-05	78	18.52	13.40	0.72	1.39E-05
34	14.69	11.13	0.76	7.63E-06	79	18.56	14.43	0.78	1.62E-05
35	14.85	11.28	0.76	7.92E-06	80	18.66	11.67	0.63	1.06E-05
36	15.00	8.28	0.55	4.30E-06	81	18.69	15.83	0.85	1.96E-05
37	15.24	9.10	0.60	5.28E-06	82	18.72	11.20	0.60	9.84E-06
38	15.43	6.05	0.39	2.37E-06	83	18.78	13.29	0.71	1.39E-05
39	15.62	7.81	0.50	3.99E-06	84	19.02	13.85	0.73	1.53E-05
40	15.67	13.81	0.88	1.25E-05	85	19.02	9.20	0.48	6.74E-06
41	15.68	10.65	0.68	7.45E-06	86	19.09	14.29	0.75	1.63E-05
42	15.69	4.26	0.27	1.19E-06	87	19.19	16.00	0.83	2.06E-05
43	15.94	12.08	0.76	9.74E-06	88	19.25	10.69	0.56	9.21E-06
44	16.01	8.49	0.53	4.83E-06	89	19.31	17.47	0.90	2.47E-05
45	16.03	7.85	0.49	4.14E-06	90	19.33	18.41	0.95	2.74E-05

5. Appendix

cons. no.	Ø a μm	Ø b μm	f_A μm/μm	$V_{particle}$ mm³	cons. no.	Ø a μm	Ø b μm	f_A μm/μm	$V_{particle}$ mm³
91	19.34	10.19	0.53	8.42E-06	136	23.74	22.94	0.97	5.23E-05
92	19.38	12.69	0.65	1.31E-05	137	23.77	13.89	0.58	1.92E-05
93	19.45	15.42	0.79	1.94E-05	138	23.87	17.63	0.74	3.11E-05
94	19.46	12.89	0.66	1.35E-05	139	24.06	8.85	0.37	7.90E-06
95	19.47	5.47	0.28	2.44E-06	140	24.15	14.74	0.61	2.20E-05
96	19.59	12.03	0.61	1.19E-05	141	24.19	20.88	0.86	4.42E-05
97	19.72	7.93	0.40	5.20E-06	142	24.21	7.06	0.29	5.06E-06
98	19.79	16.09	0.81	2.15E-05	143	24.36	20.53	0.84	4.30E-05
99	19.81	12.82	0.65	1.36E-05	144	24.46	15.50	0.63	2.46E-05
100	19.85	12.20	0.61	1.24E-05	145	24.71	14.83	0.60	2.28E-05
101	19.87	15.45	0.78	1.99E-05	146	24.71	10.75	0.43	1.20E-05
102	19.89	12.02	0.60	1.20E-05	147	24.71	19.45	0.79	3.92E-05
103	19.90	7.36	0.37	4.52E-06	148	24.84	17.13	0.69	3.05E-05
104	19.95	19.30	0.97	3.11E-05	149	24.90	21.00	0.84	4.60E-05
105	19.99	15.56	0.78	2.03E-05	150	25.46	16.06	0.63	2.75E-05
106	20.01	10.84	0.54	9.85E-06	151	25.70	16.85	0.66	3.06E-05
107	20.02	10.18	0.51	8.69E-06	152	25.72	16.73	0.65	3.02E-05
108	20.16	18.38	0.91	2.85E-05	153	25.79	18.08	0.70	3.53E-05
109	20.45	15.04	0.74	1.94E-05	154	25.99	20.24	0.78	4.46E-05
110	20.47	18.13	0.89	2.82E-05	155	26.06	17.12	0.66	3.20E-05
111	20.57	15.22	0.74	2.00E-05	156	26.10	19.32	0.74	4.08E-05
112	20.66	16.79	0.81	2.44E-05	157	26.35	14.07	0.53	2.18E-05
113	20.68	11.36	0.55	1.12E-05	158	26.40	17.91	0.68	3.55E-05
114	20.75	11.29	0.54	1.11E-05	159	26.42	11.60	0.44	1.49E-05
115	20.81	10.71	0.51	1.00E-05	160	26.84	9.53	0.36	1.02E-05
116	20.87	17.59	0.84	2.71E-05	161	26.93	9.39	0.35	9.94E-06
117	20.99	15.00	0.71	1.98E-05	162	27.56	21.31	0.77	5.24E-05
118	21.05	8.97	0.43	7.09E-06	163	27.68	14.33	0.52	2.38E-05
119	21.09	20.59	0.98	3.75E-05	164	28.67	14.58	0.51	2.55E-05
120	21.10	7.82	0.37	5.41E-06	165	28.69	17.03	0.59	3.49E-05
121	21.28	12.48	0.59	1.39E-05	166	28.70	28.03	0.98	9.45E-05
122	21.35	5.46	0.26	2.66E-06	167	29.03	15.67	0.54	2.99E-05
123	21.51	17.63	0.82	2.80E-05	168	29.35	18.64	0.64	4.27E-05
124	21.57	8.12	0.38	5.95E-06	169	29.41	18.10	0.62	4.04E-05
125	21.67	20.24	0.93	3.72E-05	170	29.41	18.29	0.62	4.12E-05
126	21.70	9.22	0.42	7.73E-06	171	29.57	20.42	0.69	5.16E-05
127	21.76	16.64	0.76	2.52E-05	172	29.71	10.77	0.36	1.44E-05
128	21.80	15.52	0.71	2.20E-05	173	29.75	27.31	0.92	9.30E-05
129	21.83	6.62	0.30	4.00E-06	174	29.76	17.65	0.59	3.88E-05
130	22.54	10.82	0.48	1.11E-05	175	29.89	10.68	0.36	1.43E-05
131	22.65	22.65	1.00	4.87E-05	176	29.90	26.91	0.90	9.07E-05
132	22.79	12.89	0.57	1.59E-05	177	29.94	7.56	0.25	7.17E-06
133	22.92	13.95	0.61	1.87E-05	178	30.15	25.26	0.84	8.06E-05
134	23.16	18.66	0.81	3.38E-05	179	30.44	14.25	0.47	2.59E-05
135	23.70	11.78	0.50	1.38E-05	180	30.52	26.04	0.85	8.67E-05

5. Appendix

cons. no.	Ø a μm	Ø b μm	f_A μm/μm	$V_{particle}$ mm³	cons. no.	Ø a μm	Ø b μm	f_A μm/μm	$V_{particle}$ mm³
181	30.79	22.41	0.73	6.48E-05	226	40.28	19.65	0.49	6.52E-05
182	30.92	22.33	0.72	6.46E-05	227	40.46	30.06	0.74	1.53E-04
183	30.96	23.93	0.77	7.43E-05	228	40.49	12.61	0.31	2.70E-05
184	31.31	6.09	0.19	4.87E-06	229	40.54	19.59	0.48	6.52E-05
185	31.54	29.86	0.95	1.18E-04	230	40.74	36.96	0.91	2.33E-04
186	31.59	18.50	0.59	4.53E-05	231	40.87	40.75	1.00	2.84E-04
187	31.67	28.16	0.89	1.05E-04	232	40.94	22.20	0.54	8.45E-05
188	32.04	22.67	0.71	6.89E-05	233	40.98	16.26	0.40	4.54E-05
189	32.23	20.69	0.64	5.78E-05	234	41.04	41.04	1.00	2.89E-04
190	32.26	20.93	0.65	5.92E-05	235	41.73	33.67	0.81	1.98E-04
191	32.37	28.52	0.88	1.10E-04	236	42.02	18.82	0.45	6.24E-05
192	32.46	25.72	0.79	8.99E-05	237	42.15	26.89	0.64	1.28E-04
193	32.68	18.33	0.56	4.60E-05	238	42.24	31.97	0.76	1.81E-04
194	32.76	13.47	0.41	2.49E-05	239	42.60	14.40	0.34	3.70E-05
195	33.56	25.87	0.77	9.41E-05	240	42.71	29.07	0.68	1.51E-04
196	33.75	23.93	0.71	8.09E-05	241	42.94	42.66	0.99	3.27E-04
197	33.88	20.75	0.61	6.11E-05	242	43.42	43.11	0.99	3.38E-04
198	34.24	21.57	0.63	6.67E-05	243	44.33	21.87	0.49	8.88E-05
199	34.35	24.13	0.70	8.38E-05	244	44.91	39.00	0.87	2.86E-04
200	34.59	15.57	0.45	3.51E-05	245	45.01	39.37	0.87	2.92E-04
201	34.78	32.00	0.92	1.49E-04	246	45.43	29.93	0.66	1.70E-04
202	35.12	16.71	0.48	4.11E-05	247	45.74	21.70	0.47	9.02E-05
203	35.20	17.74	0.50	4.64E-05	248	45.95	33.18	0.72	2.12E-04
204	35.38	19.74	0.56	5.78E-05	249	46.02	35.18	0.76	2.39E-04
205	35.46	16.21	0.46	3.90E-05	250	46.25	36.91	0.80	2.64E-04
206	35.96	20.88	0.58	6.56E-05	251	46.31	28.23	0.61	1.55E-04
207	36.06	12.77	0.35	2.46E-05	252	47.75	43.33	0.91	3.76E-04
208	36.43	17.75	0.49	4.81E-05	253	47.96	25.49	0.53	1.31E-04
209	36.72	19.10	0.52	5.61E-05	254	48.09	47.15	0.98	4.48E-04
210	37.01	28.98	0.78	1.30E-04	255	48.10	20.54	0.43	8.50E-05
211	37.08	21.84	0.59	7.41E-05	256	48.22	36.15	0.75	2.64E-04
212	37.16	24.94	0.67	9.69E-05	257	48.24	29.96	0.62	1.81E-04
213	37.20	26.76	0.72	1.12E-04	258	48.81	32.18	0.66	2.12E-04
214	37.65	20.41	0.54	6.57E-05	259	49.24	39.16	0.80	3.16E-04
215	37.68	28.32	0.75	1.27E-04	260	49.62	38.77	0.78	3.13E-04
216	37.74	30.46	0.81	1.47E-04	261	49.86	48.26	0.97	4.86E-04
217	37.95	21.24	0.56	7.17E-05	262	49.95	15.42	0.31	4.98E-05
218	38.42	34.14	0.89	1.88E-04	263	50.07	27.42	0.55	1.58E-04
219	38.66	19.90	0.51	6.41E-05	264	50.68	31.98	0.63	2.17E-04
220	38.84	12.53	0.32	2.56E-05	265	50.86	21.74	0.43	1.01E-04
221	39.27	23.04	0.59	8.73E-05	266	50.96	11.58	0.23	2.86E-05
222	39.30	24.73	0.63	1.01E-04	267	51.24	48.90	0.95	5.13E-04
223	39.97	31.13	0.78	1.62E-04	268	51.86	40.99	0.79	3.65E-04
224	40.24	31.49	0.78	1.67E-04	269	52.30	33.16	0.63	2.41E-04
225	40.26	15.86	0.39	4.24E-05	270	52.72	40.38	0.77	3.60E-04

5. Appendix

cons. no.	Ø a μm	Ø b μm	f_A μm/μm	$V_{particle}$ mm^3
271	53.22	23.93	0.45	1.28E-04
272	53.71	31.43	0.59	2.22E-04
273	54.13	41.99	0.78	4.00E-04
274	54.95	42.44	0.77	4.15E-04
275	55.73	39.61	0.71	3.66E-04
276	56.28	39.26	0.70	3.63E-04
277	57.47	20.94	0.36	1.06E-04
278	57.51	44.63	0.78	4.80E-04
279	57.67	23.21	0.40	1.30E-04
280	57.77	23.45	0.41	1.33E-04
281	58.46	17.45	0.30	7.45E-05
282	59.62	42.22	0.71	4.45E-04
283	59.68	44.88	0.75	5.03E-04
284	61.76	40.38	0.65	4.22E-04
285	63.23	57.34	0.91	8.71E-04
286	64.22	56.95	0.89	8.73E-04
287	66.48	36.49	0.55	3.71E-04
288	66.84	50.49	0.76	7.14E-04
289	67.54	38.80	0.57	4.26E-04
290	71.75	37.53	0.52	4.23E-04
291	71.96	23.30	0.32	1.64E-04
292	73.47	67.22	0.91	1.39E-03
293	73.48	40.57	0.55	5.06E-04
294	75.48	52.32	0.69	8.66E-04
295	76.54	56.68	0.74	1.03E-03
296	84.37	49.08	0.58	8.51E-04
297	86.21	43.16	0.50	6.73E-04
298	88.74	70.35	0.79	1.84E-03
299	88.98	64.86	0.73	1.57E-03
300	92.58	46.64	0.50	8.44E-04
301	93.29	66.83	0.72	1.75E-03
302	93.37	91.05	0.98	3.24E-03
303	95.72	57.33	0.60	1.32E-03
304	96.10	64.96	0.68	1.70E-03
305	97.13	50.54	0.52	1.04E-03
306	97.93	83.91	0.86	2.89E-03
307	98.35	47.68	0.48	9.36E-04
308	100.68	36.34	0.36	5.57E-04
309	101.49	92.58	0.91	3.64E-03
310	110.26	65.64	0.60	1.99E-03
311	118.74	57.49	0.48	1.64E-03

5. Appendix

5.K   Results on particle size measurement of lithium tri-silicate powder after Mess3

cons. no.	Ø a µm	Ø b µm	f_A µm/µm	$V_{particle}$ mm^3	cons. no.	Ø a µm	Ø b µm	f_A µm/µm	$V_{particle}$ mm^3
1	8.50	5.87	0.69	1.22E-06	46	20.60	13.80	0.67	1.64E-05
2	9.00	3.60	0.40	4.89E-07	47	20.70	20.70	1.00	3.72E-05
3	9.20	7.08	0.77	1.93E-06	48	20.80	16.85	0.81	2.47E-05
4	9.60	8.06	0.84	2.61E-06	49	20.80	20.59	0.99	3.69E-05
5	9.90	7.43	0.75	2.29E-06	50	20.80	13.94	0.67	1.69E-05
6	10.00	6.10	0.61	1.56E-06	51	21.00	16.38	0.78	2.36E-05
7	10.70	10.17	0.95	4.63E-06	52	21.10	5.06	0.24	2.27E-06
8	11.60	11.02	0.95	5.90E-06	53	21.80	6.54	0.30	3.91E-06
9	11.70	11.58	0.99	6.58E-06	54	22.50	12.38	0.55	1.44E-05
10	12.10	11.62	0.96	6.84E-06	55	23.10	17.79	0.77	3.06E-05
11	12.10	10.89	0.90	6.01E-06	56	23.10	8.78	0.38	7.46E-06
12	12.60	11.09	0.88	6.49E-06	57	23.20	19.95	0.86	3.87E-05
13	12.80	9.09	0.71	4.43E-06	58	23.30	10.02	0.43	9.80E-06
14	13.00	9.10	0.70	4.51E-06	59	23.40	15.68	0.67	2.41E-05
15	13.30	12.10	0.91	8.16E-06	60	23.80	12.85	0.54	1.65E-05
16	13.50	9.18	0.68	4.77E-06	61	23.80	18.56	0.78	3.44E-05
17	14.00	5.60	0.40	1.84E-06	62	23.80	15.71	0.66	2.46E-05
18	14.00	12.74	0.91	9.52E-06	63	24.10	18.80	0.78	3.57E-05
19	14.00	8.54	0.61	4.28E-06	64	24.20	15.49	0.64	2.43E-05
20	14.20	13.35	0.94	1.06E-05	65	24.30	16.04	0.66	2.62E-05
21	14.40	7.78	0.54	3.65E-06	66	24.60	11.56	0.47	1.38E-05
22	14.70	14.55	0.99	1.30E-05	67	24.70	24.70	1.00	6.31E-05
23	15.00	10.05	0.67	6.35E-06	68	25.00	23.00	0.92	5.54E-05
24	15.20	12.01	0.79	9.18E-06	69	25.60	19.71	0.77	4.17E-05
25	15.20	11.55	0.76	8.50E-06	70	25.60	16.38	0.64	2.88E-05
26	15.50	9.77	0.63	6.19E-06	71	25.80	19.35	0.75	4.05E-05
27	16.00	16.00	1.00	1.72E-05	72	25.80	10.58	0.41	1.21E-05
28	16.30	9.45	0.58	6.10E-06	73	25.90	11.14	0.43	1.35E-05
29	16.50	15.35	0.93	1.63E-05	74	25.90	12.17	0.47	1.61E-05
30	17.20	11.01	0.64	8.73E-06	75	26.30	24.99	0.95	6.88E-05
31	17.60	11.09	0.63	9.06E-06	76	26.30	19.46	0.74	4.17E-05
32	17.70	2.66	0.15	5.23E-07	77	26.40	24.55	0.93	6.67E-05
33	18.00	7.56	0.42	4.31E-06	78	26.60	14.63	0.55	2.38E-05
34	18.50	16.84	0.91	2.20E-05	79	27.30	23.21	0.85	6.16E-05
35	18.90	16.07	0.85	2.04E-05	80	27.50	26.40	0.96	8.03E-05
36	19.30	10.62	0.55	9.11E-06	81	27.60	9.94	0.36	1.14E-05
37	19.30	17.95	0.93	2.60E-05	82	27.70	13.30	0.48	2.05E-05
38	19.40	15.91	0.82	2.06E-05	83	27.70	21.61	0.78	5.42E-05
39	19.60	14.31	0.73	1.68E-05	84	27.70	24.65	0.89	7.05E-05
40	19.60	16.66	0.85	2.28E-05	85	28.00	22.96	0.82	6.18E-05
41	20.30	6.09	0.30	3.15E-06	86	28.10	22.76	0.81	6.10E-05
42	20.40	10.81	0.53	9.99E-06	87	28.30	26.04	0.92	8.04E-05
43	20.50	14.15	0.69	1.72E-05	88	28.80	18.72	0.65	4.23E-05
44	20.60	11.54	0.56	1.15E-05	89	28.90	23.41	0.81	6.63E-05
45	20.60	18.33	0.89	2.90E-05	90	29.00	16.82	0.58	3.44E-05

cons. no.	Ø a µm	Ø b µm	f_A µm/µm	$V_{particle}$ mm³	cons. no.	Ø a µm	Ø b µm	f_A µm/µm	$V_{particle}$ mm³
91	29.20	19.86	0.68	4.82E-05	136	42.20	21.94	0.52	8.51E-05
92	29.60	24.57	0.83	7.48E-05	137	42.80	23.97	0.56	1.03E-04
93	29.70	21.98	0.74	6.01E-05	138	42.80	27.82	0.65	1.39E-04
94	30.10	8.43	0.28	8.96E-06	139	44.70	34.87	0.78	2.28E-04
95	30.70	19.03	0.62	4.66E-05	140	44.90	23.80	0.53	1.07E-04
96	30.90	12.05	0.39	1.88E-05	141	45.00	31.05	0.69	1.82E-04
97	31.10	17.73	0.57	4.09E-05	142	45.40	28.60	0.63	1.56E-04
98	31.10	19.59	0.63	5.00E-05	143	46.30	14.35	0.31	4.00E-05
99	31.20	6.24	0.20	5.09E-06	144	46.30	8.80	0.19	1.50E-05
100	31.80	25.76	0.81	8.84E-05	145	46.40	38.98	0.84	2.95E-04
101	31.90	18.18	0.57	4.42E-05	146	46.40	31.55	0.68	1.93E-04
102	31.90	24.88	0.78	8.27E-05	147	46.50	35.81	0.77	2.50E-04
103	32.40	13.93	0.43	2.63E-05	148	46.90	15.48	0.33	4.71E-05
104	32.50	32.18	0.99	1.41E-04	149	47.10	33.91	0.72	2.27E-04
105	33.30	19.98	0.60	5.57E-05	150	50.00	41.50	0.83	3.61E-04
106	34.10	33.42	0.98	1.60E-04	151	50.10	20.54	0.41	8.85E-05
107	34.30	24.01	0.70	8.28E-05	152	50.80	47.75	0.94	4.85E-04
108	34.50	18.29	0.53	4.83E-05	153	51.70	34.64	0.67	2.60E-04
109	35.00	8.05	0.23	9.50E-06	154	51.90	25.43	0.49	1.41E-04
110	35.10	17.20	0.49	4.35E-05	155	52.70	14.23	0.27	4.47E-05
111	35.60	22.07	0.62	7.26E-05	156	57.80	56.07	0.97	7.61E-04
112	35.60	33.82	0.95	1.71E-04	157	59.10	41.37	0.70	4.24E-04
113	35.60	22.43	0.63	7.50E-05	158	61.10	47.66	0.78	5.81E-04
114	36.20	24.25	0.67	8.92E-05	159	64.00	35.84	0.56	3.44E-04
115	37.00	28.86	0.78	1.29E-04	160	66.50	24.61	0.37	1.69E-04
116	37.30	20.14	0.54	6.34E-05	161	66.90	63.56	0.95	1.13E-03
117	38.00	20.90	0.55	6.95E-05	162	67.10	47.64	0.71	6.38E-04
118	38.00	28.50	0.75	1.29E-04	163	67.20	43.68	0.65	5.37E-04
119	38.40	8.83	0.23	1.25E-05	164	70.10	29.44	0.42	2.55E-04
120	38.50	14.63	0.38	3.45E-05	165	70.20	57.56	0.82	9.74E-04
121	38.50	13.48	0.35	2.93E-05	166	70.40	59.84	0.85	1.06E-03
122	38.50	28.49	0.74	1.31E-04	167	73.70	72.96	0.99	1.64E-03
123	38.50	38.12	0.99	2.34E-04	168	74.20	64.55	0.87	1.30E-03
124	38.70	26.32	0.68	1.12E-04	169	75.10	36.80	0.49	4.26E-04
125	38.80	27.16	0.70	1.20E-04	170	75.80	40.17	0.53	5.12E-04
126	38.80	34.92	0.90	1.98E-04	171	76.40	31.32	0.41	3.14E-04
127	39.20	21.17	0.54	7.36E-05	172	78.40	76.83	0.98	1.94E-03
128	39.80	31.44	0.79	1.65E-04	173	84.90	72.17	0.85	1.85E-03
129	39.80	18.71	0.47	5.83E-05	174	87.20	62.78	0.72	1.44E-03
130	40.10	21.25	0.53	7.59E-05	175	89.80	73.64	0.82	2.04E-03
131	40.30	40.30	1.00	2.74E-04	176	91.60	65.04	0.71	1.62E-03
132	40.80	29.38	0.72	1.47E-04	177	91.90	56.06	0.61	1.21E-03
133	41.10	28.77	0.70	1.42E-04	178	92.20	89.43	0.97	3.09E-03
134	41.20	21.42	0.52	7.92E-05	179	96.00	44.16	0.46	7.84E-04
135	41.40	31.88	0.77	1.76E-04	180	98.00	44.10	0.45	7.98E-04

5. Appendix

cons. no.	Ø a μm	Ø b μm	f_A μm/μm	$V_{particle}$ mm^3
181	101.50	75.11	0.74	2.40E-03
182	103.80	50.86	0.49	1.12E-03
183	104.40	83.52	0.80	3.05E-03
184	106.70	106.70	1.00	5.09E-03
185	107.60	74.24	0.69	2.48E-03
186	111.00	72.15	0.65	2.42E-03
187	133.90	62.93	0.47	2.22E-03
188	138.00	88.32	0.64	4.51E-03
189	139.30	91.94	0.66	4.93E-03

5. Appendix

5.L Results on particle size measurement of lithium tri-silicate powder after Mess4

cons. no.	$\varnothing$ a µm	$\varnothing$ b µm	f_A µm/µm	$V_{particle}$ mm³	cons. no.	$\varnothing$ a µm	$\varnothing$ b µm	f_A µm/µm	$V_{particle}$ mm³
1	5.00	1.58	0.32	5.24E-08	46	14.53	10.57	0.73	6.80E-06
2	5.71	5.08	0.89	6.17E-07	47	14.55	13.03	0.90	1.03E-05
3	6.35	5.69	0.90	8.60E-07	48	14.56	6.58	0.45	2.64E-06
4	6.87	5.56	0.81	8.90E-07	49	14.68	14.68	1.00	1.33E-05
5	6.96	5.50	0.79	8.83E-07	50	14.74	11.84	0.80	8.66E-06
6	7.01	5.24	0.75	8.07E-07	51	14.74	8.89	0.60	4.89E-06
7	7.55	5.97	0.79	1.13E-06	52	14.75	11.35	0.77	7.95E-06
8	7.66	2.18	0.29	1.53E-07	53	14.76	9.93	0.67	6.09E-06
9	8.56	6.23	0.73	1.39E-06	54	14.96	2.49	0.17	3.88E-07
10	8.69	5.45	0.63	1.08E-06	55	15.00	6.72	0.45	2.84E-06
11	9.01	8.12	0.90	2.48E-06	56	15.09	12.51	0.83	9.89E-06
12	9.58	5.35	0.56	1.15E-06	57	15.38	7.87	0.51	3.99E-06
13	9.76	4.64	0.48	8.80E-07	58	15.56	12.28	0.79	9.83E-06
14	10.00	3.52	0.35	5.19E-07	59	15.72	12.85	0.82	1.09E-05
15	10.01	3.67	0.37	5.66E-07	60	15.89	14.41	0.91	1.38E-05
16	10.25	7.16	0.70	2.20E-06	61	15.91	10.91	0.69	7.93E-06
17	10.92	9.57	0.88	4.19E-06	62	15.96	12.67	0.79	1.07E-05
18	11.00	9.17	0.83	3.87E-06	63	15.99	9.18	0.57	5.64E-06
19	11.41	4.21	0.37	8.45E-07	64	16.10	9.31	0.58	5.84E-06
20	11.57	7.32	0.63	2.60E-06	65	16.22	12.98	0.80	1.15E-05
21	11.58	4.68	0.40	1.06E-06	66	16.26	15.38	0.95	1.61E-05
22	11.64	4.18	0.36	8.50E-07	67	16.32	8.68	0.53	5.15E-06
23	11.67	8.75	0.75	3.74E-06	68	16.35	7.94	0.49	4.32E-06
24	11.82	7.90	0.67	3.09E-06	69	16.43	8.10	0.49	4.52E-06
25	11.89	4.66	0.39	1.08E-06	70	16.67	16.27	0.98	1.85E-05
26	12.04	5.02	0.42	1.27E-06	71	16.89	8.26	0.49	4.83E-06
27	12.26	8.67	0.71	3.86E-06	72	17.02	7.08	0.42	3.57E-06
28	12.34	9.42	0.76	4.59E-06	73	17.15	7.94	0.46	4.53E-06
29	12.35	8.43	0.68	3.68E-06	74	17.61	16.82	0.96	2.09E-05
30	12.41	2.91	0.23	4.40E-07	75	17.68	13.56	0.77	1.36E-05
31	12.56	8.31	0.66	3.63E-06	76	17.94	9.03	0.50	6.14E-06
32	12.66	7.57	0.60	3.04E-06	77	18.19	7.29	0.40	4.05E-06
33	13.35	9.88	0.74	5.45E-06	78	18.19	13.06	0.72	1.30E-05
34	13.52	8.64	0.64	4.23E-06	79	18.22	15.88	0.87	1.92E-05
35	13.53	12.03	0.89	8.21E-06	80	18.28	9.26	0.51	6.57E-06
36	13.54	12.15	0.90	8.37E-06	81	18.31	14.06	0.77	1.52E-05
37	13.66	9.89	0.72	5.59E-06	82	18.49	12.09	0.65	1.13E-05
38	13.70	10.15	0.74	5.91E-06	83	18.67	9.10	0.49	6.48E-06
39	13.82	8.82	0.64	4.51E-06	84	18.69	9.28	0.50	6.74E-06
40	13.83	7.72	0.56	3.45E-06	85	19.06	14.20	0.75	1.61E-05
41	13.93	6.53	0.47	2.49E-06	86	19.09	7.48	0.39	4.48E-06
42	14.13	8.70	0.62	4.48E-06	87	19.12	7.76	0.41	4.82E-06
43	14.25	14.25	1.00	1.21E-05	88	19.39	5.83	0.30	2.76E-06
44	14.40	3.82	0.27	8.80E-07	89	19.41	19.35	1.00	3.04E-05
45	14.49	13.07	0.90	1.04E-05	90	19.48	13.04	0.67	1.39E-05

5. Appendix

cons. no.	Ø a μm	Ø b μm	f_A μm/μm	$V_{particle}$ mm^3	cons. no.	Ø a μm	Ø b μm	f_A μm/μm	$V_{particle}$ mm^3
91	19.70	8.09	0.41	5.40E-06	136	26.33	13.39	0.51	1.98E-05
92	19.75	10.16	0.51	8.54E-06	137	26.40	21.75	0.82	5.23E-05
93	19.99	14.78	0.74	1.83E-05	138	26.54	18.02	0.68	3.61E-05
94	20.03	10.18	0.51	8.69E-06	139	26.75	14.22	0.53	2.27E-05
95	20.16	15.20	0.75	1.95E-05	140	26.77	18.48	0.69	3.83E-05
96	20.22	8.34	0.41	5.90E-06	141	27.11	11.25	0.41	1.44E-05
97	20.45	11.07	0.54	1.05E-05	142	27.13	19.41	0.72	4.28E-05
98	20.70	13.11	0.63	1.49E-05	143	27.32	11.83	0.43	1.60E-05
99	20.78	14.49	0.70	1.83E-05	144	27.39	26.23	0.96	7.90E-05
100	20.79	9.40	0.45	7.69E-06	145	27.68	15.67	0.57	2.85E-05
101	20.94	7.04	0.34	4.35E-06	146	27.77	13.32	0.48	2.06E-05
102	21.05	11.22	0.53	1.11E-05	147	27.80	22.05	0.79	5.66E-05
103	21.17	10.94	0.52	1.06E-05	148	27.85	26.03	0.93	7.90E-05
104	21.17	6.06	0.29	3.26E-06	149	27.98	23.82	0.85	6.65E-05
105	21.36	17.83	0.83	2.84E-05	150	28.05	14.11	0.50	2.34E-05
106	21.84	17.12	0.78	2.68E-05	151	28.07	17.69	0.63	3.68E-05
107	21.91	12.22	0.56	1.37E-05	152	28.18	15.29	0.54	2.76E-05
108	21.94	19.67	0.90	3.55E-05	153	28.27	7.94	0.28	7.47E-06
109	22.03	11.83	0.54	1.29E-05	154	28.43	13.59	0.48	2.20E-05
110	22.11	9.90	0.45	9.08E-06	155	28.48	7.62	0.27	6.92E-06
111	22.14	7.62	0.34	5.38E-06	156	28.58	13.76	0.48	2.26E-05
112	22.15	13.22	0.60	1.62E-05	157	28.63	8.36	0.29	8.39E-06
113	22.24	10.23	0.46	9.75E-06	158	28.96	22.60	0.78	6.19E-05
114	22.24	12.12	0.55	1.37E-05	159	29.21	19.83	0.68	4.81E-05
115	22.25	9.94	0.45	9.21E-06	160	29.21	15.27	0.52	2.85E-05
116	22.28	10.95	0.49	1.12E-05	161	29.93	8.26	0.28	8.55E-06
117	22.39	15.24	0.68	2.18E-05	162	30.31	21.62	0.71	5.93E-05
118	22.49	15.62	0.69	2.30E-05	163	30.77	20.47	0.67	5.40E-05
119	23.14	13.69	0.59	1.82E-05	164	30.78	14.87	0.48	2.85E-05
120	23.14	17.01	0.74	2.80E-05	165	31.09	15.39	0.50	3.09E-05
121	23.17	11.33	0.49	1.25E-05	166	31.21	11.76	0.38	1.81E-05
122	23.20	11.65	0.50	1.32E-05	167	31.47	18.05	0.57	4.29E-05
123	23.21	12.53	0.54	1.53E-05	168	31.62	25.69	0.81	8.74E-05
124	23.27	10.45	0.45	1.06E-05	169	31.96	6.31	0.20	5.33E-06
125	23.36	14.66	0.63	2.10E-05	170	32.10	23.30	0.73	7.30E-05
126	24.14	10.67	0.44	1.15E-05	171	32.16	9.05	0.28	1.10E-05
127	24.52	15.77	0.64	2.55E-05	172	32.24	23.04	0.71	7.17E-05
128	24.70	15.26	0.62	2.41E-05	173	32.31	17.00	0.53	3.91E-05
129	24.71	13.41	0.54	1.86E-05	174	32.41	9.39	0.29	1.20E-05
130	24.98	13.33	0.53	1.86E-05	175	32.43	31.71	0.98	1.37E-04
131	25.07	15.87	0.63	2.65E-05	176	32.59	14.02	0.43	2.68E-05
132	25.08	21.48	0.86	4.85E-05	177	32.64	19.93	0.61	5.43E-05
133	25.33	6.66	0.26	4.70E-06	178	32.80	19.02	0.58	4.97E-05
134	25.69	7.84	0.31	6.62E-06	179	32.88	25.69	0.78	9.09E-05
135	26.01	16.25	0.62	2.88E-05	180	32.90	9.51	0.29	1.25E-05

5. Appendix

cons. no.	Ø a µm	Ø b µm	f_A µm/µm	$V_{particle}$ mm³	cons. no.	Ø a µm	Ø b µm	f_A µm/µm	$V_{particle}$ mm³
181	32.92	12.85	0.39	2.28E-05	226	44.78	20.94	0.47	8.22E-05
182	33.40	18.77	0.56	4.93E-05	227	45.00	16.92	0.38	5.40E-05
183	33.85	21.06	0.62	6.29E-05	228	45.01	31.04	0.69	1.82E-04
184	33.91	23.00	0.68	7.51E-05	229	45.18	23.24	0.51	1.02E-04
185	33.95	18.60	0.55	4.92E-05	230	45.50	34.46	0.76	2.26E-04
186	34.17	18.68	0.55	5.00E-05	231	45.58	26.65	0.58	1.36E-04
187	34.67	18.45	0.53	4.94E-05	232	47.15	35.58	0.75	2.50E-04
188	34.73	30.21	0.87	1.33E-04	233	47.23	24.66	0.52	1.20E-04
189	34.74	20.28	0.58	5.99E-05	234	47.60	26.95	0.57	1.45E-04
190	35.08	25.80	0.74	9.78E-05	235	47.88	46.58	0.97	4.35E-04
191	35.21	32.19	0.91	1.53E-04	236	48.53	29.85	0.62	1.81E-04
192	35.28	18.24	0.52	4.92E-05	237	49.06	25.36	0.52	1.32E-04
193	35.50	20.17	0.57	6.05E-05	238	49.36	17.59	0.36	6.40E-05
194	35.89	27.94	0.78	1.17E-04	239	49.49	24.45	0.49	1.24E-04
195	36.06	11.81	0.33	2.11E-05	240	51.19	29.65	0.58	1.88E-04
196	36.06	10.75	0.30	1.74E-05	241	51.58	27.71	0.54	1.66E-04
197	36.53	36.22	0.99	2.01E-04	242	52.01	35.03	0.67	2.67E-04
198	36.84	26.88	0.73	1.11E-04	243	52.18	29.89	0.57	1.95E-04
199	36.89	15.71	0.43	3.82E-05	244	53.89	44.49	0.83	4.47E-04
200	37.07	18.97	0.51	5.59E-05	245	54.08	27.32	0.51	1.69E-04
201	37.11	22.81	0.61	8.09E-05	246	55.36	52.98	0.96	6.51E-04
202	37.23	23.32	0.63	8.48E-05	247	55.61	43.32	0.78	4.37E-04
203	37.24	16.43	0.44	4.21E-05	248	55.90	29.02	0.52	1.97E-04
204	37.28	20.28	0.54	6.42E-05	249	55.91	44.41	0.79	4.62E-04
205	37.99	36.12	0.95	2.08E-04	250	56.28	39.34	0.70	3.65E-04
206	38.01	38.01	1.00	2.30E-04	251	58.30	34.58	0.59	2.92E-04
207	38.06	19.75	0.52	6.22E-05	252	58.31	42.84	0.73	4.48E-04
208	38.78	15.98	0.41	4.15E-05	253	58.59	17.66	0.30	7.65E-05
209	38.83	19.97	0.51	6.49E-05	254	58.64	21.42	0.37	1.13E-04
210	38.94	19.86	0.51	6.43E-05	255	59.28	44.95	0.76	5.02E-04
211	39.74	20.01	0.50	6.66E-05	256	59.33	38.62	0.65	3.71E-04
212	39.76	10.06	0.25	1.69E-05	257	59.77	34.89	0.58	3.05E-04
213	40.45	18.12	0.45	5.56E-05	258	59.94	27.67	0.46	1.92E-04
214	40.63	20.08	0.49	6.86E-05	259	60.75	22.97	0.38	1.34E-04
215	40.93	29.16	0.71	1.46E-04	260	60.87	27.84	0.46	1.98E-04
216	41.11	23.90	0.58	9.84E-05	261	61.92	43.34	0.70	4.87E-04
217	41.60	36.42	0.88	2.31E-04	262	62.89	33.06	0.53	2.88E-04
218	41.67	30.68	0.74	1.64E-04	263	63.76	63.25	0.99	1.07E-03
219	41.76	35.22	0.84	2.17E-04	264	63.91	39.12	0.61	4.10E-04
220	42.00	29.52	0.70	1.53E-04	265	63.94	50.03	0.78	6.70E-04
221	42.37	33.37	0.79	1.98E-04	266	64.62	38.75	0.60	4.06E-04
222	43.29	39.32	0.91	2.80E-04	267	65.47	39.71	0.61	4.32E-04
223	43.38	35.03	0.81	2.23E-04	268	67.36	23.43	0.35	1.55E-04
224	43.44	43.07	0.99	3.38E-04	269	68.23	26.69	0.39	2.04E-04
225	44.54	39.66	0.89	2.93E-04	270	68.43	53.35	0.78	8.16E-04

5. Appendix

cons. no.	Ø a μm	Ø b μm	f_A μm/μm	$V_{particle}$ mm³
271	73.60	17.94	0.24	9.93E-05
272	75.77	18.52	0.24	1.09E-04
273	78.87	21.56	0.27	1.54E-04
274	81.79	78.74	0.96	2.12E-03
275	84.74	59.45	0.70	1.25E-03
276	84.88	81.74	0.96	2.38E-03
277	86.56	42.09	0.49	6.42E-04
278	89.04	61.49	0.69	1.41E-03
279	91.57	59.60	0.65	1.36E-03
280	91.83	27.02	0.29	2.81E-04
281	91.96	61.98	0.67	1.48E-03
282	92.02	40.28	0.44	6.25E-04
283	98.62	59.93	0.61	1.48E-03
284	99.13	43.87	0.44	7.99E-04
285	102.67	73.35	0.71	2.31E-03
286	111.91	110.39	0.99	5.71E-03
287	119.76	105.03	0.88	5.53E-03
288	134.94	90.30	0.67	4.61E-03
289	149.29	100.15	0.67	6.27E-03

5. Appendix

5.M   Curriculum vitae

Name: Sebastian Roß
Date of birth: 6th of July, 1985 in Stadthagen, Lower Saxony, Germany

Education
_____

06/04   Secondary high school diploma at Ratsgymnasium Stadthagen

10/04 - 11/09   Studies of chemistry at University of Hanover

08/06   Intermediate diploma in chemistry at University of Hanover

04/09   Diploma examinations in chemistry at University of Hanover

05/09 - 11/09   Preparation of the diploma thesis at Bayer Technology Services
                     GmbH in Leverkusen, Germany; in collaboration with the Institute
                     of Inorganic Chemistry at the University of Hanover.

Since 01/10   Research associate at the Institute of Mineralogy, Leibniz University
                     Hanover, including the preparation of a dissertation to Dr. rer. nat. in
                     the workgroup petrology supervised by Prof. Dr. Harald Behrens.

Previous experiences
_____
02/07 - 03/07   Internship at BASF Coatings AG Münster, Germany

08/07 - 03/08   Student assistant at the Institute of Inorganic Chemistry

11/08 - 03/09   Student assistant at the Institute of Inorganic Chemistry

Career
_____

Since 10/13   Developer for electrochemical gas sensors at the MSA Auer GmbH,
                     Berlin, department Sankt Augustin.

Acknowledgements

Acknowledgements

readiness to help, the technical and scientific support and the awesome shared off time. Namely to mention is my office colleague Robert Knobel which I want to thank for all the technical discussion during the pressure cell development.

I want to thank my proofreaders Lars Schomborg and Isabella Laskowski for their helpful comments and constructive criticism.

Additionally, I want to express my grateful thanks to my family and friends for the encouraging time, outstanding support and all the memorable moments in the last exciting years. To conclude I want to thank Julia for her love, help and sympathy from near and far.

Acknowledgements

List of publications

1.)

Anna-Maria Welsch, Harald Behrens, Ingo Horn, Sebastian Roß, Paul Heitjans, *Self-Diffusion of Lithium in LiAlSi$_2$O$_6$ Glasses Studied Using Mass Spectrometry*, The Journal of Physical Chemistry A, **2012**, 122, 309-318

2.)

Anna-Maria Welsch, Harald Behrens, Sebastian Ross, Dawid Murawski, *Structural Control of Ionic Conductivity in LiAlSi$_2$O$_6$ and LiAlSi$_4$O$_{10}$ Glasses and Single Crystals*, Zeitschrift für Physikalische Chemie, **2012**, 226, 491

3.)

Sebastian Ross, Anna-Maria Welsch, Harald Behrens, *Lithium conductivity in glasses of the Li$_2$O - Al$_2$O$_3$ - SiO$_2$ system*, Phys. Chem. Chem. Phys., **2015**, 17 (1), 465 - 474